THE HONG KONG
POLYTECHNIC UNIVERSITY
香港理工大學
Pao Yue-kong Library
包玉剛圖書館

Copyright Undertaking

This thesis is protected by copyright, with all rights reserved.

By reading and using the thesis, the reader understands and agrees to the following terms:

1. The reader will abide by the rules and legal ordinances governing copyright regarding the use of the thesis.
2. The reader will use the thesis for the purpose of research or private study only and not for distribution or further reproduction or any other purpose.
3. The reader agrees to indemnify and hold the University harmless from and against any loss, damage, cost, liability or expenses arising from copyright infringement or unauthorized usage.

IMPORTANT

If you have reasons to believe that any materials in this thesis are deemed not suitable to be distributed in this form, or a copyright owner having difficulty with the material being included in our database, please contact lbsys@polyu.edu.hk providing details. The Library will look into your claim and consider taking remedial action upon receipt of the written requests.

Pao Yue-kong Library, The Hong Kong Polytechnic University, Hung Hom, Kowloon, Hong Kong

http://www.lib.polyu.edu.hk

LOCALIZATION AND CHARACTERIZATION OF THE FAULT IN WHEEL/RAIL SYSTEM

CHEN LONG

PhD

The Hong Kong Polytechnic University

2020

The Hong Kong Polytechnic University

Department of Mechanical Engineering

Localization and Characterization of the Fault in Wheel/rail System

CHEN Long

A thesis submitted in partial fulfillment of the requirements for the degree of

Doctor of Philosophy

Aug, 2019

CERTIFICATE OF ORIGINALITY

I hereby declare that this thesis is my own work and that, to the best of my knowledge and belief, it reproduces no material previously published or written, nor material that has been accepted for the award of any other degree or diploma, except where due acknowledgement has been made in the text.

(Signed)

CHEN Long (Name of student)

Department of Mechanical Engineering

The Hong Kong Polytechnic University

Hong Kong, China

Aug, 2019

ABSTRACT

This thesis presents a microphone array-based approach to localize and characterize the fault for the wheel/rail system under an environment with high background noise and the ground reflection interference.

In the modern city nowadays, fault detection systems are typically applied in the railway industry to examine the structural health status of the wheel/rail system. The damage or fault on the surface structure of the wheels can cause impact noise lead to great environmental pollution or even cause fatal railway accident. Therefore, it is necessary to develop a structural condition monitoring system in order to improve the operability and reliability of the wheels in service. To deal with such problems, various methods have been employed to monitor the condition of wheel/rail system, such as acoustic emission (AE), ultrasonic wave, and magnetic testing. However, these methods can only indicate the existence of faults, but they cannot determine the position of the fault wheel. Since these existing techniques only rely on contact inspection methods and periodical maintenance to eliminate the potential security issues, this paper attempts to achieve fault visualization by adopting an acoustic-based noncontact diagnosis method. In this regard, the approach by using microphone array can be very effective to detect the faults on the structure surface.

Before going into the main part of the thesis, preliminary investigation is first conducted by using a useful tool for characterizing and detecting non-stationary impulsive signals named spectral kurtosis (SK), then the wavelet transform (WT) based SK is proposed to extract the impulsiveness feature of signals in frequency-domain by smoother curves. However, considering the broadband feature of the impact noise generated by the uneven structural surface, it is difficult to identify the appropriate frequency bands for calculating the SK of a broadband signal. The research findings indicate that the wheel faults can hardly be identified using the traditional frequency-domain method. Thus, through the exploration of the traditional beamforming methods including delay-and-sum (DAS), linearly constrained minimum variance (LCMV) and multiple signal classification (MUSIC) by adopting plane wave and spherical wave model, a so called broadband weighted MUSIC (BW-MUSIC) method is proposed to detect the broadband signals. Meanwhile, a kurtosis based beamformer in time-domain is proposed to identify the fault under multiple sound sources circumstance and achieve fault visualisation as a function of time and space, instead of frequency and space. By using kurtosis beamformer, different types of faults on the wheels could be identified and localised by observing the kurtosis value on the beamforming sound map. The effectiveness of the proposed method to diagnose the wheel fault has been validated experimentally in this section. By the validation of experiments and simulations, the proposed kurtosis beamformer in time-domain is feasible to distinguish the location of the wheel with fault from the pristine wheel.

The application of kurtosis enables the identification and localisation at extremely low signal-to-noise ratio (SNR). By thoroughly discussions and comparisons with other estimators such as peak value and root mean square (RMS), the kurtosis beamformer was found to be suitable for a wide range of SNRs, even in cases where the impulsive feature in the signal is completely indistinguishable using the traditional beamforming method from the background noise. Compared with the beamforming output evaluated by RMS and peak value, the kurtosis beamformer has a lower sidelobe level (SLL) and its ability to extract the impulsiveness emerging from the background noise is much stronger. Typically, the beamforming power can yield accurate positions of the sound sources in a field of multiple sound sources based on the acoustical power. Its suitability for a wide range of SNRs makes the main advantage when compared with the state-of-the-art structural condition monitoring non-destructive testing (NDT) techniques, apart from eliminating the necessity to attach the sensors to the structure. The influence of the duration of data acquisition on the performance of kurtosis beamformer has been discussed as well. Generally, when the duration of data acquisition for analysis contains at least one impulse signal, it would be accurate enough to identify the fault according to the kurtosis beamformer. However, if the number of impulses per second is high, the kurtosis value becomes low and may influence the accuracy of the fault localisation.

The localization approach is then extended to sound wave propagation model with ground effect and moving source. With multiple sound sources and the interference of ground reflection, the mentioned BW-MUSIC method could provide a separate and distinct localization result in sound map to compute as an initial value. Based on that, the so-called Levenberg-Marquardt and Crank Nicolson (LM-CN) method can provide a preferable estimation result of ground impedance. Compared with the former LM approach to estimate ground impedance, the rate of convergence among all parameters is improved in LM-CN method. And the convergence values are closer to the actual values.

Theoretically, in low Mach number cases, moving source problems could be solved by adopting an instantaneous frequency. Therefore, the BW-MUSIC method is first examined. A de-Dopplerization approach is adopted and combined with the kurtosis beamformer to deal with the high Mach number cases in time-domain. The experimental results presented in sound maps had a good matching with the actual conditions in terms of localizing and identifying. The localization results for three moving sources were acceptable, and the improved sound maps can identify wheel fault with the interference of background noise.

PUBLICATIONS ARISING FROM THE THESIS

Chen, L., Choy, Y. S., & Wang, T. G. (2017). Fault diagnosis by time-domain beamforming integrated with kurtosis method. INTER-NOISE and NOISE-CON Congress and Conference Proceedings.

Chen, L., & Choy, Y.-S. (2018) Fault identification and localization for moving wheels based on de-dopplerization beamforming kurtosis method. Berlin Beamformig Conference.

Chen, L., Choy, Y. S., Wang, T. G., & Chiang, Y. K. (2019) Fault detection of wheel in wheel/rail system using kurtosis beamforming method. Structural Health Monitoring, doi:10.1177/1475921719855444

ACKNOWLEDGEMENTS

I would like to thank all of the people who kindly helped me during my Ph.D study in the Department of Mechanical Engineering, The Hong Kong Polytechnic University. Without their kindly help, this thesis would not have been accomplished.

I would like to express my deepest appreciation to my supervisor Dr. Choy Yat-Sze for who proposed this project title and gave me the most patient guidance and generous necessary financial aid. I would like to thank Dr. Wang Tiangang for who shared the research ideas and gave many constructive advises at the beginning of my study. Without their selfless assistance, support and encouragement, this thesis would not have been accomplished either.

I would also like to thank Dr. Wang Zhibo, Mr. Wei Long, Dr. Chiang Yan-Kei, Mr. Yang Weiping, Dr. Kai-Chung Tam, Prof. Fei Chengwei for their instructions and technical support during my study.

The last but not the least, I would like to thank my parents and parents-in-law for their support and encouragement. Special thanks to my wife, Dr. Ma Jing, for all her love, encouragement, understanding and academic support during my Ph.D study.

NOMENCLATURE

Symbol	Description
M	the index of microphone
m	the index of each microphone
ω	angular frequency
θ	incident angle
i	imaginary number
$p_m(\omega)$	the complex pressure signal at the receiver
$q(\omega)$	sound source excitation
$h_m(\theta,\omega)$	the transfer function between the microphone and the sound source excitation in far-field assumption
e	Euler number
c	the speed of sound
d	the distance between the adjacent microphones
$h_m(r_m,\omega)$	the transfer function between the microphone and the sound source excitation in near-field assumption
r_m	the distance between the mth receiver and the sound source
$kurtosis(x)$	kurtosis value
E	the expected value of the quantity
$\mu(x)$	mean value

$\sigma(x)$	standard deviation
$w(n)$	the analysis window
N_w	the analysis window length
P	temporal step size
$Y(t)$	arbitrary time-domain process
f	frequency
$Y_w(kP, f)$	short-time Fourier transform
π	Pi
$S_{2nY}(f)$	2n-order empirical spectral moment
$K_Y(f)$	spectral kurtosis
$K_{WT}(f)$	wavelet transform-based spectral kurtosis
$S_{2nW}(f)$	the 2n-order empirical spectral moment of wavelet transform
$WT(\tau, a)$	wavelet transform
a	the scale of wavelet function
τ	the translation time
F_{scale}	the frequency corresponding to the scale
F_c	the center frequency of wavelet basis
F_s	the sampling rate
$s(t)$	a Gaussian impulse signal
$\mathbf{w}(r_m, \omega)$	weighting function in spherical wavefront model
$b(r_m, \omega)$	the frequency-domain DAS beamformer output in near-field
$w_m(r_m, t)$	the time-domain beamformer weighting function

$p_m(t)$	the measured signal in time-domain
$b(r_m,t)$	the time-domain DAS beamformer output in near-field
$\beta(r_m,t)$	The time-domain beamforming power in near-field
$Kurt(r_m)$	the kurtosis beamformer output
H	Hermitian transpose
$\beta(\theta,\omega)$	the frequency-domain beamforming power in far-field
$b(\theta,\omega)$	the frequency-domain beamforming output in far-field
$\mathbf{R}(\omega)$	correlation matrix
$\beta_{MVDR}(\theta)$	the minimum variance distortionless response beamforming power
$\mathbf{U}_{sn}$	eigenvectors of correlation matrix belonging to the signal subspace
$\mathbf{D}_{sn}$	eigenvalues of correlation matrix belonging to the signal subspace
$\mathbf{U}_n$	eigenvectors of correlation matrix belonging to the noise subspace
$\mathbf{D}_n$	eigenvalues of correlation matrix belonging to the noise subspace
$\mathbf{U}$	eigenvectors of correlation matrix
$\mathbf{D}$	eigenvalues of correlation matrix
$\beta_{MUSIC}(\theta)$	The multiple signal classification beamforming output in far-field assumption

Q	complex spherical wave reflection coefficient
R_p	plane wave reflection coefficient
$F(w)$	boundary loss factor
Z	normal impedance of the ground surface
α_e	the effective rate of change of porosity with depth
σ_e	the effective flow resistivity at the ground surface
$\beta_{MUSIC}(r_m)$	the multiple signal classification beamforming output in near-field assumption
$\beta_{BM}(r_m)$	the broadband multiple signal classification beamforming output
$\beta_{WBM}(r_m)$	the broadband weighted multiple signal classification beamforming output
$\mathbf{e}(x, y, \sigma_e, \omega)$	the error function of the sound source location and the effective flow resistivity
$\mathbf{S}(x_0, y_0, \sigma_{e_0}, \omega)$	the initial reference signal vector
$\hat{\mathbf{S}}(x, y, \sigma_e, \omega)$	the signal vector to be estimated
$\mathbf{J}(\omega)$	the Jacobian matrix
ξ_{n+1}	The $(n+1)^{\text{th}}$ iteration result of the Levenberg–Marquardt optimisation process
λ	positive scalar regularisation parameter
p_t	total acoustic pressure
ρ	fluid density

$\mathbf{q}_d$	the dipole domain source
Q_m	the monopole domain source
S	the source strength
A_m	the value of the pulse amplitude
f_0	the frequency bandwidth
t_p	the pulse peak time
Z_a	the acoustic input impedance
Z_{ac}	the acoustic impedance
Z_{mech}	the mechanical impedance
δ_x	the ratio between the error and the actual fault location in percentage in x direction
δ_y	the ratio between the error and the actual fault location in percentage in y direction
x_a	actual fault coordinate in x direction
y_a	actual fault coordinate in y direction
x_e	the estimated coordinate by the beamforming approach in x direction
y_e	the estimated coordinate by the beamforming approach in y direction
v_0	moving speed
$\mathbf{r} = [x, y, z]$	observation position
$\mathbf{r}_0 = [v_0\tau_j, 0, 0]$	source position

$M_0(\tau)$	Mach number
φ_s	the phase of a moving source at the receiver
ω_i	the instantaneous frequency at the receiver
$\beta_{WBD}(r_m)$	the broadband weighted delay-and-sum beamforming output
$\beta_{DAS}(r_m, f)$	traditional delay-and-sum beamforming power at near-field assumption
K	the number source signals
$b(\Delta\mathbf{r}_\kappa, \tau)$	the de-Dopplerized time-domain beamforming output
$\cos\varphi_{m\kappa}(\tau)$	the angle between the direction of $\mathbf{v}_0$ and $\mathbf{r}_m - \left[\mathbf{r}_0(\tau) + \Delta\mathbf{r}_\kappa\right]$

ABBREVIATION

ABD	acoustic-based diagnosis
AE	acoustics emission
B-MUSIC	broadband MUSIC
BW-DAS	broadband weighted DAS
BW-MUSIC	broadband weighted MUSIC
Clean-SC	Clean based on source coherence
CN	Crank Nicolson
DAMAS	deconvolution approach for the mapping of acoustic sources
DAS	delay-and-sum
DBF	digital beamforming
DBSAR	Digital Beamforming Synthetic Aperture Radar
DC	direct current
DOA	direction of arrivals
EMAT	electromagnetic acoustic transducer
FDM	finite difference method
FEM	finite element method
FFT	fast Fourier transform
FT	Fourier transform
IFT	inverse Fourier transform

JTFA	joint time-frequency analysis
LCMV	linearly constrained minimum variance
LM	Levenberg–Marquardt
MEMS	microelectrical-mechanical system
MUSIC	multiple signal classification
MVDR	minimum variance distortionless response
NAH	near-field acoustical holography
NASA	National Aeronautics and Space Administration
NDT	non-destructive testing
OOR	out-of-roundness
PML	perfectly matched layer
PZT	piezoelectric lead zirconate titanate
RCF	rolling contact fatigue
RMS	root mean square
SDP	symmetrised dot pattern
SK	spectral kurtosis
SLL	sidelobe level
SNR	signal-to-noise ratio
SPL	sound pressure level
STFT	short-time Fourier transform
TDOA	time difference of arrival
TRA	time reversal acoustics

ULA	uniform lineal microphone array
WT	wavelet transform

TABLE OF CONTENTS

LIST OF FIGURES AND TABLES

CHAPTER 1

Introduction and literature review

1.1 Background

Railway engineers have been troubled by imperfections on train wheels since the wheel/rail system was used in modern society (Alemi, Corman, & Lodewijks). When trains are travelling, imperfections on wheels can always significantly affect the rails, sleepers as well as bearings in wheel/rail system, cause annoying noise and potential security issues. Therefore, fault diagnosis is crucial for conditional-based maintenance in the railway industry (Beebe, 1995). Currently, approximately 21,000 locomotives, 73,000 carriages, and 799,000 wagons are operational in China (Barke & Chiu, 2005). Under such circumstances, structural condition monitoring systems are widely implemented in the railway industry and various monitoring approaches have been proposed for the inspection of wheel and rail conditions (Alemi et al.). However, nearly half of the train accidents still resulting from imperfect train wheels, which owed to the prolonged usage of the wheel/rail system. Moreover, the routine inspections are still relied on the detection of the fault, and the comprehensive maintenance cost of checking all the

wheels of a train can be very expensive.

As a non-contact diagnoses method, the technology of sound source localization and characterization by using microphone array can be very effective to detect the faults on the structure surface (Steyskal, 1987). Although the technology has been developed for decades, it remains a complicated task to localize and characterize the sound sources in specific industrial occasions. For instance, in wheel/rail system, background noise interference can be serious, and sound sources are usually moving. Meanwhile, the ground reflection must be considered during fault localization and detection approach. To remain valid in such occasions in the wheel/rail system, we propose a time-domain kurtosis beamforming technique using microphone array for fault localization and characterization in this article (Chen, Choy, & Wang, 2017).

1.2 Structure condition monitoring in railway industry

Wheels wear out or get damaged due to frequent use, leading to an uneven surface or an irregular shape. In the wheel/rail system, these faults and imperfections can be categorised into wheel-flat due to severe wearing, dent due to crack, and squat and corrugation due to rolling contact fatigue (RCF) (S. Grassie & Kalousek, 1993; S. L. Grassie, 2005; Johansson, 2006; Nielsen & Johansson,

2000). When the driver brakes forcible horizontal pressures are applied to railway wheels, sometimes the wheels will lock and then slide along the rail during traveling. Such locking and sliding will cause a severe wear of one specific part of the wheels in contact with the rail, leading to the formation of a “wheel-flat”, which can be regarded as grave discontinuities on the wheel/rail surface during wheels rotating (Thompson & Jones, 2000; Wu & Thompson, 2002). And it also be regarded as one type of wheel out-of-roundness (OOR). Crack can be categorised into thermal crack and fatigue crack. Thermal crack is the result of alternate heating and cooling of the wheel when it is travelling and braked frequently, and it originates from a metallurgical change in the wheel material. It is considered to be the most severe form of wheel fault. Fatigue crack, squat and corrugation are all caused by repeated contact stress during the wheel rolling motion. They are usually known as RCF and can sustainably develop on wheel surface. RCF is associated particularly with heavy load of the train, irregular welds on the rail, and flakes at the gauge corner of the rail. In addition, block braked of wheel treads can also leads to corrugation.

These discontinuities in wheel/rail system can generate large impact forces and leads to impact noise and/or increased rolling noise between the wheel and rail (Vér, Ventres, & Myles, 1976). Rolling noise ensues when wheels pass over the rail. This is predominantly caused by undulations of the wheel and the surface of the rail, thereby inducing a vertical relative vibration. Impact noise can be

considered as an extreme form of rolling noise, which is caused by faulty or uneven structural surfaces of the wheel or rail (Hanson, Towers, & Meister, 2006). As a periodical sound signal, impact noise is produced and added to the usual rolling noise when the wheels running over discontinuities or rail joints, which can be regarded as a relatively harmless condition. Contrary to the traditional acoustics emission (AE) phenomenon, impact noise is an impulsive, short duration pressure pulse with a peak amplitude that is much higher than that of the rolling noise (X. Zhang, Feng, Wang, & Shen, 2015). It is a quasi-periodic series of impulsive signal according to the cycle of the rotating wheel. Broadband, short duration, low acoustic energy level, low signal-to-noise ratio (SNR), and quasi-periodical nonstationary characteristics are some of the features of impact noise (Liang, Iwnicki, Ball, & Young, 2015).

To identify and localise the position of the aforementioned discontinuities in the wheel/rail system, so that the repair and maintenance can be performed on time, a reliable real-time structural condition monitoring system is needed to be implemented. Therefore, a variety of fault detection methods have been developed, such as vibration analysis, magnetic testing, Lamb wave analysis, and AE (Dornfeld & Cai, 1984; Drinkwater & Wilcox, 2006; Matsumoto et al., 2008; Peng & Kessissoglou, 2003; Salzburger, Schuppmann, Li, & Xiaorong, 2009; Su, Ye, & Lu, 2006). In vibration analysis, the presence of defects is identified by observing the frequency shift or variation of the pattern of the time-variant signal

and comparing that with the patters obtained from a healthy structure. In magnetic testing, electromagnetic acoustic transducer (EMAT) probes are mounted along the rails to inspect the wheels when a train passes by in a short time. The Rayleigh wave is transmitted when the wheel is contact with the EMAT probe. The Rayleigh wave pulse makes several round trips along the tread of the wheel. The EMAT probes detect echoes from discontinuities in the tread in the pulse echo mode after these round trips. Lamb waves are generated and captured by piezoelectric sensors and possess high susceptibility to interference on a propagation path. These are considered cost effective for fault identification, compared to the previous two techniques. Different types of faults and damages in the structure can be identified by selecting the appropriate Lamb modes (Su et al., 2006). AE is a phenomenon, wherein a radiation of transient elastic waves is generated from a rapid release of strain energy resulting from deformation or damage within or on the surface of a material. These waves are generated by the interaction of two media in relative motion and an AE signal is emitted only at the time of these events. In practical applications, several AE sensors are mounted on the wheel and techniques such as rail testing model, wavelet transform (WT) and Shannon entropy are utilized to filter the AE signal and detect the defects based on the feature of time window (X. Zhang et al., 2015). The Shannon entropy of noise signals has lower fluctuation and smaller standard deviation than the AE signals so that defects in rails can be detected. This method provides satisfactory performance under an environment of high background noise. However, the influence of noise effects on fault detection

is significant, when the train travels in high speeds. Furthermore, the AE method can only monitor the generation of faults in a structural health monitoring system. It is not used to detect the structural defeats after the formation of faults.

These aforementioned fault detection approaches can mostly be regarded as contact methods, as the sensors are required to be mounted on the surface of the structure with wiring. In order to eliminate the additional loading by the sensor on the structure or any further issue related to the moving structure, coupling and real-time diagnostic need in railway industry, a noncontact measurement approach, such as acoustics-based diagnosis, is a more attractive option. Some researchers have strived to employ acoustic-based diagnosis (ABD) methods to detect faults in rotating machinery. This includes utilising the symmetrised dot pattern (SDP) method to detect abnormalities in bearings, and the near-field acoustical holography (NAH) technique to detect faults in a gear box (Lu, Jiang, Yuan, & Yan, 2013; Shibata, Takahashi, & Shirai, 2000). However, for the NAH technique, an array of microphones should be located close to the detecting surface, which can be difficult to achieve. Even if the equivalent source method (ESM) combined with the other holographic methods can overcome the measuring distance difficulty when employed in the far-field, the physical interpretation of the nature of the identified source, the number of microphones, and the data processing time are the problems to implement the acoustical holography technique in such case. Therefore, an alternative method, called beamforming technique, is used to detect

the structural damages. By exploiting the different time-series characteristics, time-domain methods can be used to attain statistical decisions for fault detection and identification. Time-domain beamforming is considered effective and accurate to localise moving, transient, or broadband sound sources (Carter, 1981; Kim & Choi, 2013; Quazi, 1981; Trees, 2002). Time-domain beamformer can be evaluated by peak value, root mean square (RMS) value, or kurtosis (Martin & Honarvar, 1995; Seo, Choi, & Kim, 2014; Y. Zhang, Liang, Li, & Hou, 2013). Among these three estimators, kurtosis is considered the best indicator of signal impulsiveness for fault detection of rotating components. A team of researchers used the beamforming spectral kurtosis (SK) in the frequency domain to detect the fault of each component in a complex rotating machinery system (Antoni, 2004, 2006; Dwyer, 1983, 1984).

1.3 Sound source localization and characterization technique

Multiple options can be considered for localizing and characterizing sound sources within different conditions. Generally, they include beamforming technology, time difference of arrival (TDOA) technology (Dvorkind & Gannot, 2005; Owsley & Swope, 1981; Quazi, 1981), NAH and time reversal acoustics (TRA) (Fink, 1999; Fink, Montaldo, & Tanter, 2004; Maynard, Williams, & Lee, 1985; Veronesi & Maynard, 1987). Among these four types of approaches, TDOA

method cannot conduct signal enhancement to obtain the specific signal features during localizing for post-processing. The time differences of arrival of each microphone to sound source can be obtained by calculating the cross-correlation function of the measured signals. Therefore, TDOA method can only characterizes the geometry information of the sound source by at least four microphones in different planes. Based on the sound pressure distribution on the measurement plane, the NAH technique can completely reconstruct the sound source, not only the source location but also the shape of the sound source. However, it requires the microphone array arranged very close to the sound source which can hardly achieved along the transit railway. TRA is very suitable when the SNR is very low. It needs to reverse the time history of the received sound signal at all measurement points and play them back in space, so it demands another array of the sound sources besides the sensor array. To summarize, the TDOA, NAH and the TRA method are not very suitable for the cases involved in this article.

Beamforming is one of the microphone array location technologies which has high accuracy and effectiveness in both frequency and time domain (Kim & Choi, 2013). And it can also be effective when both the sound source is far and near to the microphone array. Plane and spherical model would be adopted in far-field and near-field, respectively. Beamforming can be considered as one of the conventional acoustic imaging methods, but is still can be used in the modern industrial field because of its advantages in fast computing, non-contact

measurement, and high-resolution output. This array-based measurement technique can be used from short to long distances, requires a relatively short calculation time and is less sensitive to noise compared to other methods.

One typical representative of beamforming technique is the famous conventional delay-and-sum (DAS) beamformer (Cigada, Ripamonti, & Vanali, 2007). Conventional DAS beamformer seeks to analyse the wavefront of noise source by introducing a scanning vector **w**, and to obtain the source location and characterisation. Normally the scan vector **w** is chosen based on the model or on the assumption of different types of the wavefront of source signals which can be measured at the same time, meanwhile it should satisfy both accuracy and robustness of the parameter estimation. It can be regarded as a data-independent approach because the scan vector does not depend on the measured data. Each signal is delayed relative to the distance separating the microphone and the source under consideration. By introducing the scanning vector, all the weighted signals reinforce each other. Therefore, the summation of these compensated signals is maximized. Then the location of the sound source can be found by scanning over the sound field to find the peak position where the summation of the compensated signals is maximized. The visualization of each scanning grid point on the scanning sound field forms a beamforming map, and the sound source is indicated by the peak positions. However, conventional DAS beamformer has a low spatial resolution at low frequencies, which is limited by the dimension of the microphone

array. Besides, the chosen of the scan vector results in that the sidelobe level of DAS beamformer is high.

To overcome the resolution limits and the sidelobe effects in DAS beamformer, the scan vector is continuously designed using information of the measured signals or correlation matrix in different beamformers. The latter research examined the structure of measured data to obtain an enhanced resolution. To analyze the measurement data, a correlation matrix representing the spatial relationship between microphone signals can provide a significant amount of useful information. The SNR of the measured correlation matrix determines the robustness of the estimation. Many representative techniques for improving the estimator performance in regard to the SNR are developed.

The linearly constrained minimum variance (LCMV) beamformer or so-called the Capon beamformer was designed to minimize the undesirable influence from sources in all directions only except the look direction $\boldsymbol{\theta}$ by introducing a vital important assumption that the total beamforming power $\boldsymbol{\beta}$ in the $\boldsymbol{\theta}$ direction will be minimized if the contributions of other sources are removed by the successive choice of the weighting vector "$\boldsymbol{w}$" (J. Li, Stoica, & Wang, 2003; Z. Wang, Li, & Wu, 2005). It helps to reduce the sidelobes and sharps the main-lobe significantly compared with the traditional DAS beamformer. Typically, if the amplitude output is constrained to be 1, the beamformer output response will not

be distorted in the steering direction. In this situation, the beamformer is called the minimum variance distortionless response (MVDR) beamformer.

The multiple signal classification (MUSIC) method has better precision than LCMV and DAS method (Schmidt, 1986). It can separate the signal subspace from noise subspaces based on the orthogonal relationship between the eigenvectors of the correlation matrix. It focuses on the noise subspace of eigenvectors' orthogonality against the vectors of the signal subspace. Therefore, the beamforming power, which can be calculated from the correlation matrix consisting of these eigenvectors, should be minimal since the scan vector belongs to the signal subspace, which is the essential assumption of the MUSIC method for realizing super-resolution, the MUSIC method can only indicate the relative beamforming power and localise the source of signals, but it cannot estimate the real amplitude of the beamformer output. Therefore, it can only be used to find the locations of sound sources, but the reconstruction of source signals at the source locations cannot be achieved. The methodology of these three beamforming methods will be introduced in detail in the next chapter.

The focus on different characters of sound sources has led to the development of deconvolution techniques such as deconvolution approach for the mapping of acoustic sources (DAMAS) or Clean based on source coherence (Clean-SC) (Brooks & Humphreys, 2006; Sijtsma, 2007). Additionally it was found that

conventional beamforming with Clean-SC may be the best method in three-dimension sound visualization. However, when the source map is clearly improved, these methods require large computation time. To solve this problem, a new sound source localization technique called Hybrid Method with lower computation time was proposed in 2014. Combined with DAMAS, the Hybrid Method can give very clear noise source map even when the sound source is immersed in the flow.

Beamforming power of a signal limited within a narrow frequency band is equivalent to the finite sum of its beamforming power at discrete frequencies (Mucci, 1984). A representative scan vector can be designed for all the frequency components in the finite band when the frequency bandwidth is narrow enough. Then the narrowband signal processing is similar to the single frequency case, while the above approach is not suitable for broadband signal approximately. For a broadband beamformer in frequency domain, a more complex frequency correction method needs to be adopted. This method attempts to covert the correlation matrices measured at different frequencies to a single reference frequency by introducing a transformation of the measurement space that is frequency invariant.

Nowadays, beamforming has been widely used in various fields such as radar and underwater community. In National Aeronautics and Space Administration (NASA), digital beamforming (DBF) is used to enhance antenna performance.

NASA's Digital Beamforming Synthetic Aperture Radar (DBSAR) is a reconfigurable L-Band radar that employs a phased array architecture and a state-of-the-art data acquisition and real-time processor in order to enable multi-mode measurement techniques in a single radar platform (Rincon et al., 2010). DBSAR collected multimode data aboard the NASA P3 aircraft: during its first field campaign over the Delmarva Peninsula in 2008. Another case that beamforming has been used in sound source identification is Airframe Noise Flight Test program, which was conducted by NASA and Gulfstream at the NASA Wallops Flight Facility during October 2006 to acquire baseline airframe noise data on a regional jet class of transport in order to determine noise source strengths and distributions for model validation (Khorrami, Lockard, Humphreys Jr, Choudhari, & Van de Ven, 2008).

1.4 Objectives

This thesis aims at the localization and characterization of sound sources, which are generated by the faults on the structure surface of wheel/rail system. Ground reflections, moving sound source conditions, background noise, and other interference noise sources should be considered in the research. Therefore, the objectives of this thesis are summarized as follows:

(1) To localise and identify the faults of a wheel in an environment with

different SNRs using time-domain kurtosis beamformer, and study the accuracy of fault detection under different SNRs and durations of data acquisition.

(2) To obtain corresponding kurtosis values for different types of wheel faults, which are helpful for differentiating the types of faults occurring during the early stages.

(3) To localise and identify the faults along with the ground reflection effect, and estimate the impedance of the reflecting ground surface.

(4) To extend the proposed methods into the moving sound source localization area.

(5) To show the possibility of detecting faults on a moving train.

1.5 Thesis structure

Both theoretical and experimental efforts have been involved in this study. This thesis consists of six chapters.

Chapter 2 introduces the basic sound propagation models which would be adopted in the following research. Two sound source localization and characterization techniques including time-domain beamforming and SK method in frequency-domain are presented. Thereafter, a preferable approach called kurtosis beamformer is proposed with experimental validations.

Chapter 3 focus on the extensional discussions of the proposed kurtosis beamformer. It is further investigated in many respects, including the types of fault, the influence of SNR and duration of data acquisition. And it is compared with current state-of-the-art techniques. As a non-contact early-stage fault detection approach, kurtosis beamformer is suitable for a wide range of SNR with an unnecessary effort of attaching the sensors on the structure surface.

In Chapter 4, the reality that the ground reflection effect with different material properties exists underneath the rail is considered. The kurtosis beamformer is extended to achieve the fault visualisation as well as to estimate the impedance of the ground. Considering the impedance is a function of frequency, an optimisation process in frequency-domain is introduced in this chapter and integrated with beamforming technique to deal with the two problems at the same time.

The proposed method is further modified in Chapter 5 to be utilized on the moving source localization approach. Considering the different moving speed of the sound source, the modification of the proposed method is studied in two different directions. In the end of this chapter, an outdoor measurement besides the railway is presented to validate the possibility of detecting the faults on a moving train.

At last a conclusion of some suggestions for further investigation is given in Chapter 6.

CHAPTER 2

Sound source localization and characterization

2.1 Introduction

In this chapter, two sound propagation models including plane wave and spherical wave model are firstly reviewed, which would be adopted in the following sound sources localization approaches. For sound source characterization problems, preliminary investigation is first conducted by using a useful tool for characterizing and detecting non-stationary impulsive signals named SK (de la Rosa, Sierra-Fernández, Agüera-Pérez, Palomares-Salas, & Moreno-Muñoz, 2013; Eftekharnejad, Alssayh, Addali, & Mba, 2012; Ottonello & Pagnan, 1994; Sawalhi, Randall, & Endo, 2007; Vrabie, Granjon, Maroni, & Leprettre, 2004). Based on that, the WT based SK is proposed to extract the impulsiveness feature of signals in frequency-domain by smoother curves (Daubechies, 1990; Nason & Silverman, 1995). However, considering the broadband feature of the impact noise generated by the uneven structural surface, it is difficult to identify the appropriate frequency bands for calculating the SK of

a broadband signal. The research findings indicate that the wheel faults can hardly be identified using the traditional frequency-domain method. Thus, a kurtosis based beamformer in time-domain is proposed to identify the fault under multiple sound sources circumstance and to achieve fault visualisation as a function of time and space, instead of frequency and space (Chen, Choy, Wang, & Chiang). By using kurtosis beamformer, the faults on the wheels could be identified and localised by observing the kurtosis value on the beamforming sound map. The effectiveness of the proposed method to diagnose the wheel fault has been validated experimentally in this chapter.

2.2 Sound propagation model

Sound source localization method differs due to the assumption of what type of wavefront will be measured. If the source is far from the array, then the direction of propagation is approximately equal at each sensor, and the propagation field within the array aperture can be regarded as a plane wave. But it a source is close to the array, the wavefront from the source is perceptively curved when observed over the array (Tuma, Janecka, Vala, & Richter, 2012). In this thesis, the spherical wavefront model is well fitted to the measurement data.

2.2.1 Plane wave model

The plane wave model is used when the sound sources are far away from the receivers. This means that the distance between an arbitrary sound source and an arbitrary receiver is much longer than the distance between two adjacent receivers. In such assumption, the direction of arrivals (DOA) are equal at each receiver, and once the DOA is estimated, then the sound source location is determined. Figure 2.1 shows a plane wave signal model adopted in a beamforming approach by using a uniform lineal microphone array (ULA).

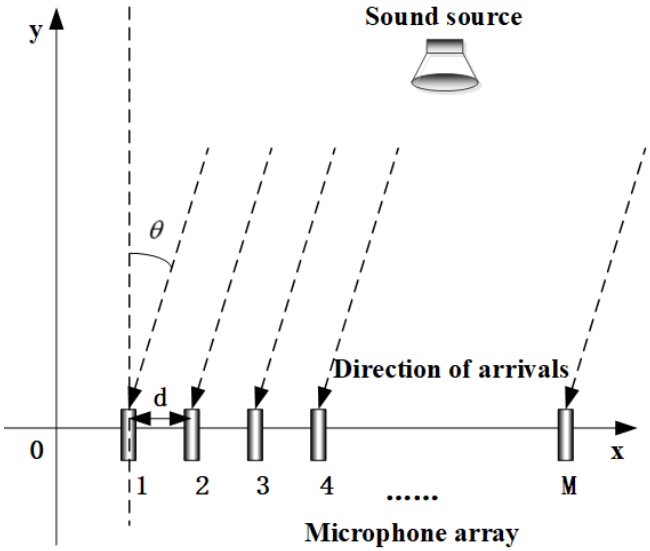

Figure 2.1 Plane wave signal model.

By using this signal model, the complex pressure signal at the *m*th microphone at x axis is given by:

$$p_m(\omega) = q(\omega)h_m(\theta,\omega) \tag{2.1}$$

in which θ is the incident angle of the plane wave, m is the index of each microphone (m=1, …, M), and $h_m(\theta,\omega)$ is the transfer function between the *m*th

microphone and the sound source excitation *q*, which can be expressed as:

$$h_m(\theta,\omega) = e^{-i\omega(m-1)(d/c)\sin\theta} \tag{2.2}$$

in the free-field assumption, where *c* is the speed of sound and *d* is the distance between the adjacent microphones.

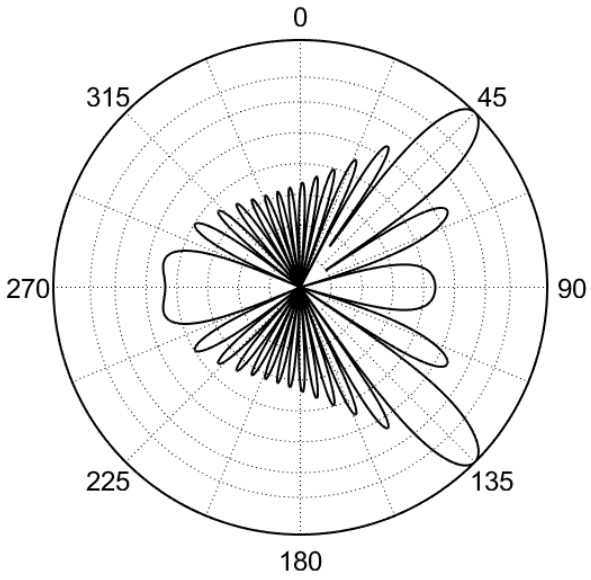

Figure 2.2 Beamforming result by adopting plane wave signal model.

Figure 2.2 shows a representative DAS beamformer output computing by MATLAB by adopting the plane wave signal model. The incident angle θ is set to be $45°$. Since the ULA can not tell the difference between the front and the back, the beamforming map is symmetrical with the microphone array (x axis).

2.2.2 Spherical wave model

Based on the near-field assumption, the spherical wave model is used in

which the sound sources are relatively near from the receivers. The distance between an arbitrary sound source and an arbitrary receiver can be comparable compared with the distance between two adjacent receivers. Similarly, Figure 2.3 shows a spherical wave model adopted in a beamforming approach by using ULA. The wavefront from the sound source at (x, y) is curved when arriving at the microphones. In such case, the transfer function between the receiver and the sound source can be written as:

$$h_m(r_m, \omega) = \frac{e^{i\omega r_m / c}}{r_m} \tag{2.3}$$

in which $r_m = \sqrt{(x - x_m)^2 + (y - y_m)^2}$ is the distance between the *m*th receiver and the sound source.

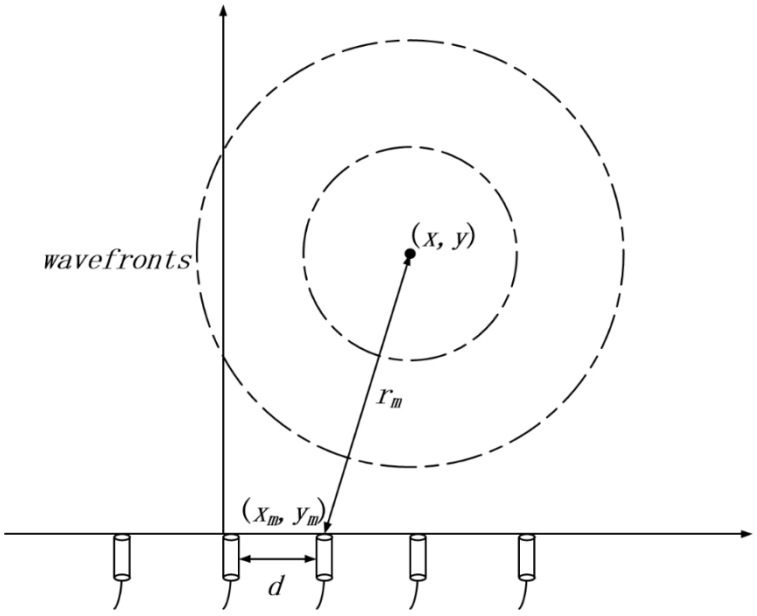

Figure 2.3 Spherical wave model.

Similarly, Figure 2.4 shows a DAS beamformer output computing by

MATLAB by adopting the spherical wave signal model. Since the near-filed assumption is adopted, the beamforming map is shown in 3-D in Figure 2.4(a).

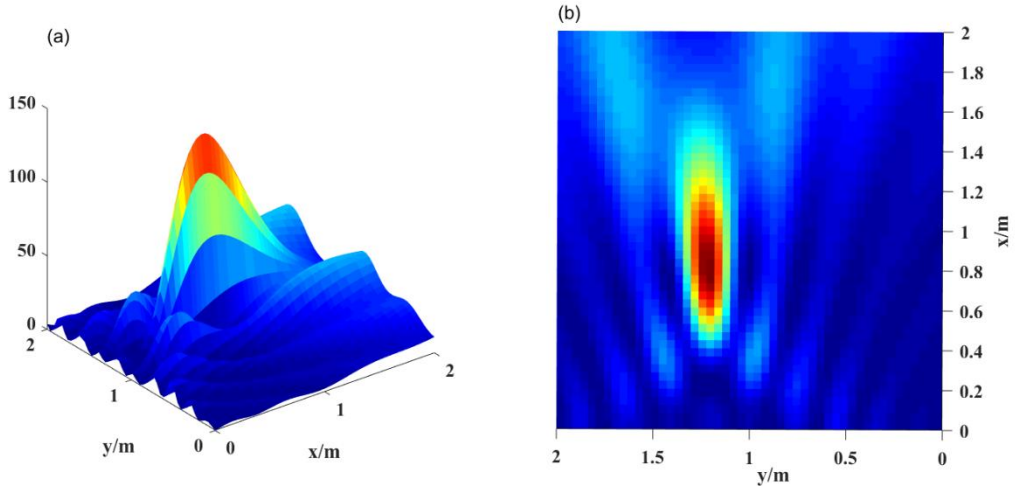

Figure 2.4 Beamforming result by adopting spherical wave signal model.

2.3 Theoretical formulation

To characterize the sound generated by fault on the wheel surface, the SK method is firstly considered, which can be combined with the beamforming technique in frequency-domain. In this section, SK is studied and improved by WT to achieve a better performance during indicating the fluctuating frequency band.

2.3.1 Spectrum kurtosis

Impact noise can be caused by faulty wheels during the train travelling. It is an impulsive, short duration pressure pulse with a peak amplitude. To characterize

such features, kurtosis is first considered to be investigated, which is a traditional statistical tool. It is a good indicator of signal impulsiveness in fault detection for rotating components, which is expressed as:

$$kurtosis(x) = \frac{E\left\{\left[x - \mu(x)\right]^4\right\}}{\left[\sigma(x)\right]^4} - 3 \tag{2.4}$$

in which $\mu(x)$ is the mean value of x, $\sigma(x)$ is the standard deviation of x, and E represents the expected value of the quantity (Y. Zhang et al., 2013). The "minus 3" at the end of equation 2.4 is to normalize the kurtosis of the normal distribution equal to zero (Y. Wang, Xiang, Markert, & Liang, 2016). Furthermore, a concept named SK can indicate the peakedness of a probability distribution associated to the instantaneous amplitudes of the time-series based on the normalized fourth-order moment of the magnitude of short-time Fourier transform (STFT) (Ottonello & Pagnan, 1994; Pagnan, Ottonello, & Tacconi, 1994). In the former researches, they also showed that SK could be used as a filter to recover random signals even when they are severely corrupted by additive stationary noise. This conclusion actually builds the foundation for the applications of SK to characterize the sound sources with impulsiveness. SK was initially defined as the kurtosis of its frequency components and was compared the variability in amplitude of the different spectral frequencies. Thus, this statistical parameter indicated how the impulsiveness of a signal varies with frequency (de la Rosa et al., 2013). An estimator of the SK based on the STFT was originally suggested in (Capdevielle, Serviere, & Lacoume, 1996; Dwyer, 1983, 1984, 1985; Ottonello & Pagnan, 1994; Pagnan et al., 1994), while its explicit deduction from a time-frequency approach

was given in (Antoni, 2004, 2006; Antoni & Randall, 2006):

For a process $Y(t)$ with an analysis window $w(n)$ of length N_w and a given temporal step size *P*, the STFT is written as:

$$Y_w(kP, f) = \sum_{n=-\infty}^{\infty} Y(n)w(n-kP)e^{-j2\pi nf} \tag{2.5}$$

The 2n-order empirical spectral moment of $Y_w(kP, f)$ is defined as:

$$S_{2nY}(f) = \left\langle \left| Y_w(kP, f) \right|^{2n} \right\rangle_k \tag{2.6}$$

with $\langle \cdot \rangle_k$ standing for the time-average operator over index *k*, hence the STFT-based estimator of the SK can be defined as:

$$K_Y(f) = \frac{S_{4Y}(f)}{S_{2Y}^2(f)} - 2 \tag{2.7}$$

To verify the effectiveness of using STFT-based SK method to identify the periodically impulsive signal, a simple experiment was conducted in anechoic chamber. A Gaussian impulse signal was generated by a loudspeaker with an interference background white noise. Figure 2.5(a) shows the recorded time domain signal of this case. It can be observed that the Gaussian impulse signal is totally merged in the background noise. Figure 2.5(b) shows the result of STFT-based SK method, which was coded by MATLAB. The protrusive peak in Figure 2.5(b) indicates that the recorded signals contain a dramatic fluctuation around 1135Hz, which means the domination frequency band of the Gaussian impulse signal should be around 1135Hz. Based on this inference, a band-pass filter with an 1130Hz to 1140Hz passband was applied to the original signal in Figure 2.5(a), and Figure 2.5(c) shows the result of the filtered signal. It shows that the merged

Gaussian impulsive signal appears from the background noise. Till then the impulsive feature of the original signal has been characterized by the SK method. To be noted that the SK results as a statistical parameter can only indicate how the impulsiveness of the original signal varies with frequency, yet the filtered result in Figure 2.5(c) is definitely not the original Gaussian impulse signal which was generated before.

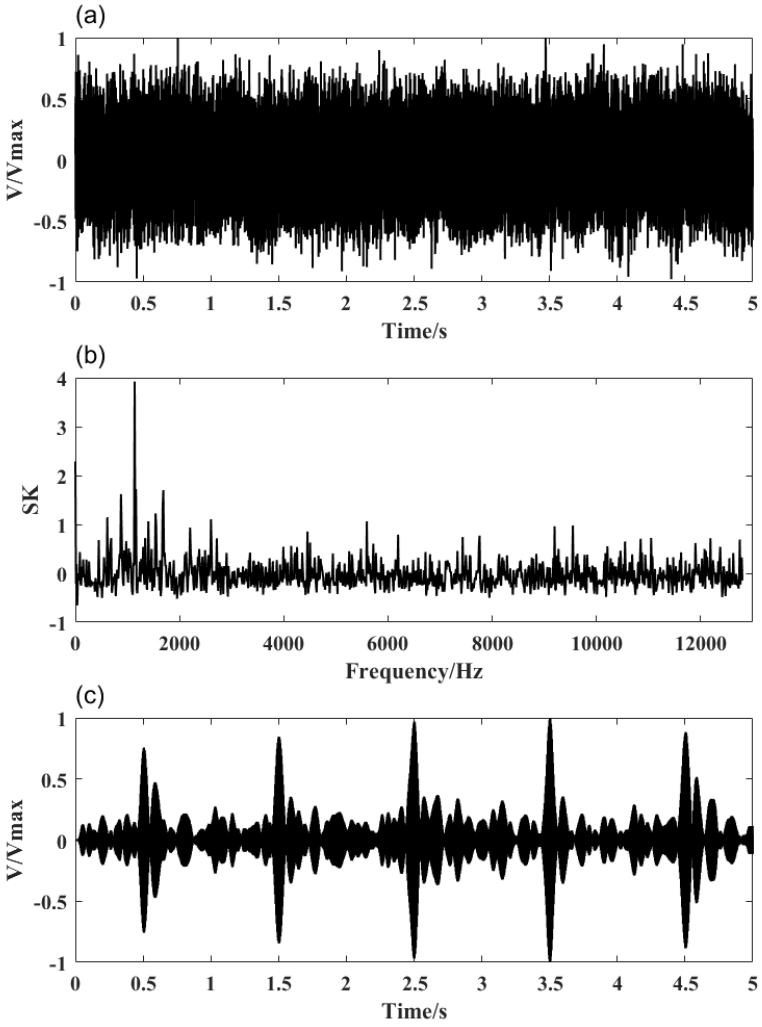

Figure 2.5 Signal processing by STFT-based SK method: (a) original signal in time-domain; (b) result of STFT-based SK; (c) filtered signal in time-domain.

The STFT approach in the SK calculation is usually used to determine the frequency variation over time of a signal, which is a traditional joint time-frequency analysis (JTFA) method. In this approach the entire time domain signal is divided into numerous small signals, each small signal is approximately smooth, and then the Fourier transform is implemented on each small signal, so that we can know what the frequency is at each moment. However, when the original signal is to be divided, the decision of the length of the window can be critical. The small window leads to a low frequency resolution while the big window leads to a low time resolution. To overcome this problem, another JTFA method, WT, which is rather popular at present was discovered by researchers (Daubechies, 1990; Nason & Silverman, 1995). An adaptive kurtosis filtering technique based on Morlet wavelet was developed, in which WT was used a filter bank (Liu, Huang, Wang, & Zhu, 2014). Compared with STFT, WT can overcome the problem of selection of time and frequency resolution significantly. It can be assumed justifiably as an alternative JTFA approach in SK calculation:

Recall the 2n-order empirical spectral moment of STFT outcome $Y_w(kP, f)$:

$$Y_w(kP, f) = \sum_{n=-\infty}^{\infty} Y(n)w(n-kP)e^{-j2\pi nf} \tag{2.5}$$

and the STFT-based estimator of the SK:

$$K_Y(f) = \frac{S_{4Y}(f)}{S_{2Y}^2(f)} - 2 \tag{2.7}$$

Based on which, the WT-based SK can be defined as:

$$K_{WT}(f) = \frac{S_{4W}(f)}{S_{2W}^2(f)} - 2 \tag{2.8}$$

similarly, in which the 2n-order empirical spectral moment of WT can be expressed as:

$$S_{2nW}(f) = \left\langle |WT(\tau, a)|^{2n} \right\rangle_k \tag{2.9}$$

and calculated via WT transform:

$$WT(\tau, a) = \frac{1}{\sqrt{|a|}} \int x(t) h * (\frac{t-\tau}{a}) dt \tag{2.10}$$

in which a is the scale and controls the expansion of wavelet function which can be transferred to frequency in practical application and τ is the translation time. The frequency corresponding to the scale satisfied:

$$F_{scale} = \frac{F_c F_s}{Scale} \tag{2.11}$$

in which F_c is the center frequency of wavelet basis and F_s is the sampling rate. According to the sampling theory, the frequency range should be $(0, F_s/2)$, so the scale range should be $(2F_c, \infty)$. New WT-based SK method was also coded by MATLAB and the corresponding SK result is shown in Figure 2.6. Compared with Figure 2.5(b), the further highlighted peak of frequency remains 1135Hz and the curve becomes rather smooth. To be noted that the selection of wavelet basis of WT approach can affect the shape of the curve in Figure 2.6 significantly during the simulation. It could lead another attractive research interest when combining the WT and SK method together.

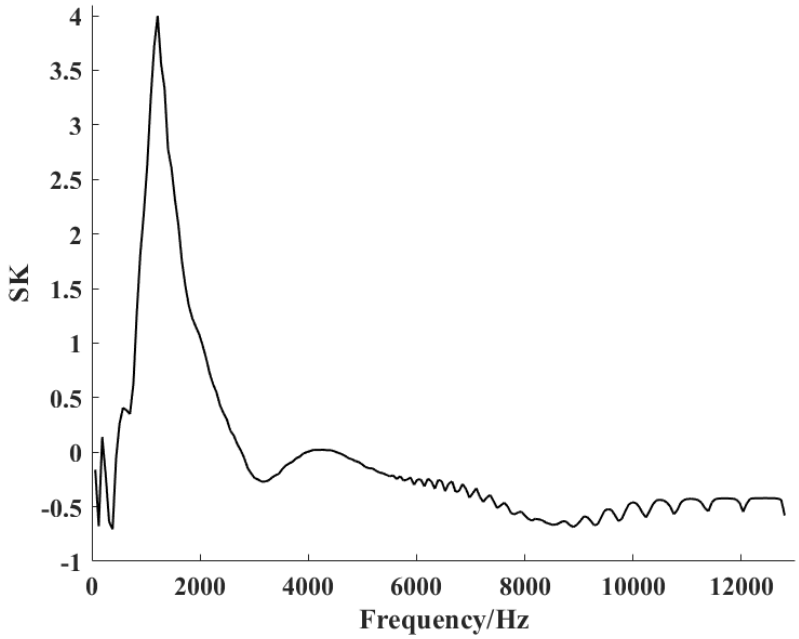

Figure 2.6 Result of WT-based SK.

Further theoretical studies were conducted to verify the robustness of the WT-based SK method. A Gaussian impulse signal was coded with exponential decay to imitate the impact signal in practice, which is expressed as:

$$s(t) = -2\pi^2 f^2 (t - 0.01n) e^{-2\pi^2 f^2 (t-0.01n)^2} \tag{2.12}$$

in which bandwidth $f = 400$ Hz . Figure 2.7(a) shows the exponential decay Gaussian impulse signal which composed of five simulated impact signals. In Figure 2.7(b) the original signal is totally merged into an additional background noise. By adopting the proposed WT-based SK method, Figure 2.7(c) shows the result indicated by a quite smooth curve. The protrusive peak in the curve suggests that the combined signal in Figure 2.7(b) contains a dramatic fluctuation frequency band around 480 Hz. Hence the band-pass filter with a 450 Hz to 500 Hz passband was applied to the combined signal, and Figure 2.7(d) shows the filtered signal

which can be observed that the merged impulsive signals appears from the background noise. Thus far the WT-based SK method was verified effectively both by simulation and experiment means.

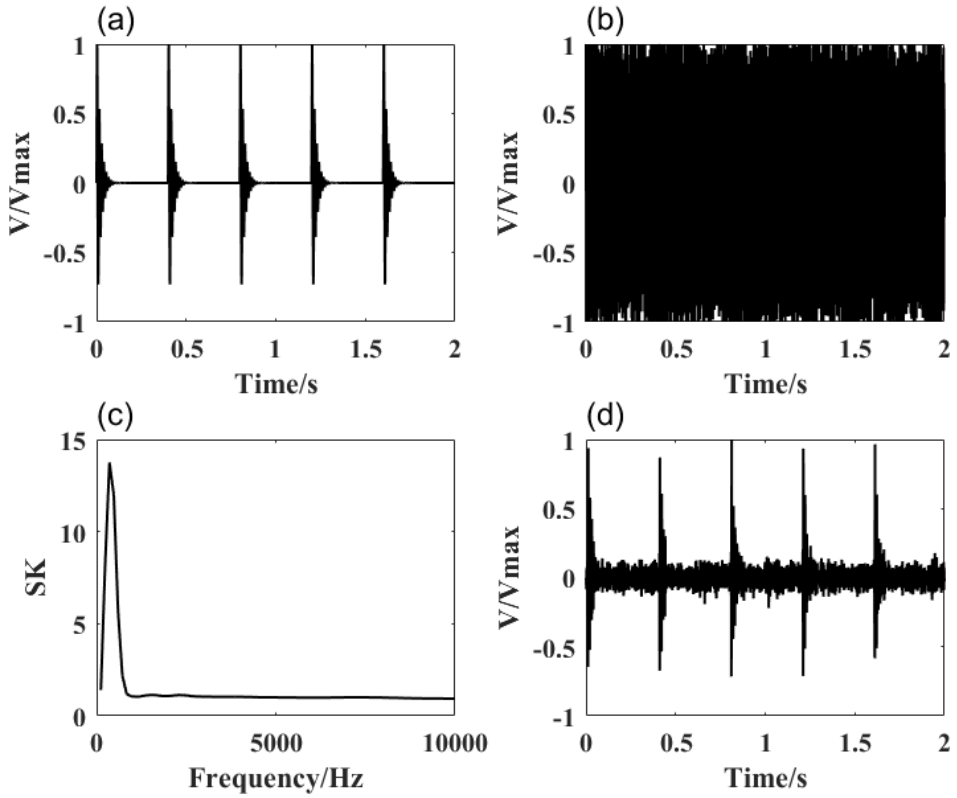

Figure 2.7 Signal processing by WT-based SK method: (a) original exponential decay Gaussian impulse signal; (b) original signal in time-domain; (c) result of WT-based SK method; (d) filtered signal in time-domain.

Since one of the objectives of this research is to distinguish the faulty wheel from pristine wheels in the wheel/rail system, and faulty wheel would generate the impact noise when it is rotating. The domination frequency band of an impact signal which calculated from the WT-based SK method should be applied in the

frequency-domain beamforming method to localize the faulty wheel in application. In fact, a team of researchers have used the SK and frequency-domain beamforming to detect the fault of each component in a complex rotating machinery system (Antoni, 2006; Cabada, Leclere, Antoni, & Hamzaoui, 2017). However, unlike the gearbox used in the former research, in the wheel/rail system, it is not straightforward to localize the faulty wheel by characterizing its domination frequency band. The impact signal generated by a wheel with uneven structural surface possesses the broad frequency feature. However, it is difficult to identify the appropriate frequency bands for calculating the SK of a broadband signal. Subsequently, the research findings indicate that the wheel faults can hardly be identified using the frequency-domain method.

Figure 2.8 shows the fast Fourier transform (FFT) results of the rotating faulty and pristine wheel in Figure 2.8(1a) and (2a), respectively. While the corresponding SK results are shown in Figure 2.8(1b) and (2b). We can see the dominate frequency band is around 200-800 Hz. By using a frequency-domain beamformer, one single faulty wheel could be easily located. This method was verified in Prof. Antoni's work. But the problem is the frequency distribution of a pristine wheel is quite similar to that faulty one. That is because the rolling and impact noise generated by a pristine wheel and faulty wheel share the same vibration media. They are both generated due to the unevenness of the wheel surface, and the difference between them is the dimension of the unevenness. Therefore, their dominate frequency bands calculated by spectrum kurtosis are

almost the same. Resulting from those occurrences, it is difficult to identify an appropriate frequency bands for the frequency-domain beamforming to localize the faulty wheel. As we know, when a frequency-domain beamformer is applied, a specific frequency must be chosen during computing. That means if we put a faulty wheel and a pristine wheel together, we cannot distinguish them by frequency-domain beamforming due to their same dominate frequency band. Because we can not ensure that the amplitude of faulty wheel is always larger than the pristine wheel. In such case, a frequency-domain beamformer would indicate the location with larger sound power at that specific frequency, not the faulty/pristine wheel. The main differences between these two curves are the values of kurtosis. Since the kurtosis value is a time-domain character, and it could be indicated by a time-domain beamformer. So, we decide to make use of the kurtosis value in time-domain instead of spectrum kurtosis.

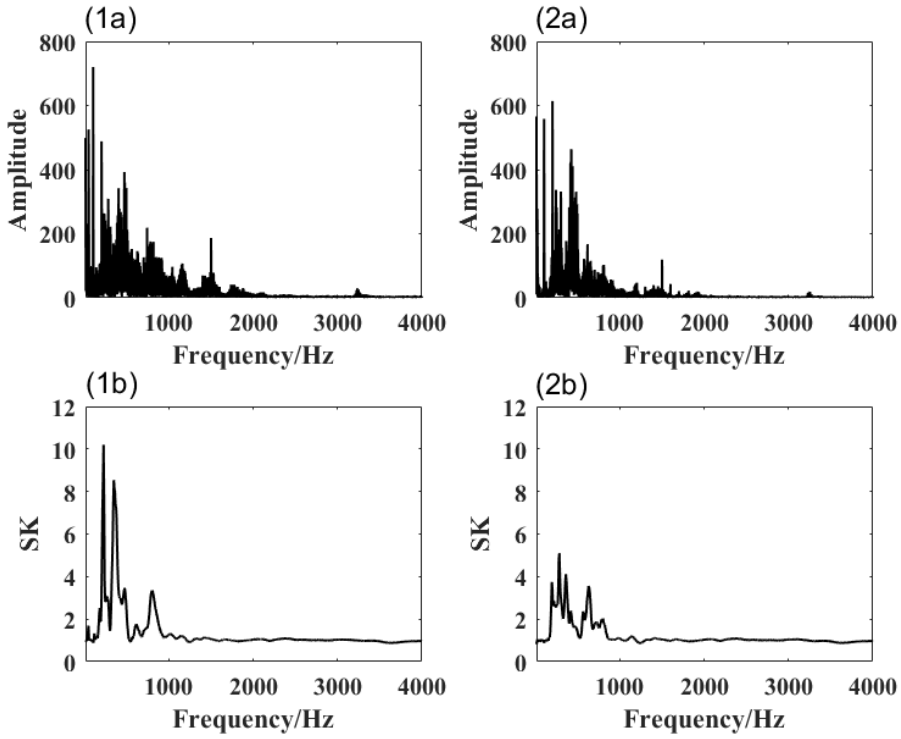

Figure 2.8 FFT and SK result comparisons of faulty and pristine wheel: (1a) and (1b) faulty wheel; (2a) and (2b) pristine wheel.

2.3.2 Time-domain beamforming

Since the SK method can only indicate the impulsive signal from stationary signals but can not distinguish the impact noise from the rolling noise in the wheel/rail system. Kurtosis is considered to be utilized as a time-domain statistic indicator, which could be combined with the time-domain beamforming method. Time-domain analysis can be utilized for real-time identification of sound sources. In fact, the time-domain beamformer is the original form of beamforming that has been used since World War I (Michel, 2006). However, time-domain beamforming requires a large amount of computing operation in the analysis procedure. Rare algorithm was discovered in the past several years expect the traditional DAS beamformer. The algorithms in frequency-domain including LCMV and MUSIC based on the correlation matrix **R** can not apply to the time-domain directly. Although the beamforming technology has been developed for decades, it remains a complicated task to localize and characterize the sound sources in specific industrial occasions. For instance, in wheel/rail system, background noise interference can be serious, and sound sources are usually moving. Meanwhile, the ground reflection must be considered during fault localization and detection approach. In this perspective, this study attempts to fill this gap to remain valid in

such occasions in the wheel/rail system.

As it shown in Fig. 1, if a pure-tone sound source of frequency ω is located close to a ULA consisting *M* microphones arranged at x axis, the wavefront of the sound from the sound source should be considered curved when it is observed over the microphone array. The sound pressure signals received at the microphone array can be expressed as:

$$\mathbf{p}(\omega) = [\, p_1(\omega) \quad p_2(\omega) \quad \cdots \quad p_M(\omega)]^T \tag{2.13}$$

The beamforming method assumes that the wavefront can be expressed by a positional parameter r_m, which is the distance between the source and the *m*th microphone in array. A straightforward way to extract such a certain parameter from the given measurement data is to introduce a scan vector that depends on r_m by defining a weighting function in spherical wavefront model given by:

$$\mathbf{w}(r_m, \omega) = \frac{1}{M}[w_1(r_m, \omega) \quad w_2(r_m, \omega) \quad \cdots \quad w_M(r_m, \omega)]^T \tag{2.14}$$

in which

$$w_m(r_m, \omega) = e^{-i\omega\frac{r_m}{c}} \tag{2.15}$$

and

$$r_m(x_m, y_m) = \sqrt{(x - x_m)^2 + (y - y_m)^2} \tag{2.16}$$

where *m* is the index of each microphone (*m*=1, …, *M*), *c* is the representative of sound speed, and the superscript *T* represents the transpose of a vector or matrix. Using the defined weighting function $\mathbf{w}(r_m, \omega)$ and the received sound pressure signals $\mathbf{p}(\omega)$, the frequency-domain beamformer output in near-field can be written as:

$$b(r_m,\omega)=\mathbf{w}(r_m,\omega)^T\mathbf{p}(\omega) \tag{2.17}$$

The time-domain representation of the beamformer weighting function can be derived from the inverse Fourier transform (IFT) of equation 2.15, which is given by:

$$\begin{aligned} w_m(r_m,t) &= \frac{1}{M}\cdot\frac{1}{2\pi}\int_{-\infty}^{\infty} e^{-i\omega\frac{r_m}{c}}e^{-i\omega t}d\omega \\ &= \frac{1}{M}\delta(t+\frac{r_m}{c}) \end{aligned} \tag{2.18}$$

Equation 2.18 indicates that the measured signal $p_m(t)$ could be impressed as a function which is filtered by a delta function with a certain time delay. The time domain beamforming scan vector and received signal can be expressed in matrix form by defining two partitioned vectors consisting of $\mathbf{w}(\tau)$ and $\mathbf{p}(t+\tau)$ at each time instance $\tau = n\Delta t$:

$$\hat{\mathbf{w}}(r_m)=\begin{bmatrix}\mathbf{w}(r_m,0)\\ \mathbf{w}(r_m,\Delta t)\\ \vdots\\ \mathbf{w}(r_m,(N-1)\Delta t)\end{bmatrix},\hat{\mathbf{p}}(t)=\begin{bmatrix}\mathbf{p}(t)\\ \mathbf{p}(t+\Delta t)\\ \vdots\\ \mathbf{w}(t+(N-1)\Delta t)\end{bmatrix} \tag{2.19}$$

Then the beamformer output can be defined by:

$$\begin{aligned} b(r_m,t) &= \hat{\mathbf{w}}(r_m)^T\hat{\mathbf{p}}(t) \\ &= \sum_{m=1}^{M}\sum_{n=0}^{N-1} w_m(r_m,n\Delta t)p_m(t+n\Delta t) \\ &= \sum_{m=1}^{M}\int_{-\infty}^{\infty}\left[\omega_m(r_m,\tau)\,p_m(t+\tau)\right]d\tau \end{aligned} \tag{2.20}$$

Using the integral of the time-delayed Dirac delta function $\int_{-\infty}^{\infty} f(t)\delta(t-T)dt = f(T)$ to solve the integration in equation 2.20 presents the near-field time-domain beamforming output:

$$b(r_m, t) = \frac{1}{M} \sum_{m=1}^{M} p_m (t - \frac{r_m}{c}) \tag{2.21}$$

In general, the time-domain beamforming is always considered computationally inefficient, on the other hand, the frequency-domain beamforming by using FFT can operate faster in real-time. But when only a pure time delay is considered, the formula of time-domain beamforming is straightforward, and its processing can emphasize the temporal characteristics of the source signal. This property can be serviceable when fault detection is conducted.

2.3.3 Kurtosis beamformer

In statistics, kurtosis is a measure of the peakedness of a variable. A higher kurtosis value of a signal is the result of its larger deviations in the time history. Three different typical signals were generated, and their kurtosis values were compared in Table 2.1. The rectangular wave and sine wave are typical low kurtosis distributions. The deviations of their time history were less than the normal distribution. Similar to other univariate normal distributions, the kurtosis value of white noise is 3. The impulsive signal was adopted to imitate the impact noise generated by the imperfections of rotating mechanisms. Further, its kurtosis value was extremely higher than those of the rectangular wave, sine wave, or white noise.

Table 2.1

Different signals and their kurtosis values.

Type of signal	Kurtosis value
Rectangular wave	1.000
Sine wave	1.500
White noise	3.0280
Gaussian impulses	98.5976

Researchers have tried to use statistic tools to represent the beamforming output before (Kim & Choi, 2013). Peak value has been proposed to use as an alternative estimator in time-domain beamforming technique for locating impulsive sound source (Seo et al., 2014). In the previous study, the performance of peak value and RMS value were investigated and compared when the measured signals are embedded in noise, and the impulsive noise source is modeled as a triangular pulse. The simulation results showed that the peak value estimator of beamformer output determines the location with a better spatial resolution and a lower SLL than RMS value. Considering kurtosis has been widely used in fault detection of bearings and its ability to measure the flatness when comparing a probability distribution with a normal distribution, it should be used as another alternative estimator when localising the impulsive signals. The kurtosis-based time-domain beamformer will be introduced below, and the comparison among the kurtosis, RMS and peak value will be given in the next chapter.

Recall the near-field time-domain beamforming output:

$$b(r_m,t)=\frac{1}{M}\sum_{m=1}^{M}p_m(t-\frac{r_m}{c}) \tag{2.21}$$

The RMS value of the beamforming output $b(r_m,t)$ is called the beamforming power, which can be written as:

$$\beta(r_m,t)=E[|b(r_m,t)|^2] \tag{2.22}$$

Similarly, the kurtosis of the DAS beamformer output $b(r_m,t)$, which is named kurtosis beamformer, is as follows:

$$Kurt(r_m)=\frac{E\left(\left\{b(r_m,t)-\mu\left[b(r_m,t)\right]\right\}^4\right)}{\left\{\sigma\left[b(r_m,t)\right]\right\}^4} \tag{2.23}$$

It is noteworthy that unlike the conventional beamforming power, the kurtosis beamformer in the current study is dimensionless.

2.4 Experimental validation

To simulate the real wheel/rail system, a rotating machinery system was designed and constructed as shown in Figure 2.9. The system was composed of two rollers and two different shafts. One shaft of diameter 25 mm was coupled with a cast iron wheel of diameter 200 mm that served as the rail, and one shaft of diameter 20 mm also was coupled with a cast iron wheel of diameter 150 mm that served as the wheel. Both shafts were driven by 60 W/220 V direct current (DC) motors (5IK60RGU-CF) with decelerators (5GU-3K). Belt transmission and universal coupling were applied to the roller test rig to ensure that the motion of the wheel with wheel-flat possessed enough space. The different speeds of the two

shafts could be achieved by speed control switches that were attached with DC motors and an optical tachometer. The test rig was used to demonstrate the rotating motion of the wheel and the impact between the wheel and rail when the train operated. The whole test rig occupied a small space and was easy to handle; therefore, the experiments could be conducted in an anechoic chamber.

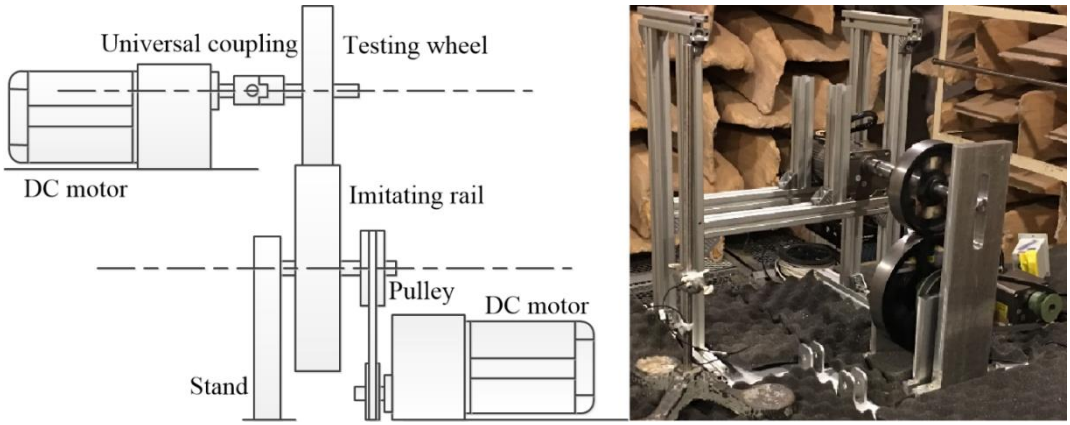

Figure 2.9 Sketch and snapshot of roller test rig.

Experiments were conducted to investigate the performance of time-domain beamforming integrated with kurtosis. All experiments were performed in an anechoic chamber with a background noise level of less than 15 dBA, and a cut-off frequency of 80 Hz to avoid sound reflections from the surrounding boundaries. Two experimental cases are discussed in the following content. Figure 2.10 shows one of the experimental setups of the roller test rigs. A loudspeaker of diameter 9 cm was used to generate the background noise, while two roller test rigs that generated the impact noise and rolling noise were placed in the anechoic chamber. In the experiments, an array of sixteen microphones was aligned linearly with the

microphone separation of 0.1 m. The array was placed 1.3 m above the floor and at 0.7 m perpendicular to the sound sources. The acoustic signals were captured by 16 Brüel & Kjær 9854 microphones, and amplified by a Brüel & Kjær Type 2694-A 16-channel DeltaTron conditioning amplifier. The analogue signals were converted into digital signals by four NI 9234 four-channel data acquisition cards.

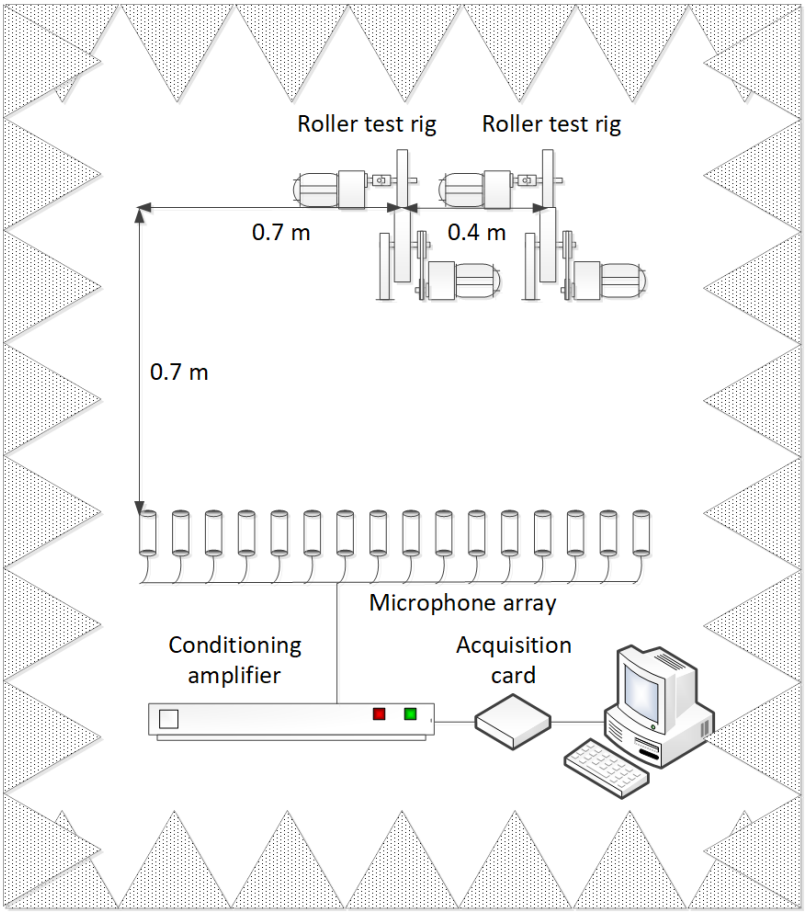

Figure 2.10 Experimental setup.

Figure 2.11 shows the comparison between the result for the location of the fault by the traditional DAS beamformer, and that by the kurtosis beamformer. The roller test rig carrying a wheel with wheel-flat was installed at (0.7 m, 0.7 m), while

another roller test rig carrying the wheel without fault was placed at (1.1 m, 0.7 m). Figure 2.11(a) shows the time-domain beamforming power and Figure 2.11(b) shows the time-domain kurtosis beamformer. The number of averaging is the number of microphones. We didn't use any windows in the data processing and no overlaps was used, too. Without the interference by the background white noise in this case, the location of the two sound sources due to the wheel system operation can be observed clearly in Figure 2.11(a). The beamformer power at the location of the wheel without fault (square) is slightly less than that of the wheel with fault (diamond). Meanwhile, Figure 2.11(b) shows that the kurtosis beamformer of the wheel with fault is significantly higher than that of the wheel without fault. This means that the sound map of the beamforming integrated with kurtosis is more effective at revealing the location of the wheel-flat and concealing the location of the normal wheel.

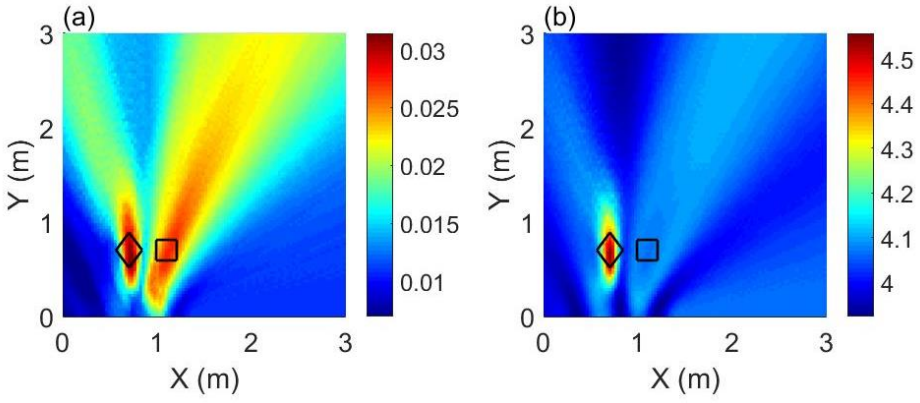

Figure 2.11 Fault detection and localisation results of wheel with wheel-flat (◇: wheel-flat, and □: without fault): (a) DAS beamforming power; (b) kurtosis beamformer.

The geometric experimental setup of the second case is shown in Figure 2.12. In this case, the arrangement of microphone array and the data acquisition system is retained the same as the former case. The parallel distance between the microphone array and the sound sources was changed to 1.2 m. As the figure shows, an interference noise source was added into the sound field. The three sources had an equidistance which is 0.6 m.

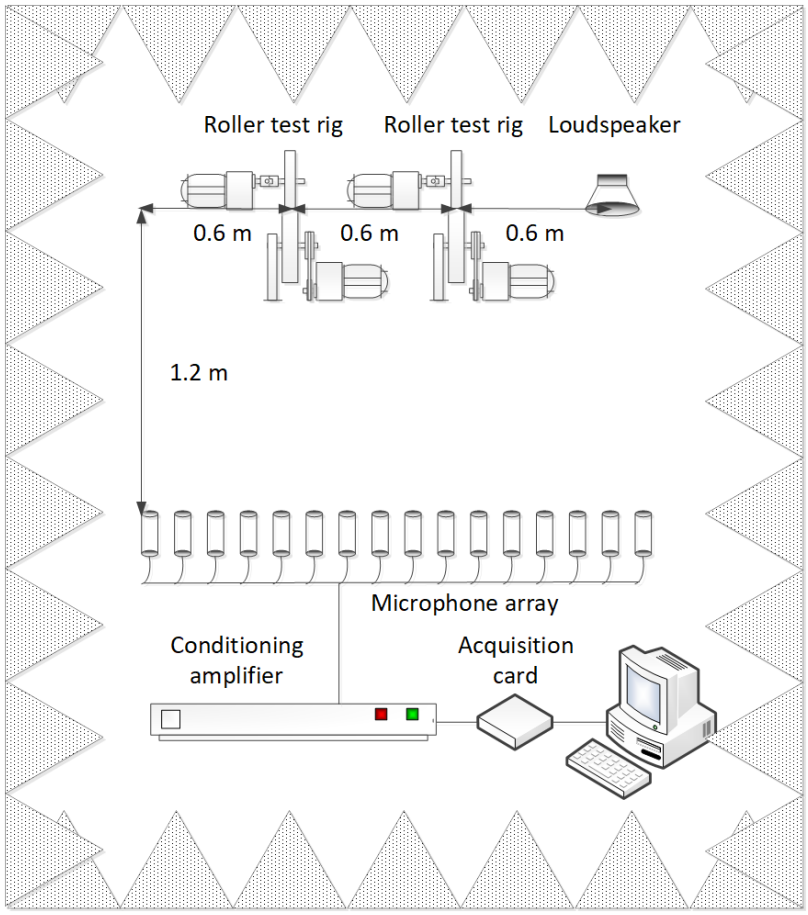

Figure 2.12 Experimental setup.

Figure 2.13 shows the comparison between the DAS and kurtosis beamformer.

In Figure 2.13(a), two indistinct sound sources and one definite sound source can be discovered in the sound map. That is because to verify the effectiveness of the proposed kurtosis beamformer, the amplitude of the interference noise (1.8 m, 1.2 m) was set to be higher than the impact (1.2 m, 1.2 m) and rolling (0.6 m, 1.2 m) noise. What needs to be pointed out is that the kurtosis beamformer would fail if the SNR is extremely low. The criteria od such situation will be thoroughly discussed in the next chapter. In the Figure 2.13(b) both the rolling noise and background noise were suppressed, on the other hand the impact noise generated by faulty wheel was protruded. The result is consistent with the former case.

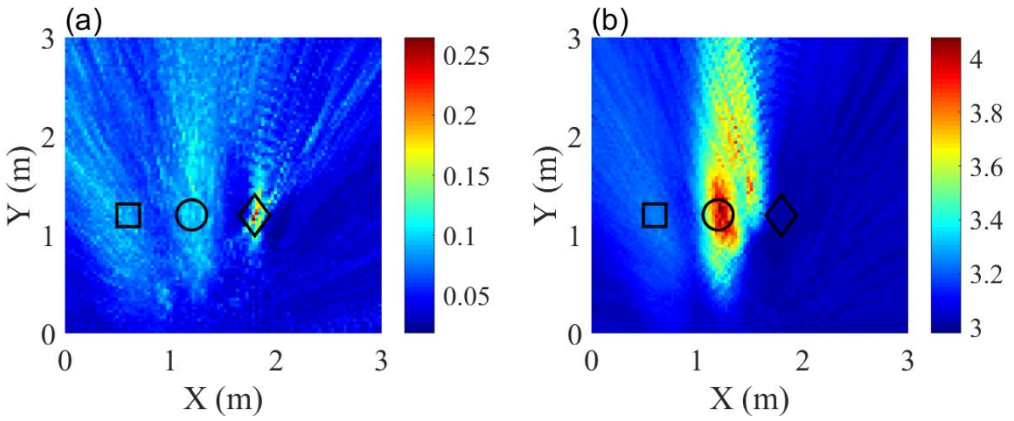

Figure 2.13 Fault detection and localisation results of wheel with wheel-flat (□: without fault, ○: wheel-flat, and ◇: interference noise): (a) DAS beamforming power; (b) kurtosis beamformer.

2.5 Chapter summary

Firstly, signal models in far-field and near-filed assumptions have been

established in this chapter, including plane wave model and spherical wave model. Based on the signal models, the presentation of traditional beamforming method is introduced.

To characterize the impact noise from rolling noise, SK and kurtosis are studied theoretically. SK method can significantly indicate the frequency band of the impact noise. Compared to the STFT-based SK method, the main advantage of the proposed WT-based SK approach is the smooth curve and the outstanding peak. Considering the impact noise is actually an extreme case of the rolling noise, the frequency band of these two noises is almost the same. Thus, an integrated method combined beamforming and kurtosis in time-domain is proposed. A compared experimental study has been conducted between the time-domain DAS beamformer and kurtosis beamformer. Differ from the traditional DAS beamformer, kurtosis beamformer is feasible to trace the location of the wheel with fault from the pristine wheel under the condition of background noise.

It is important to note that in the Section 2.4, we use the peak kurtosis value in sound map to indicate the location of the faulty wheels, which is about 4 to 4.5. It is not a large number compared with the kurtosis value shown in Table 2.1 and Figure 2.8 during the theoretical formulation. However, the kurtosis value of white noise and pristine wheel are still closer to 3, so the difference between 3 and 4 is major enough to distinguish the faulty wheel in the experiments. The additional relevant experimental validations and the baseline to determine the existence of a fault would be shown in the next section.

CHAPTER 3

Extensional discussion of kurtosis beamformer

3.1 Introduction

In this chapter, the proposed kurtosis beamformer is further investigated in many respects, including the types of fault (S. Grassie & Kalousek, 1993; S. L. Grassie, 2005; Johansson, 2006; Nielsen & Johansson, 2000; Wu & Thompson, 2002), the influence of SNR and duration of data acquisition. At first, the kurtosis beamformer is expected to be a monitor method at the early-stage of the fault formation (Pal, Daniel, & Farjoo, 2013). Therefore, different types of faults in different stages would be tested in the fault detection approach. Dent, squat and wheel-flat were chosen in the following experiments to be the representatives of different faults, while the different dimensions of the fault could be regarded as the different stages of which. The kurtosis value of those faults and the corresponding performance would be introduced in the Section 3.2.

Meanwhile, the kurtosis beamformer is compared with the current state-of-the-art methods in two respect. As a statistics estimator, kurtosis is compared with

the RMS and peak value during the localization of impulsive signals. As a structural condition monitoring technique, kurtosis beamformer is compared with the other non-destructive testing (NDT) techniques. Since the examined signals and the logics of fault identification of those techniques are very different, this part of comparison would be stated in forms instead of experimental validation.

In the end, the results of the discussion of influence of SNR and duration of data acquisition would provide an explicit criterion of the utilization of kurtosis beamformer.

3.2 Identification of different types of faults

Three types of faults were created on the wheel to simulate the structural damages including dent, squat, and wheel-flat. Their snapshots and corresponding raw time-variant acoustic signals (in terms of voltage normalized by the maximum voltage) measured by one of the microphones when the two wheels were rotating together are shown in Figure 3.1. Figure 3.1(1a) shows the snapshot of the wheel without faults, while Figure 3.1(2a), (3a), and (4a) show the snapshots of the wheel with the fault of dent, squat, and wheel-flat, respectively. Figure 3.1(3a) and (4a) show that the faults on the wheel surface are severe, and the impulsiveness of the signals in Figure 3.1(3b) and (4b) are obvious. However, it is difficult to distinguish between the signal of the dented wheel in Figure 3.1(2b) and that of the wheel without fault in Figure 3.1(1b) by observation. To solve this problem,

the kurtosis value is more appropriate to reflect the severity of the fault. This type of fault with less significant signals can be regarded as one of the early stage faults on the contact surfaces. To eliminate the potential safety issues, more efforts to conduct faults detection at the early stage should be performed.

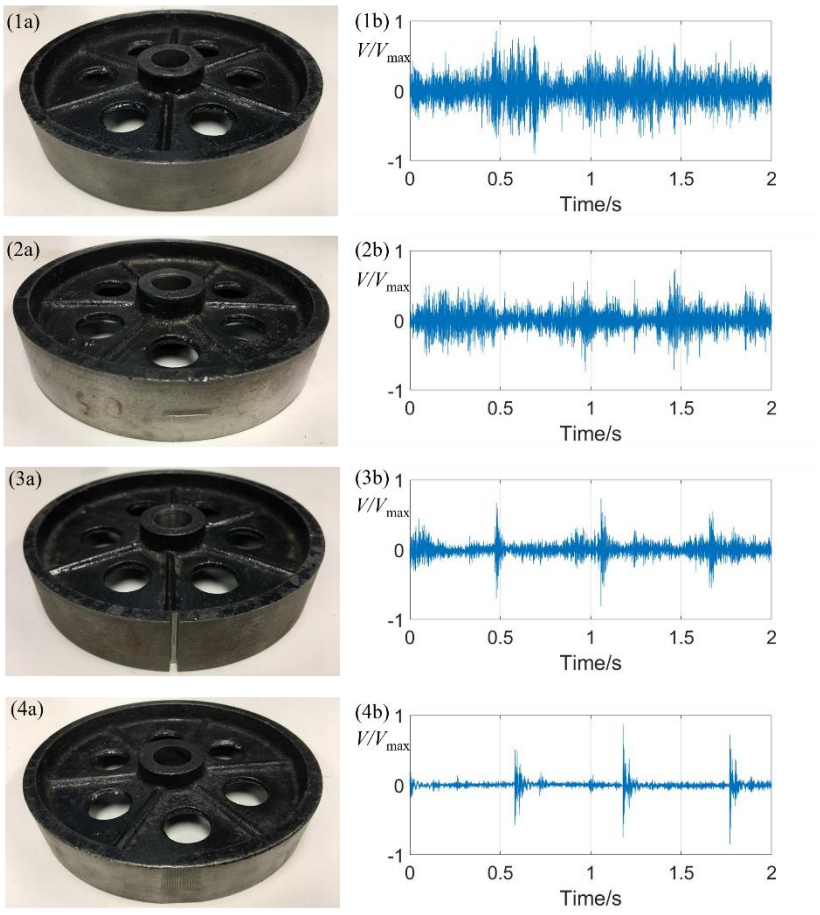

Figure 3.1 Snapshots and time-domain signals of wheel without fault. (1a) snapshot of wheel without fault, (1b) signal of wheel without fault; (2a) snapshot of wheel with dent, (2b) signal of wheel with dent; (3a) snapshot of wheel with squat, (3b) signal of wheel with squat; (4a) snapshot of wheel with wheel-flat, (4b) signal of wheel with wheel-flat.

Different raw wheel fault signals with their kurtosis values are shown in Table 3.1. The measurements were repeated 20 times. To ascertain the fault level by the kurtosis value, a pure random noise signal from the loudspeaker, which was regarded as reference data, was generated for comparison and it yielded a kurtosis value of approximately 3. The first, second, and third columns of Table 3.1 indicate the fault type, kurtosis value, and standard deviation among all the tests, respectively. The fourth column indicates the relative sound pressure level (SPL) comparing the signals of the wheel with faults with the signal of the wheel without fault. In the reference paper (Pal, Daniel, & Farjoo, 2013), a fine depression is regarded as an early stage fault. To simulate the early stage fault, we engrave an almost slight dent on the wheel surface. Around 0.2 mm to 2 mm, for example. The rolling noise radiating from the wheel without fault yielded the kurtosis value of approximately 3.98, while that from the wheel with a 0.2-mm dent yielded the kurtosis value of approximately 4.5. This reflects that the small-sized dent, which cannot be identified from the time-variant data, can be recognised based on the kurtosis analysis. The kurtosis values of the squat and wheel-flat were significantly larger than that of the dent. Moreover, when the wheel faults were larger or became more serious, the kurtosis values became larger. Therefore, it is possible to determine the severity of the wheel faults and locate the faults using the kurtosis beamformer.

Table 3.1

Different types of wheel faults and their kurtosis values.

Type of signal	Kurtosis value	Standard deviation	Relative SPL (dB)
Random noise	3.0078	0.0128	N/A
Wheel without fault	3.9802	0.0342	+0.00
Dent (depth=0.2 mm)	4.5731	0.0686	+0.12
Dent (depth=0.5 mm)	4.6384	0.0497	+0.85
Dent (depth=2 mm)	4.2965	0.0629	+1.38
Squat	8.7016	0.3590	+2.09
Wheel-flat (depth=0.5 mm)	9.3195	0.4161	+2.75
Wheel-flat (depth=1 mm)	43.1276	2.3221	+4.92
Wheel-flat (depth=2 mm)	44.4229	1.2782	+7.91

To further investigate the performance of the proposed method in the noisy environment, the effect of different SPL of background white noise was added in this case. Thus, in sound field, a loudspeaker was placed at (0.3 m, 0.7 m) as it is shown in Figure 3.2 to generate a white noise.

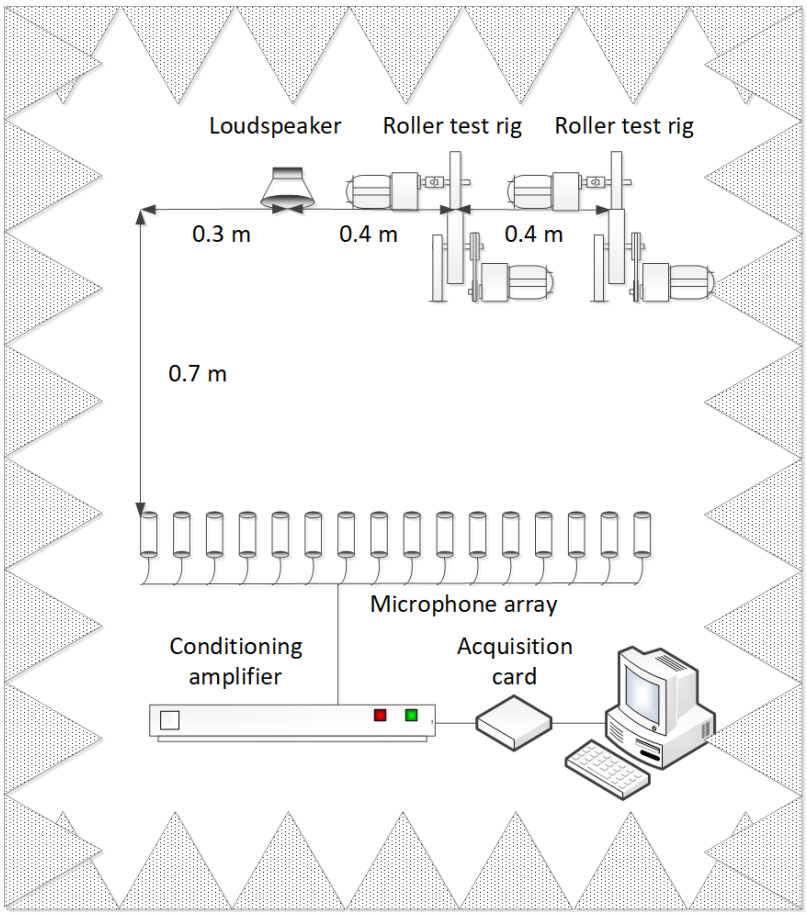

Figure 3.2 Experimental setup.

The identification and localization results of different types of faults are shown in Figure 3.3. The first and second columns of Figure 3.3 show the time-domain beamforming power and time-domain kurtosis beamforming, respectively. The first, second, and third rows of Figure 3.3 show the localisation result of the wheel without fault and with the fault of dent, squat, and wheel-flat, respectively, under the background noise. In addition, the symbol of diamond, square, and circle show the actual location of the loudspeaker, the wheel without fault, and the wheel with fault, respectively. Figure 3.3(1a) shows that the locations of the wheel with and without fault are vague, and it is difficult to identify these two types of sound

sources. However, the location of the speaker appears to be clearer and identifiable from the sound map. This is primarily because of the SPL of background noise being higher than that of other two types of sound sources. Meanwhile, the location of the wheel with dent can be recognised approximately from the map of the kurtosis beamforming, as shown in Figure 3.3(1b), while the location of the speaker and the normal wheel cannot be identified. According to the literature, the size of roughly about 0.2 mm dent which is a fine depression at the rail surface is considered as an early stage of crack initiation and propagation (Pal et al., 2013). In this regard, the kurtosis value 3.8 attributed to the dent with the same size which can reflect the early stage of faults on the wheel surface is considered as the baseline to determine the existence of the fault in the sound map. Similarly, Figure 3.3(2a) and (3a) show a vague beamforming map; therefore, the location of the wheel with fault cannot be identified. Figure 3.3(2b) shows a clear kurtosis beamformer map such that the location of the wheel with squat can be recognised. Figure 3.3(3b) depicts that the location of the wheel with the fault of wheel-flat is clear, and it is more acceptable than the dent and squat detections shown in Figure 3.3(1b) and (2b). This is because the kurtosis value of the dent is slightly larger than that of the wheel without fault; additionally, some sidelobes can be observed in Figure 3.3(1b).

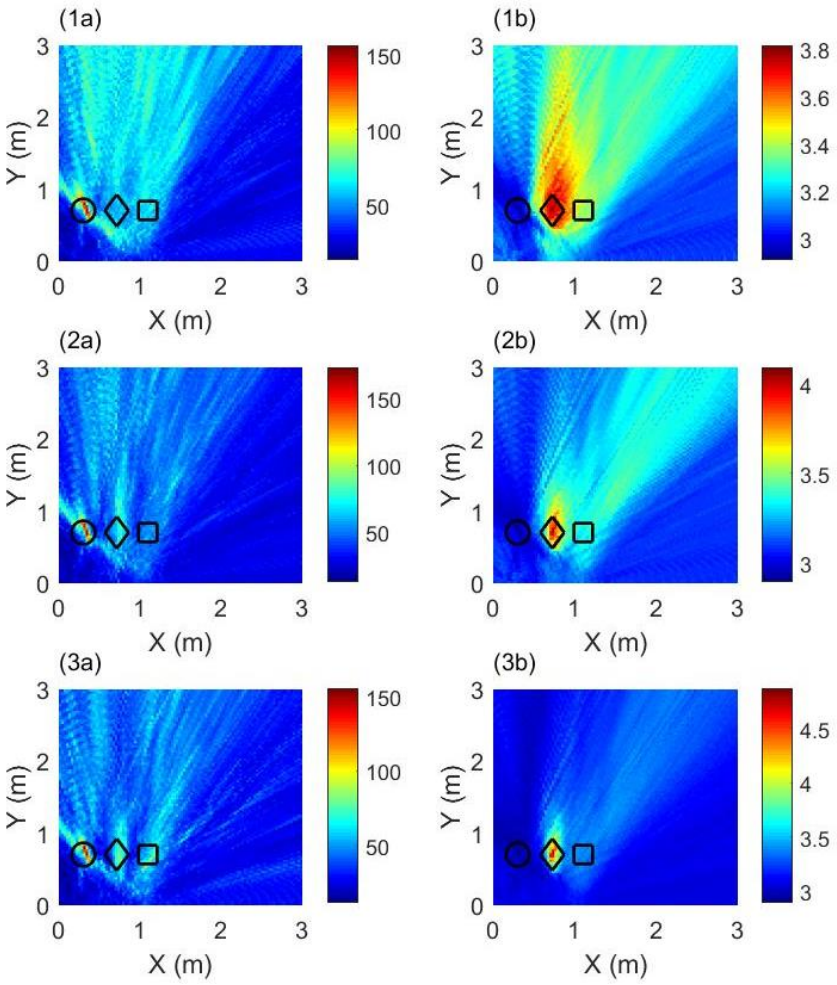

Figure 3.3 Fault detection and localisation results (○: background noise, ◇: wheel with fault, and □: wheel without fault): (1a) DAS beamforming power of wheel with dent; (1b) kurtosis beamforming of wheel with dent; (2a) DAS beamforming power of wheel with squat; (2b) kurtosis beamforming of wheel with squat; (3a) DAS beamforming power of wheel with wheel-flat; (3b) kurtosis beamforming of wheel with wheel-flat.

3.3 Comparison with current state-of-the-art approaches

3.3.1 Comparison of statistics estimators

Generally, kurtosis can be applied as a time-domain beamforming estimator to detect the impulsive signals generated by the impact of wheels with the fault in the wheel/rail system. Figure 3.4 shows the comparison of the maps of the time-domain beamformer evaluated by different statistic estimators, and the experimental setup is the same as it is shown in Figure 3.4. The first, second, and third columns of Figure 3.4 show the result of the RMS, peak value, and kurtosis value, respectively, for the localisation of the speaker, the pristine wheel and the wheel-flat. The second row of Figure 3.4 shows the variation in amplitude of the corresponding beamforming estimator along the axial direction for Y=0.7 m. A study of the impulsive sound source localisation shows that the peak value is better than the RMS as a statistic estimator to locate the sound source using the beamforming approach, owing to the achievement of a narrower beamwidth and a lower SLL (Seo et al., 2014). In the present case of the localisation of an impulsive signal, the kurtosis value performed better than the peak, as observed in Figure 3.4(3b) and (2b), respectively. The use of RMS estimation is to calculate the total sound power. Figure 3.4(1b) shows that the signal of the wheel-flat is weak with a low power level. Nevertheless, the kurtosis value is regarded as a better estimator to enhance the wheel-flat signal with respect to the background noise in Figure 3.4(3b). Consequently, kurtosis can be more advantageous than the RMS and peak value for the detection and localisation of a single impulsive sound source.

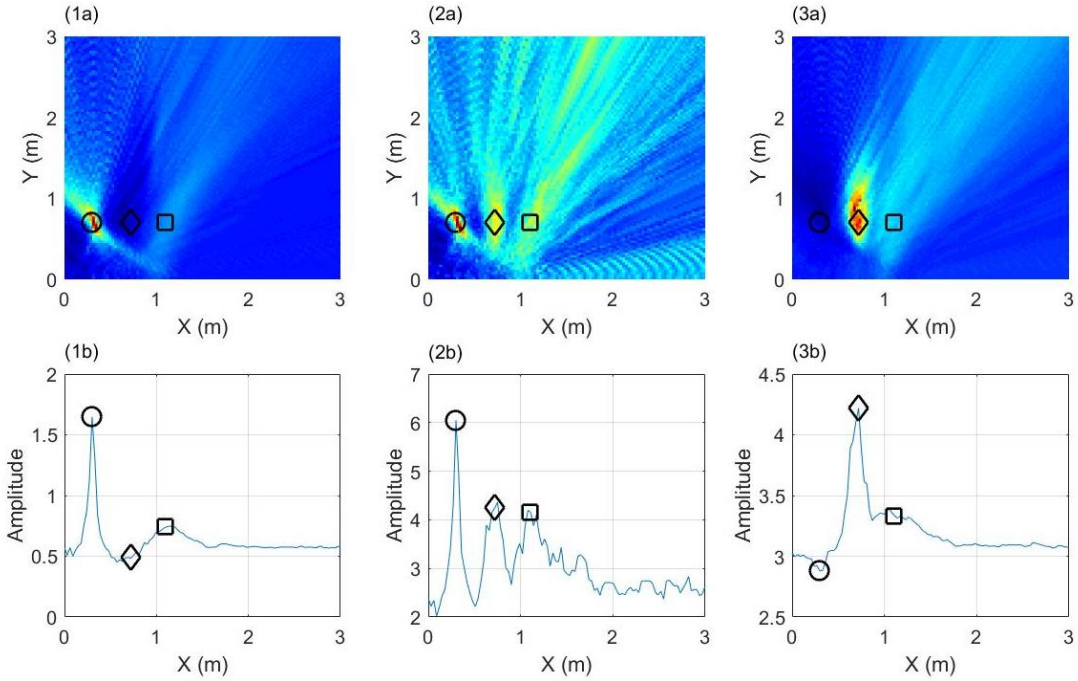

Figure 3.4 Fault detection and localisation results using different statistic estimators (○: background noise, ◇: wheel with wheel-flat, and □: wheel without fault): (1a) RMS value; (1b) vertical view for RMS value at Y = 0.7 m; (2a) peak value; (2b) vertical view for peak value at Y = 0.7 m; (3a) kurtosis; (3b) vertical view for kurtosis at Y = 0.7 m.

3.3.2 Comparison of NDT techniques

In this section, the proposed kurtosis beamforming method is compared with current state-of-the-art fault detection approaches. The results are tabulated in Table 3.2. All the structural condition monitoring approaches use NDT techniques (Beebe, 1995; Dornfeld & Cai, 1984; Drinkwater & Wilcox, 2006; Fan, Su, Meng, & He, 2014; Fassois & Sakellariou, 2007; Matsumoto et al., 2008;

Peng & Kessissoglou, 2003; Salzburger et al., 2009; Su et al., 2006). In traditional vibration testing, accelerometers are mounted on the structure, and displacement and velocity are analysed with different frequency/time domain techniques. During this testing, the displacement and velocity of the structural component can easily be interfered by the vibration of the whole system. Magnetic or ultrasonic methods are a preferred solution to address this problem. Ultrasonic wave can travel over a long distance in materials with a high attenuation ratio, and be easily changed by damages or boundaries on its propagation path. Thus, it is suitable to detect faults in a large structure as well as recognize the different kinds of faults. In comparison with other traditional NDT techniques, Guided Lamb wave-based fault detection using piezoelectric lead zirconate titanate (PZT) elements, which is one of the most popular ultrasonic techniques, is considered cost-effective for use in applications. Unlike other detection methods, AE method is used to detect the transient elastic waves caused by crack formation. Therefore, it is more appropriate to investigate the dynamic behaviour of structures. In addition, this method is not employed to detect structural faults after the formation of faults. While all the structural crack detecting methods rely on waves propagating in the structures, as indicated in table 4, the kurtosis beamforming method relies on the acoustic waves propagating in the air, which is categorized as an acoustic imaging technique. The main advantage of this technique is that it eliminates the necessity to attach the sensors to the structure, making it suitable for a wide range of SNRs.

Table 3.2

Kurtosis beamforming method vs other condition monitoring approaches.

Condition monitoring approaches	Vibration technique	Ultrasonic technique	Magnetic methods	Acoustic emission	Kurtosis beamforming method
Actuators	Nil	Piezoelectric lead zirconate titanate elements	Ultrasonic control unit	Nil	Nil
Sensors	Accelerometers	Piezoelectric sensors	Electromagnetic acoustic transducer probes	Acoustic emission sensors	Microphones
Signal	Vibration signal	Lamb wave	Rayleigh wave	Transient elastic wave	Acoustic signal
Non-destructive testing	Yes	Yes	Yes	Yes	Yes
Estimating dynamic characteristics of faults	No	No	No	Yes	No
Requiring contact between sensors and structure	Yes	Yes	Yes	Yes	No

3.4 Influence of signal-to-noise ratio and background noise

When the background noise is added in the sound field, it is difficult for the beamformer evaluated by RMS and peak value to identify the location of pristine wheel and the wheel-flat. It is noteworthy that in a real scenario or in the outdoor environment, the background noise may vary and thus may influence the accuracy of the fault identification of the railway wheel when using the kurtosis value. Under such circumstance the impulsive signals generated by faults might be totally merged in rolling noise and background noise. Therefore, the SPL of the loudspeaker was varied such that different SNRs were acquired by the array of microphones for analysis. Table 3.3 shows the result of the kurtosis value for different types of faults under different SNR ($SNR = Power_{fault} / Power_{background\ noise}$). The measurements were repeated 20 times. For each type of fault, the kurtosis values become smaller when the SNR is decreased. It is close to 3 when the SNR is too low, i.e., approximately 0.2 to 0.4 for the dent and squat, respectively. In this regard, the wheel may be misdiagnosed as a pristine structure without fault.

Table 3.3

Different SNRs applied to three types of faults signals and their kurtosis values.

Type of signal	SNR	Kurtosis value	Standard deviation
Dent (depth=2 mm)	0.6409	3.5003	0.0285

	0.4083	3.0380	0.0153
	0.1390	2.9848	0.0156
Squat	0.9236	5.9115	0.1198
	0.5884	4.3933	0.0577
	0.2003	3.1068	0.0165
Wheel-flat (depth=1 mm)	1.0934	30.9272	1.8299
	0.6965	11.1754	0.4175
	0.2371	5.4277	0.2417

Further investigations were conducted by comparing the localisation performance of the time-domain beamforming using the peak value, RMS, and kurtosis estimator under different SNRs. In this study, one loudspeaker generating different powers of random noise, located at (0.3 m, 0.7 m), and one roller test rig at (0.7 m, 0.7 m) were used. The SPL of background noise received by one of the microphones ranged from 35 dB to 98 dB when the roller test rig was switched off. The corresponding experimental set up is shown in the Figure 3.5 below.

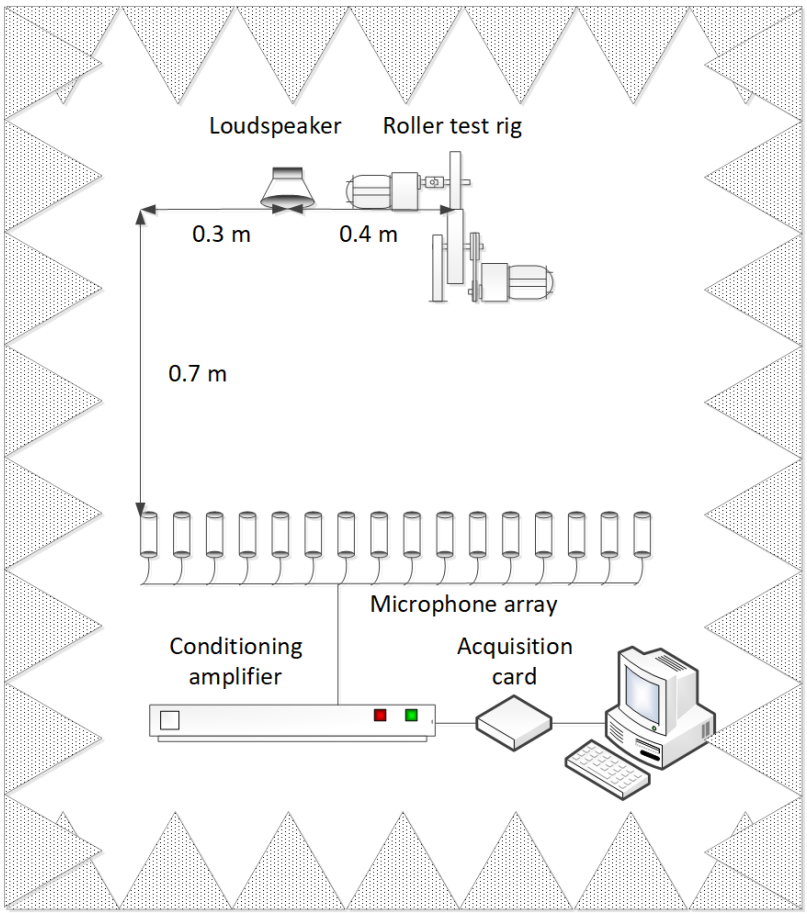

Figure 3.5 Experimental setup.

Figure 3.6 shows the beamforming map for the localisation of the wheel with the fault of wheel-flat under different SNRs. The first, second, and third column of Figure 3.6 show the time-domain beamformer evaluated by the peak value, RMS, and kurtosis value, respectively. The first, second, third, fourth, fifth, and sixth row of Figure 3.6 represent the beamforming map under the condition of background noise of approximately 84–98 dB, 72–83 dB, 66–71 dB, 60–65 dB, 55–59 dB, and 35–54 dB, respectively. In the experiments, the wheel-flat signal remained at 49 dB, and the background noise in the anechoic chamber was 26 dB. When the background noise is approximately 84–98 dB, the location of the speaker

can only be observed based on the peak value in Figure 3.6(1a) and the RMS in Figure 3.6(1b). Additionally, the location of the wheel fault was totally merged even in the kurtosis beamformer map in Figure 3.6(1c). Similar results of the beamformer output of peak and RMS values are shown in Figure 3.6(2a) and Figure 3.6(2b), respectively, when the background noise is approximately 72–83 dB. However, the location of the fault of wheel-flat can be approximately identified and localised using the kurtosis beamformer map, as shown in Figure 3.6(2c). When the background noise is reduced to approximately 66–71 dB, both the location of the fault of wheel-flat and loudspeaker can be revealed using the RMS in Figure 3.6(3b); however, the loudspeaker location may be misdiagnosed as the fault. Meanwhile, the fault location can be recognised clearly using the kurtosis beamformer map as shown in Figure 3.6(3c). When the background noise is further reduced to approximately 60–65 dB, the fault location can be localised by both beamformers of RMS and kurtosis, as shown in Figure 3.6(4b) and (4c), respectively. Moreover, the kurtosis beamformer performed better than the others owing to a lower SLL. When the background noise is reduced to 55–59 dB, the location of wheel-flat can be obtained by using the RMS and kurtosis. When the background noise is low, approximately 35–54 dB, such that white noise signal is buried in the signal of the wheel-flat, all the beamforming maps presented similar localisation results. It is noteworthy that the value of the kurtosis beamformer at the location of the wheel-flat gradually increases with the SNR. This is consistent with the result of Table 3.3. The kurtosis value has a positive correlation with the

severity of faults and SNR.

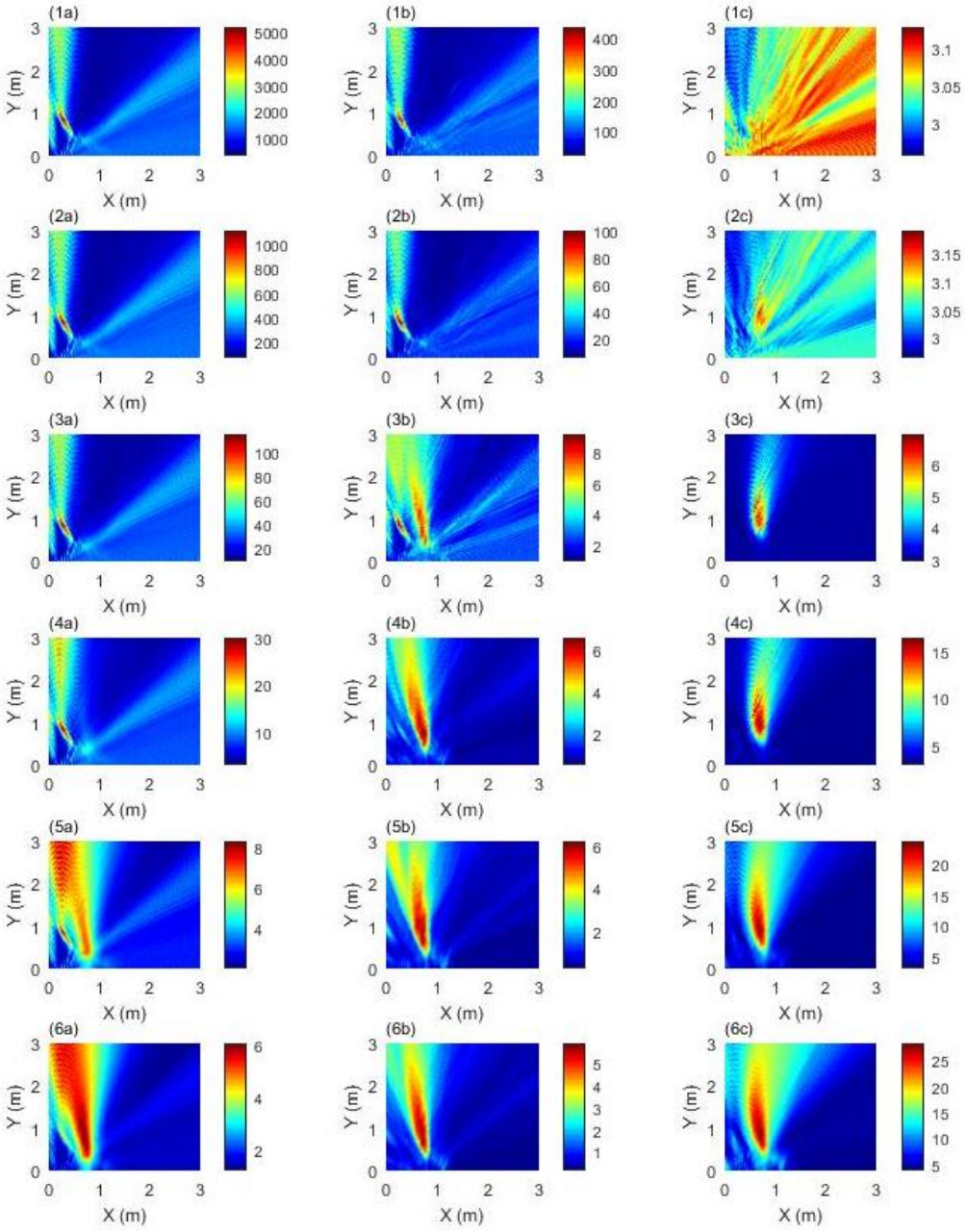

Figure 3.6 Fault detection and localisation results using beamforming power, peak value, and kurtosis under different SNRs. The first, second, and third columns show the time-domain beamformer evaluated by peak, RMS, and kurtosis values, respectively. The first, second, third, fourth, fifth, and sixth row represent the beamforming maps under the background noise of

approximately 84–98 dB, 72–83 dB, 66–71 dB, 60–65 dB, 55–59 dB, and 35–54 dB, respectively.

3.5 Influence of the duration of data acquisition on kurtosis value

The rotating wheel on the rail generates an impulsive signal comprising multiples impulses due to the multiple impacts when the train traverses on the rail. This raises a question: up to how many impulses can be contained for the detection? We assume that the impact noise generated is a Gaussian impulsive signal, such that

$$s(t) = -2\pi^2 f^2 (t - 0.01n) e^{-2\pi^2 f^2 (t-0.01n)^2} \tag{3.1}$$

where f is the centre frequency, and n is a decay factor. In this case, f was set to be 100, while n was changed from 1 to 10. Figure 3.7 shows the kurtosis value as a function of the number of impulses per second. The curve of the Gaussian impulsive signal has a similar trend with that of the measured data of the wheel-flat. When three impulses per second are adopted for the analysis, the kurtosis value can reach the maximum value of approximately 12. For the measured data of squat and dent, the kurtosis value can attain the maximum when the number of impulses per second is approximately 4. Generally, the kurtosis value could reach 6 or even higher when 1 to 10 impulses per second are used for the analysis. This indicates that when the duration of data acquisition for analysis contains at least

one impulse signal, it would be accurate enough to identify the fault according to the kurtosis beamformer. However, if the number of impulses per second is high, the kurtosis value becomes low and may influence the accuracy of the fault localisation. This method may also provide a useful tool for the routine maintenance of some low speed rotating machine.

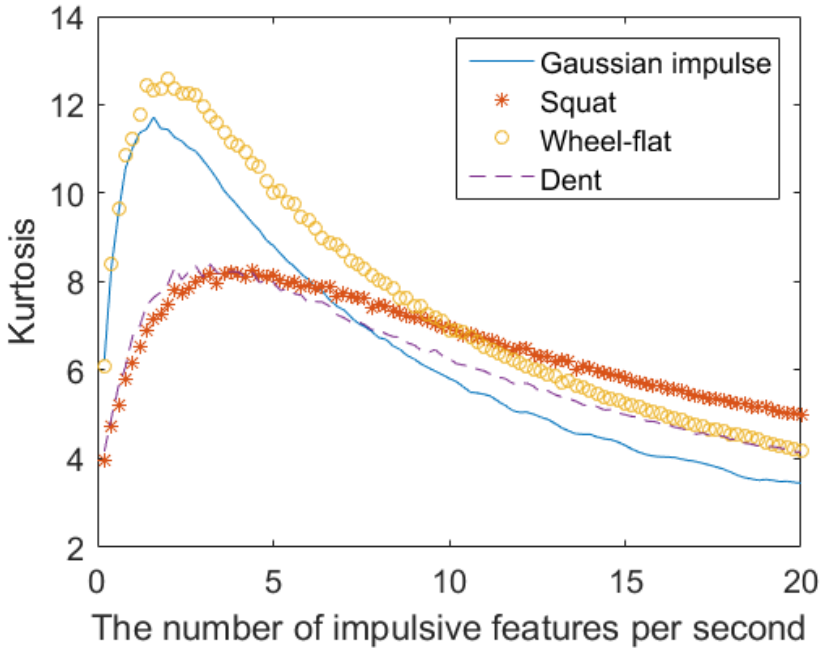

Figure 3.7 Kurtosis values vs. the number of impulsive features per second in different signals.

3.6 Chapter summary

In this chapter the proposed kurtosis beamformer is further investigated by theoretical and experimental study. Firstly, different types of wheel faults such as dent, squat, and wheel-flat can be identified according to the kurtosis value.

Compared with the beamforming output evaluated by RMS and peak value, the kurtosis beamformer has a lower SLL and its ability to extract the impulsiveness emerging from the background noise is much stronger. Typically, the beamforming power can yield accurate positions of the sound sources in a field of multiple sound sources based on the acoustical power. When the background noise is high, the kurtosis outperforms the peak value and RMS to extract the feature of impulsive signals. In addition, the kurtosis value and its accuracy depended on the duration and number of impulses of the acquired signal for data analysis.

The influence of SNR on the kurtosis value for the signal of different types of faults has been investigated as well. The signals of significant faults with high SNRs tend to result in a large kurtosis value. Random noise or other interference distributions typically have a lower kurtosis value. However, the proposed method performs well when the fault is relatively small, where a low SPL or SNR is generated. Herein, the performance of the time-domain beamformer using three different estimators such as the peak, RMS, and kurtosis values under different SNR conditions has been studied. The kurtosis beamformer was found to be suitable for a wide range of SNRs, even in cases where the impulsive feature in the signal is completely indistinguishable using the traditional beamforming method from the background noise.

CHAPTER 4

Ground impedance estimation

4.1 Introduction

The beamforming map of the fault proposed in Chapter 2 and 3 is based on the free field assumption. In reality, ground with different material properties exists underneath the rail; ground reflections should not, therefore, be ignored. For the presence of such ground, Tam et al. proposed a hybrid method combining the Levenberg–Marquardt (LM) and MUSIC methods to estimate a time-harmonic point sound source location and the ground impedance simultaneously (K. Li, Attenborough, & Heap, 1991; Tam, Lau, & Tang, 2016). The MUSIC method is a subspace-based approach of beamforming (Kim & Choi, 2013; Schmidt, 1986) that makes use of the eigen decomposition of a correlation matrix of all the microphone signals in the frequency domain to separate the signal and noise subspaces. Compared with the traditional DAS and the MVDR methods (Cigada et al., 2007; Kim & Choi, 2013; J. Li et al., 2003), MUSIC has a higher spatial resolution and lesser sidelobes to achieve a better representation of sound source locations. It has also been adopted in broadband sound source range and bearing

estimation (Jeffers, Bell, & Van Trees, 2002). By summing the narrowband MUSIC responses for each frequency bin, the broadband MUSIC (B-MUSIC) response over a frequency range could be implemented to improve the accuracy of localising multiple sound sources in real noisy environments (Ishi, Chatot, Ishiguro, & Hagita, 2009). In order to accurately detect the position of sound sources and ground impedance, the LM method is adopted, which is a modified optimisation process of the Gauss–Newton method by introducing a non-negative damping factor to achieve a reduction in residual vibrations (Hartley, 1961; Levenberg, 1944; Marquardt, 1963). In the work of Tam et al., the Jacobian matrix in the LM optimisation process is performed numerically by the backward finite difference method (FDM). Compared to the Crank Nicolson (CN) method (Sweilam, Khader, & Mahdy, 2012), the error produced in the iteration process of backward FDM is usually larger. Nevertheless, with the initial locations from MUSIC, the LM method significantly improves the accuracy of the source locations, and meanwhile provides flexibility to the estimation of ground impedance (Tam et al., 2016).

Aiming at locating and identifying faults of an uneven surface of a wheel in the wheel/rail system along with the ground effect, the function of the time-domain kurtosis beamformer is extended to include the fault visualisation and ground impedance estimation simultaneously. To deal with these at the same time, the initial estimation of the fault location is found by using our proposed broadband weighted multiple signal classification (BW-MUSIC) method instead of using the

conventional B-MUSIC method in this chapter. Moreover, the impedance of the reflecting ground surface is found using our proposed modified LM method, which is slightly more efficient than the LM method adopted by the team of Tam et al. Subsequently, the location of a fault on a wheel with an impact noise feature can be accurately determined by the time-domain kurtosis beamformer.

4.2 Theoretical formulation

The research findings in Section 2.3.1 indicates that the wheel faults can hardly be identified from pristine wheels using the traditional frequency-domain method. Considering the ground impedance is a function of frequency, new localization approach in broadband frequency-domain should be studied in this research. Through the exploration of the traditional beamforming methods including DAS, LCMV and MUSIC method, a so-called BW-MUSIC method is proposed to detect the broadband signals. To start with, the methodology of traditional DAS, LCMV and MUSIC method will be first introduced in this section, while the performance of these three beamformer will be compared. Then the sound wave propagation model with ground impedance will be introduced. Based on which, the theoretical formulation of the BW-MUSIC and LM-CN method will be proposed in the following sections.

4.2.1 Frequency-domain beamformer

4.2.1.1 DAS beamformer

The example used in this section is simplified by assuming the sound as a pure tone. Assuming an acoustic signal is measured by a linear array of *M* microphones by adopting the plane wave model which is introduced in Section 2.2.1, while the DOA of the plane wave source is θ_0, the sound frequency is ω and the distance between two neighboring microphones is *d*. The measured complex pressure field can be expressed in vector form as:

$$\mathbf{p}(\omega) = [\, p_1(\omega) \quad p_2(\omega) \quad \cdots \quad p_M(\omega) \,]^T \tag{4.1}$$

The *m*th element of $\mathbf{p}(\omega)$ is the complex pressure signal of the source at the *m*th microphone which is given by:

$$p_M(\omega) = q(\omega) e^{-i\omega(m-1)(d/c)\sin\theta_0} \tag{4.2}$$

where $q(\omega)$ is the amplitude of the source signal and it is usually called the source excitation signal. The transfer function between the measurement signal of the *m*th microphone and the source excitation *q* is denoted by $h_m(\theta_0, \omega)$:

$$h_m(\theta_0, \omega) = e^{-i\omega(m-1)(d/c)\sin\theta_0} \tag{4.3}$$

In plane wave model assumption, the DOA are totally equal at each microphone, and once the DOA is estimated, the sound source location is determined. Thus, to extract θ_0, a so-called steering vector (also called weighting function) $\mathbf{w}(\theta, \omega)$ is adopted:

$$\mathbf{w}(\theta,\omega) = [w_1(\theta,\omega) \quad w_2(\theta,\omega) \quad \cdots \quad w_M(\theta,\omega)]^T \tag{4.4}$$

in which the *m*th element of the scan vector for a plane wave source is given by:

$$w_M(\theta,\omega) = \frac{1}{M} e^{-i\omega(m-1)(d/c)\sin\theta} \tag{4.5}$$

Using the steering vector and the measured sound signal $\mathbf{p}(\omega)$, the near-field frequency-domain DAS beamformer output can be defined as:

$$\begin{aligned} b(\theta,\omega) &= \mathbf{w}(\theta,\omega)^H \mathbf{p}(\omega) \\ &= \frac{q(\omega)}{M} \sum_{m=1}^{M} e^{-i\omega(m-1)(d/c)(\sin\theta - \sin\theta_0)} \end{aligned} \tag{4.6}$$

where the superscript *H* is the Hermitian transpose (complex-conjugate transpose) of a matrix. The expected value of the squared beamformer output is called the beamforming power $\beta(\theta,\omega)$. The beamforming power is a useful measure for visualizing the sound power distribution at the assumed source locations, which is defined as:

$$\begin{aligned} \beta(\theta,\omega) &= E[|b(\theta,\omega)|^2] \\ &= \mathbf{w}(\theta,\omega)^H \mathbf{R}(\omega)\mathbf{w}(\theta,\omega) \end{aligned} \tag{4.7}$$

where

$$\mathbf{R}(\omega) = \mathrm{E}[\mathrm{p}(\omega)\mathrm{p}(\omega)^H] \tag{4.8}$$

is the correlation matrix of the measured signal. Each element of it represents the correlation of two microphone signals in frequency domain.

4.2.1.2 LCMV beamformer

The development of various beamforming methods is based on the

development of the steering vector design. When there are multiple sources in the sound field, the beamforming power at a certain steering angle becomes the summation of the contribution of the source in the looking direction and the contributions from the sources in other directions. The LCMV beamformer looks for the source location by minimize the undesirable contributions from the sources in other directions. It designs the steering vector in such way so that the specified amplitude output of the beamformer is normalized in certain looking direction. The criteria for designing this steering vector is based on the assumption that the total beamforming power at the looking direction will be minimized if all the contributions from the sources in other directions are rejected by the designed weighting function. Thus, the problem becomes an optimization problem subject to equality constraints. Typically, if the amplitude output is constrained to be 1, the beamformer output response will not be distorted in the looking direction and the beamformer is hence named the MVDR beamformer.

This optimization problem can be solved by using Lagrange multiplier method: to minimize the equation 4.7

$$\beta(\theta, \omega) = \mathbf{w}(\theta, \omega)^H \mathbf{R}(\omega)\mathbf{w}(\theta, \omega) \tag{4.7}$$

which subject to the equation

$$b(\theta) = \mathbf{w}(\theta)^H \mathbf{h}(\theta) \tag{4.9}$$

The problem is equivalent to minimize the equation

$$J(\mathbf{w}, \mu) = \mathbf{w}^H \mathbf{R}\mathbf{w} + \mu(\mathbf{w}^H \mathbf{h} - 1) \tag{4.10}$$

in which μ is the Lagrange multiplier, and $\mathbf{h}$ is the transfer function of the source

signal to the measurement signal. Similar to the equation 4.4 and 4.5, in the far field assumption, **h** can be expressed as:

$$\mathbf{h}(\theta,\omega) = [h_1(\theta,\omega) \quad h_2(\theta,\omega) \quad \cdots \quad h_M(\theta,\omega)]^T \tag{4.11}$$

in which

$$h_M(\theta,\omega) = \frac{1}{M} e^{-i\omega(m-1)(d/c)\sin\theta} \tag{4.12}$$

By finding the zero-derivative point of *J* respect to **w** and μ, we have:

$$\frac{\partial J}{\partial \mathbf{w}^H} = \mathbf{R}\mathbf{w} + \mu\mathbf{h} = 0 \Rightarrow \mathbf{w} = \mu\mathbf{R}^{-1}\mathbf{h} \tag{4.13}$$

and

$$\frac{\partial J}{\partial \mu} = \mathbf{w}^H\mathbf{h} - 1 = 0 \Rightarrow \mathbf{w}^H\mathbf{h} = 1 \tag{4.14}$$

Therefore, the solution for **w** is given by:

$$\mathbf{w}(\theta) = \frac{\mathbf{R}^{-1}\mathbf{h}(\theta)}{\mathbf{h}(\theta)^H\mathbf{R}^{-1}\mathbf{h}(\theta)} \tag{4.15}$$

The MVDR beamforming power which can be obtained by substituting the equation (4.15) into equation (4.7):

$$\beta_{MVDR}(\theta) = \frac{1}{\mathbf{h}(\theta)^H\mathbf{R}^{-1}\mathbf{h}(\theta)} \tag{4.16}$$

4.2.1.3 MUSIC beamformer

MUSIC is a popular subspace-based approach of beamforming in frequency domain for multiple sound sources, which makes the use of the eigen decomposition of correlation matrix $\mathbf{R}$ of measured sound signal to extract the signal and noise subspaces. Since the eigen vectors of noise subspace $\mathbf{U}_n$ is

orthogonal to the basis vectors of the signal subspace $\mathbf{U}_{sn}$, the MUSIC beamforming output can be calculated by the inverse of a scan vector $\mathbf{w}(\omega)$ belongs to the signal subspace multiplied by the correlation matrix of the noise subspace. By adopting this method, a higher spatial resolution and lesser sidelobes in sound maps can be achieved.

To begin with, recall the correlation matrix $\mathbf{R}$:

$$\mathbf{R}(\omega)=\mathrm{E}[\mathrm{p}(\omega)\mathrm{p}(\omega)^{H}] \tag{4.17}$$

The correlation matrix can be expressed as an eigen decomposition form, that is:

$$\mathbf{R} = \mathbf{U}\mathbf{D}\mathbf{U}^{H} \tag{4.18}$$

Since the columns of $\mathbf{U}$ are orthogonal, the correlation matrix can be separated into two parts:

$$\begin{aligned}\mathbf{R} &= \mathbf{U}\mathbf{D}\mathbf{U}^{H} \\ &= \mathbf{U}_{sn}\mathbf{D}_{sn}\mathbf{U}_{sn}^{H} + \mathbf{U}_{n}\mathbf{D}_{n}\mathbf{U}_{n}^{H}\end{aligned} \tag{4.19}$$

where $\mathbf{U}_{sn}$ and $\mathbf{D}_{sn}$ are the eigenvectors and eigenvalues corresponding to the κ largest eigenvalues of $\mathbf{R}$, and $\mathbf{U}_{n}$ and $\mathbf{D}_{n}$ are those defined from the remaining eigenvalues from $\kappa+1$ to m. Since $\mathbf{U}_{n}$ is orthogonal to the basis vectors of the signal subspace, the beamforming power calculated from the correlation matrix consisting of these eigenvectors

$$\beta_{n}(\theta) = \mathbf{w}(\theta)^{H}\mathbf{U}_{n}\mathbf{U}_{n}^{H}\mathbf{w}(\theta) \tag{4.20}$$

will be minimal for a scan vector $\mathbf{w}(\theta)$ belonging to the signal subspace. The size of the correlation matrix $\mathbf{R}$, $\mathbf{U}$ and $\mathbf{D}$ matrix are M*M, but the numbers in $\mathbf{D}$ are all zero except the diagonal line. (M is the number of microphone). The size of $\mathbf{U}_{n}$ matrix is M*(M-the number of sound sources), and for $\mathbf{U}_{sn}$ matrix

is M*(the number of sound sources). The inverse of the beamforming power indicates the source location has a maximum value when the scan vector $\mathbf{w}(\theta)$ belongs to the signal subspace. And the MUSIC beamforming output can be written as:

$$\beta_{MUSIC}(\theta) = \frac{1}{\mathbf{w}(\theta)^H \mathbf{U}_n \mathbf{U}_n^H \mathbf{w}(\theta)} \tag{4.21}$$

4.2.1.4 Localization simulation

In order to show the basic principle of the beamforming techniques, the simplest case will be introduced below in which only a 1D evenly distributed linear array is adopted and several pure tone sound sources are assumed far away enough so that the wavefronts are considered as a plane wave. The performance of the algorithms introduced above is investigated theoretically with a virtual 1D measurement procedure. An array of 20 microphones is adopted in the following example. The frequency of the source signals is assumed to be 1200Hz, and the spacing of the microphones is set to be 0.16m. The case was designed including three signal sources with the DOA are 30, 60, and 90 degree, respectively, and the interference noise whose SNR = 40. Beamforming programs were coded by MATLAB. Figure 4.1 shows the results of the comparison of DAS, MUSIC and LCMV method.

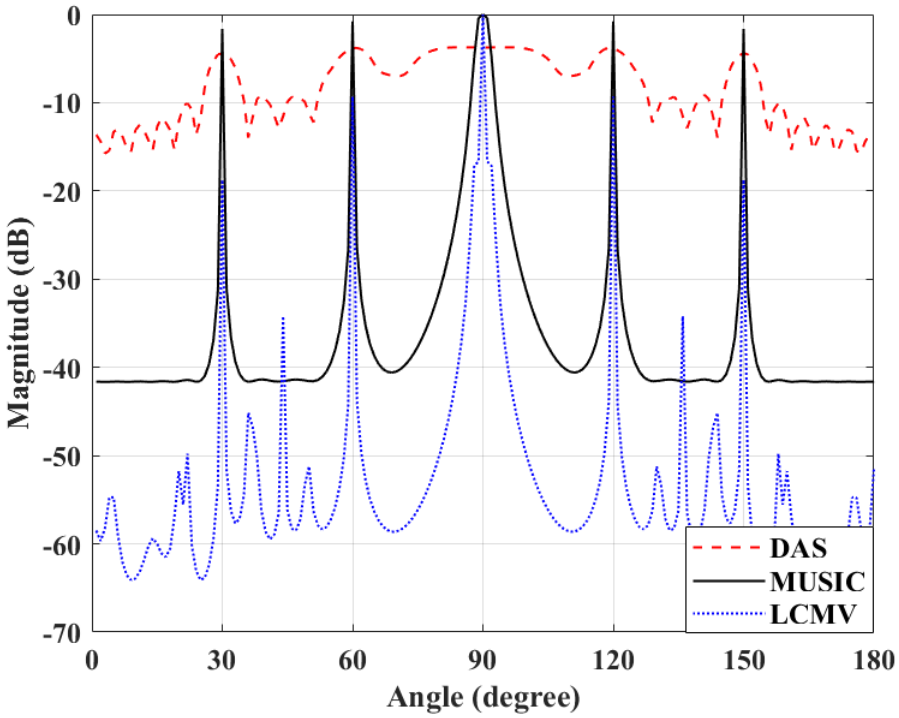

Figure 4.1 Comparison of DAS, MUSIC and LCMV method.

In this case, the DAS beamformer failed to distinguish the three sources, while the correct localization result is given by the MUSIC and LCMV method, the DOA were very accurate and the three mainlobes are very sharp. The DAS beamformer is the most basic beamformer and gives the worst localization result since it doesn't adopt any feature of the signal except the time delay. The other two types of beamformers: MUSIC and LCMV method have much more better results with sharp mainlobes, and in particular no sidelobes can be observed in the curve of MUSIC method when the interference noise is added. Unlike the traditional DAS method, they both show good capabilities to localize multiple sources. However, apart from the sidelobe resulting from interference noise, the performance of the LCMV beamformer can also degrade significantly when there

are multiple incoherent sound sources in the measurement channels. When one source energy is much weaker than the others, the weaker sound source may merge in the mainlobe of the stronger one. In consideration of these two constraints, in frequency-domain, the MUSIC method is most recommended in the following research of this thesis.

4.2.2 Sound wave propagation model influenced by ground effect

Figure 4.2 shows a sound source propagation model over a flat ground surface with the normal impedance *Z*. Assuming that p_m is the measured sound pressure, $r_m(x_m, y_m) = \sqrt{(x-x_m)^2 + (y-y_m)^2}$ is the distance between the sound source and the m^{th} receiver microphone, and m is the index of each microphone. $r_i = \sqrt{r_m^2 + 4h_m h_s}$ is the distance between the image source and the m^{th} microphone. The total complex sound pressure at the m^{th} microphone due to the sound source and image source can be expressed as:

$$p_m(r_m) = \frac{\exp(i\omega r_m / c)}{r_m} + Q\frac{\exp(i\omega r_i / c)}{r_i} \tag{4.22}$$

in which c is the speed of sound, and Q is the complex spherical wave reflection coefficient and can be given by:

$$Q = R_p + (1-R_p)F(w) \tag{4.23}$$

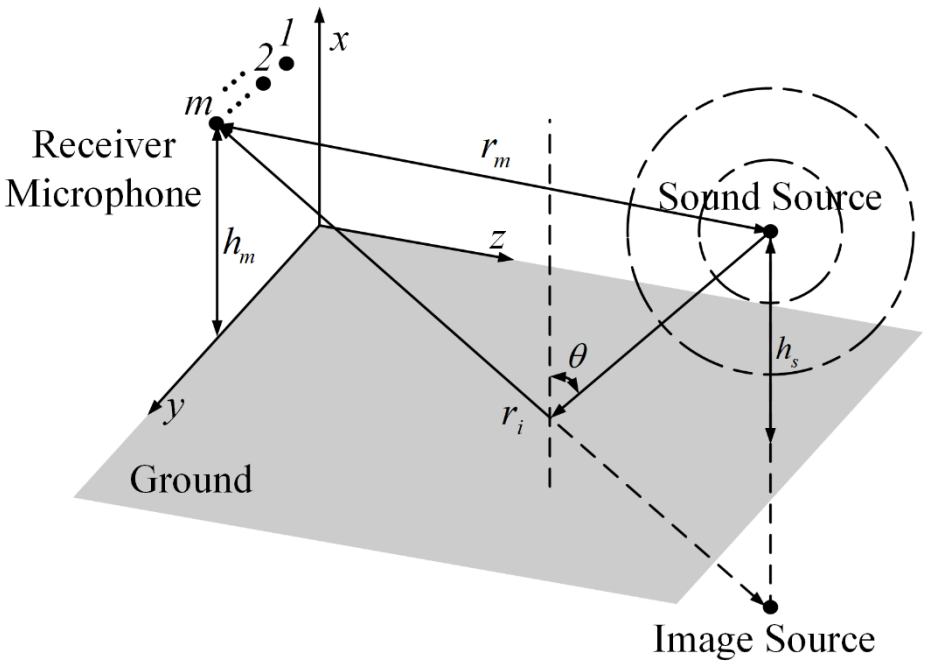

Figure 4.2 Sound source propagation model over ground surface.

where R_p is the plane wave reflection coefficient and $F(w)$ is the boundary loss factor. R_p and $F(w)$ can be calculated by the equations below:

$$R_p = (Z\cos\theta - 1)/(Z\cos\theta + 1) \tag{4.24}$$

$$F(w) = 1 + i\sqrt{\pi}we^{-w^2}\,\mathrm{erfc}(-iw) \tag{4.25}$$

$$w^2 = (i\omega r_i/2c)[(1/Z) + \cos\theta]^2, \tag{4.26}$$

in which θ is the incidence angle, $\mathrm{erfc}(\cdot)$ represents the complementary error function and *Z* is the normal impedance of the ground surface:

$$\begin{aligned} Z &= Z_r + iZ_i \\ &= 0.436\sqrt{\sigma_e/f} + i[0.436\sqrt{\sigma_e/f} + 19.48(\alpha_e/f)] \end{aligned} \tag{4.27}$$

In this study, the effective rate of change of porosity with depth α_e is assumed to be $150\,m^{-1}$, and the effective flow resistivity at the ground surface σ_e will be estimated by the LM method so that the complex spherical wave reflection

coefficient Q can be estimated eventually.

4.2.3 Initial estimation of source location by BW-MUSIC

The MUSIC method is mainly applied in the frequency domain. It makes use of the eigen decomposition of the correlation matrix $\mathbf{R}$ of the measured sound signal to extract the signal and noise subspaces. Re-call the MUSIC beamforming output in far-field assumption:

$$\beta_{MUSIC}(\theta) = \frac{1}{\mathbf{w}(\theta)^H \mathbf{U}_n \mathbf{U}_n^H \mathbf{w}(\theta)} \tag{4.21}$$

The MUSIC beamforming output in near-field assumption can be written as:

$$\beta_{MUSIC}(r_m) = \frac{1}{\mathbf{w}(r_m)^H \mathbf{U}_n \mathbf{U}_n^H \mathbf{w}(r_m)} \tag{4.22}$$

By computing the MUSIC beamforming output $\beta_{MUSIC}(r_m, f)$ for each frequency bin $(1-N)$, the B-MUSIC output can be expressed by averaging these narrowband outputs over a broadband frequency range:

$$\beta_{BM}(r_m) = \frac{1}{N} \sum_{f=f_0}^{f_N} \beta_{MUSIC}(r_m, f) \tag{4.23}$$

However, as we know, the selection of the computed frequency during narrowband beamforming calculation can be critical. That is because inexact frequency selection would lead to an incorrect localisation result. Considering the different contributions of each frequency in the spectrum, the straightforward summation of the whole frequency range in equation (4.23) could also lead to an incorrect localisation result. We believe that the estimation of the location of a broadband

signal should be weighted by the multiple Fourier transform (FT) results $F(f)$ themselves, so that the interference of the non-dominating frequency band can be eliminated during computation of the beamforming. By such means, The BW-MUSIC output can be given by:

$$\beta_{WBM}(r_m) = \frac{1}{N}\sum_{f=f_0}^{f_N} F(f)\beta_{MUSIC}(f, r_m) \tag{4.24}$$

This method may be considered a compromise that meets both the broadband and narrowband requirements. In one respect, broadband signal features are considered; on the other hand, the advantage of accurate selection of the dominating frequency during computation of the narrowband beamforming may be retained.

4.2.4 Further estimation of source location and ground impedance by the LM and Crank Nicolson methods

In this section, the LM optimisation process is introduced to estimate the ground impedance and simultaneously to revise the source location further. An error function of the sound source location (x, y) and the effective flow resistivity at the ground surface σ_e in vector form is defined as:

$$\mathbf{e}(x, y, \sigma_e, \omega) = [\mathbf{S}(x_0, y_0, \sigma_{e_0}, \omega) - \hat{\mathbf{S}}(x, y, \sigma_e, \omega)] \tag{4.25}$$

in which $\mathbf{S}(x_0, y_0, \sigma_{e_0}, \omega)$ is the initial reference signal vector calculated by beamforming output while $\hat{\mathbf{S}}(x, y, \sigma_e, \omega)$ is the signal vector to be estimated. The objective of the LM optimisation process is to minimise the error function $\mathbf{e}(x, y, \sigma_e, \omega)$. To utilise the LM optimisation process, the Jacobian matrix is

introduced and can be calculated by a numerical method:

$$\mathbf{J}(\omega)=[\frac{\partial \mathbf{e}(x,y,\sigma_e,\omega)}{\partial x}\quad \frac{\partial \mathbf{e}(x,y,\sigma_e,\omega)}{\partial y}\quad \frac{\partial \mathbf{e}(x,y,\sigma_e,\omega)}{\partial \sigma_e}], \tag{4.26}$$

in which the partial differential term $\partial \mathbf{e}(\omega)$ is calculated by the backward FDM in former research:

$$\frac{\partial \mathbf{e}(\omega)}{\partial x}=\frac{\mathbf{e}(x)-\mathbf{e}(x-\Delta x)}{\Delta x} \tag{4.27}$$

which will be replaced by the Crank Nicolson method:

$$\frac{\partial \mathbf{e}(\omega)}{\partial x}=\frac{\mathbf{e}(x+\Delta x)-\mathbf{e}(x-\Delta x)}{2\Delta x} \tag{4.28}$$

in this study, which yields a more accurate approximation. The comparison of these two FDMs is presented in Section 4.41. The variable intervals in equation 4.28 are set to $\Delta x=\Delta y=10^{-13}$ m and $\Delta\sigma_e$=100 MKS rayls/m . The $(n+1)^{\text{th}}$ iteration result ξ_{n+1} of the LM optimisation process is:

$$\xi_{n+1}=\xi_n-\{\mathbf{J}(\omega)^T\mathbf{J}(\omega)+\lambda\ \mathrm{diag}[\mathbf{J}(\omega)^T\mathbf{J}(\omega)]\}^{-1}\mathbf{J}(\omega)^T\mathbf{e}(\omega), \tag{4.29}$$

in which λ is a positive scalar regularisation parameter. This parameter is introduced to overcome the difficulty when $\mathbf{J}(\omega)^T\mathbf{e}(\omega)$ is singular or nearly singular. When $\lambda=0$ the optimisation process becomes the well-known Gauss-Newton optimisation method. During the application, the strategy is to try a as small as possible lambda value as a start, for example, 0.0001. If the rate of convergence is too slow, or the error function becomes bigger, then we should try a bigger lambda. And eventually we will find an appropriate lambda value for a specified convergence procedure. It also could be a variable instead of a constant number during every iteration step to obtain an optimized convergence procedure. Y. He et al. presents a corrected LM algorithm to adjust the value of λ so that the

whole process is more efficient and robust. In this study, λ is set at 0.01 to meet the stability demand of estimation.

4.3 Simulation

4.3.1 LM estimation process by using the backward finite difference and CN methods

Numerical simulations are performed by MATLAB to compare the performance of the LM method by adopting the backward finite difference and CN methods during the calculation of the Jacobian matrix. The sound source location is assumed at (0.5 m, 1 m), while the effective flow resistivity is assumed to be 200,000 MKS rayls/m. Once the effective flow resistivity is estimated, the value of the normal impedance of the ground surface can be easily derived from equation (4.27). The frequency of the sound source is set to be 1,000 Hz throughout the analysis. To conduct the LM optimisation estimation process, an initial input localisation from beamforming is assumed at (0.55 m, 1.05 m), and the preliminary estimation of the effective flow resistivity is assumed to be 220,000 MKS rayls/m, which is typical for sandy ground. The details of LM and LM–CN estimation theories are introduced in Section 4.2.4. The comparison of the LM method is shown in Figure 4.3 as a dashed line for backward finite difference in and a solid line for LM–CN. The iterations are computed up to 10,000 times in both processes

so that the estimated parameters converge on the actual values as far as possible. Figure 4.3(a) and (b) show the estimated coordinates of the sound source, and Figure 4.3(c) shows the estimated effective flow resistivity. Clearly by replacing the backward FDM with the CN method, the rate of convergence among all three sets is improved. The initial values along the solid lines move towards the actual values more quickly than the dashed lines. Furthermore, the convergence values by the LM–CN method are closer to the actual values.

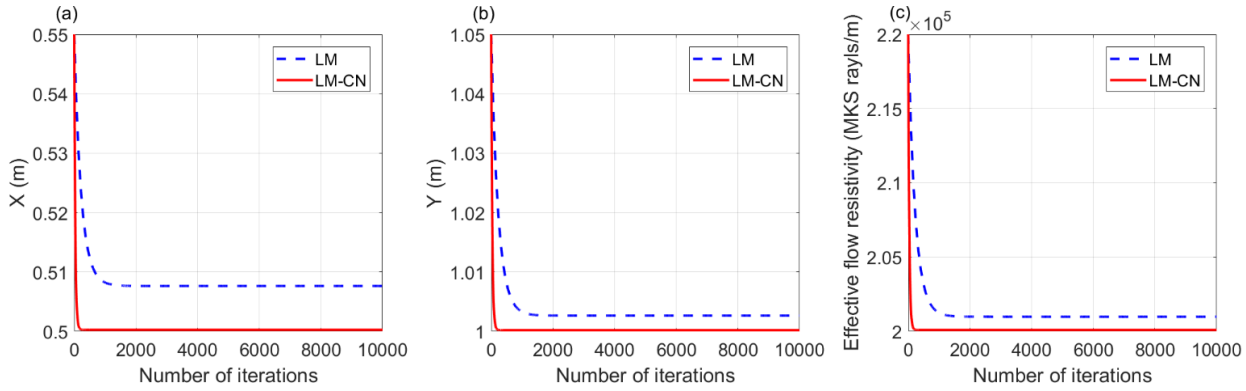

Figure 4.3 Comparison of simulation results of the LM method using the backward finite difference and LM–CN methods.

4.3.2 Initial localisation results simulation

Localisation simulations are performed by the finite element method (FEM) software COMSOL to investigate the performance of the proposed BW-MUSIC method against the traditional DAS and MUSIC method, under the influence of ground effect. The transient pressure acoustics model was adopted in the

simulations and a Gaussian pulse was set at the point source to imitate an impulsive signal. The scalar wave equation of the transient pressure acoustics model is:

$$\frac{1}{\rho c^2}\frac{\partial p_t}{\partial t^2}+\nabla\cdot\left[-\frac{1}{\rho}\left(\nabla p_t-\mathbf{q}_d\right)\right]=Q_m \tag{4.30}$$

The wave equation of the Gaussian pulse source is:

$$\frac{1}{\rho c^2}\frac{\partial p_t}{\partial t^2}+\nabla\cdot\left[-\frac{1}{\rho}\left(\nabla p_t-\mathbf{q}_d\right)\right]=\frac{4\pi}{\rho c}S\delta(\mathbf{x}-\mathbf{x}_0), \tag{4.31}$$

in which p_t is the total acoustic pressure, ρ is the fluid density, $\mathbf{q}_d$ is the dipole domain source, Q_m is the monopole domain source, and *S* is the source strength:

$$S=-A_m\rho\frac{\pi}{2}f_0^2(t-t_p)e^{-\pi^2 f_0^2(t-t_p)^2}, \tag{4.32}$$

where A_m is the value of the pulse amplitude, f_0 is the frequency bandwidth, and t_p is the pulse peak time. To simulate the ground impedance, an impedance boundary condition under the sound area was set while the other three sides of the sound area were surrounded by a perfectly matched layer (PML). The impedance boundary condition is the following:

$$-\mathbf{n}\cdot\left[-\frac{1}{\rho_c}\left(\nabla p-\mathbf{q}_d\right)\right]=\frac{1}{Z_a}\frac{\partial p_t}{\partial t}\quad, \tag{4.33}$$

in which the acoustic input impedance Z_a is related to the acoustic impedance Z_{ac} and the mechanical impedance Z_{mech} via the area *A* of the boundary:

$$Z_{mech}=AZ_a=A^2Z_{ac} \tag{4.34}$$

The point source location was at (2.8 m, 3.5 m) and a simulative uniform linear microphone array was adopted. The whole geometry of the simulation is shown in Figure 4.4.

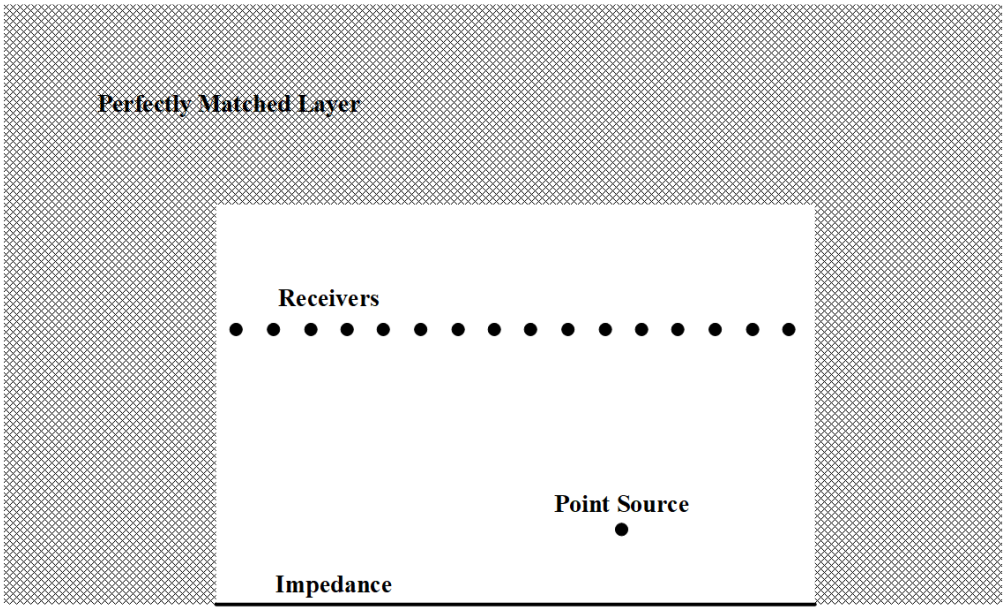

Figure 4.4 Geometry of the simulation by COMSOL.

Figure 4.5 shows the simulated localisation results obtained using the DAS, MUSIC, weighted broadband DAS, and weighted broadband MUSIC methods. Because the impedance domain was active under the sound area, in Figure 4.5(1a) and (1b) the sidelobes and the main lobe in the sound map are hardly distinguishable. The performance of the conventional DAS and MUSIC could be severely disrupted by the reflection effect. Comparing these two plots, the mentioned condition is slightly improved in Figure 4.5(1b) because the MUSIC method is credited with a higher spatial resolution and lesser sidelobes. Figure 4.5(2a) shows the localisation result of weighted broadband DAS. The sidelobes in this plot are much lesser, yet the spatial resolution is still low, and the point source at (2.8 m, 3.5 m) and its image source at (2.8 m, 2.5 m) due to the impedance combine into one main lobe. The aforementioned problems are perfectly solved in

Figure 4.5(2b) by BW-MUSIC. The localisation result is quite accurate, and nearly no sidelobe distortion may be noticed in the sound map.

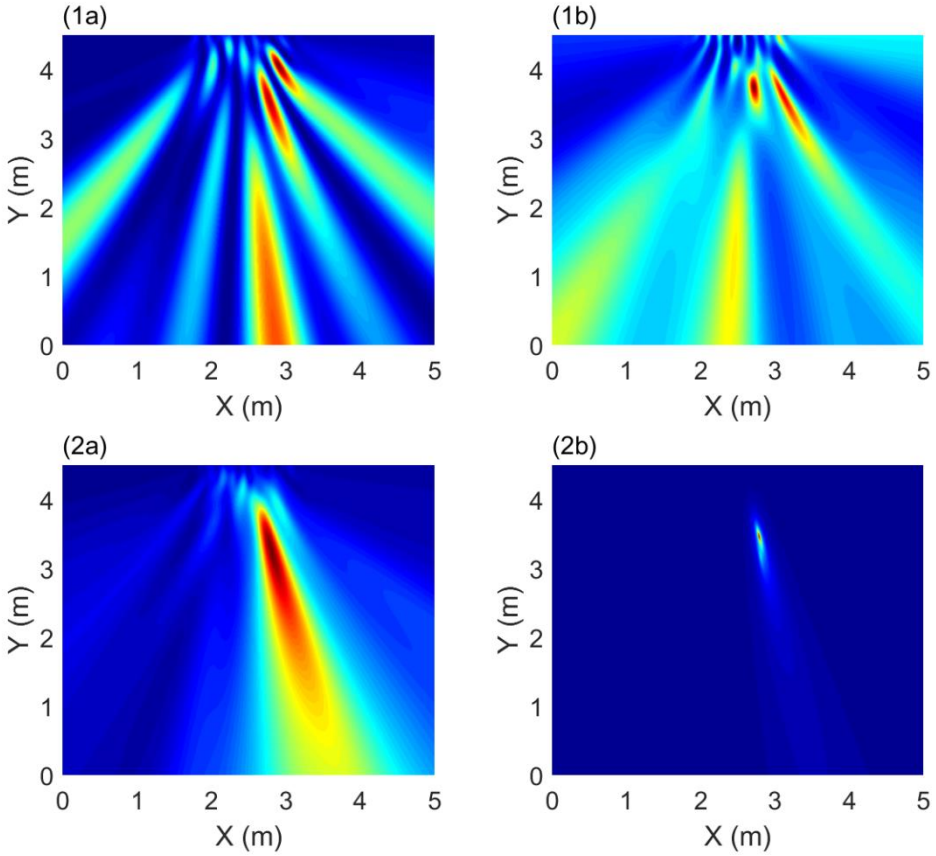

Figure 4.5 Localisation results from DAS (1a), MUSIC (1b), weighted broadband DAS (2a), and weighted broadband MUSIC (2b).

4.4 Experimental study

4.4.1 Initial localisation results from broadband weighted MUSIC

As the simulation comparison results of B-MUSIC and BW-MUSIC show, the sound map which is not weighted by the multiple FT results can be distorted by the superposition of the sidelobes. Experimental testing is conducted to compare these two methods. All experiments were performed in a semi-anechoic chamber with a background noise level of less than 15 dBA, and a cut-off frequency of 80 Hz to avoid sound reflections from the surrounding walls and ceiling. In particular, the original wire gauze floor of the anechoic chamber is covered by timber sheeting to achieve the sound wave propagation model with ground effect. Figure 4.6 shows the experimental setup consisting two roller test rigs, a 32-channel quadrate microphone array, two Brüel & Kjær Type 2694-A 16-channel DeltaTron conditioning amplifiers, eight NI 9234 four-channel data acquisition cards, and a desktop computer.

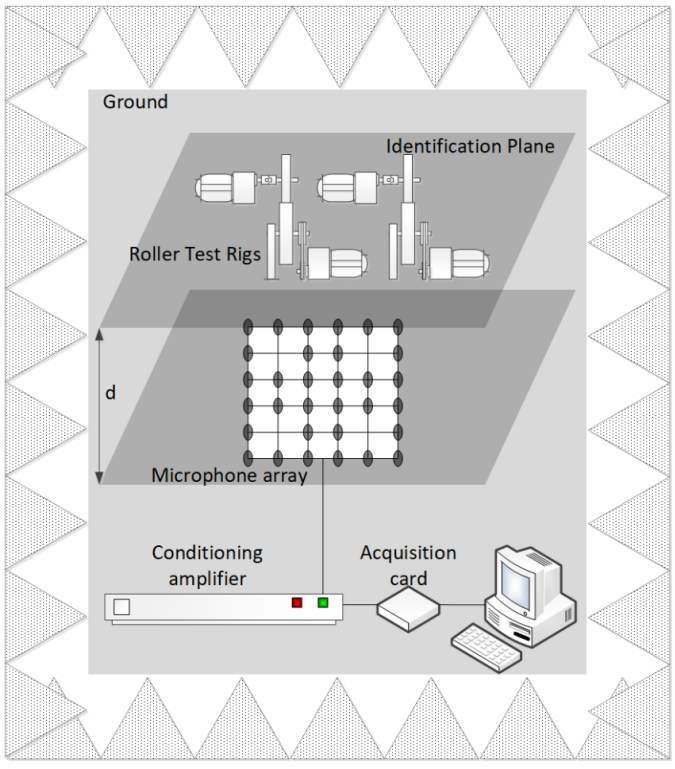

Figure 4.6 Experimental setup

In the localisation results that are shown in Figure 4.7, two random noise sound sources tagged as □ and ○ are installed in the identification plane. The x-axis is set as the ground surface so that the fourth quadrant in the sound map indicates the localisation of image sources, which are tagged as ◇ and X. Figure 4.7(a) shows the localisation results of B-MUSIC while Figure 4.7(b) shows the localisation results of BW-MUSIC. Due to the difference in volume of the two sound sources, the beamformer output at □ is significantly higher than ○. In Figure 4.7(a) a bulk of superposition of sidelobes around the sound sources can be easily noticed in consequence of the ground effect. The image sources and sound sources are mixed together in this sound map. The challenge is noticeably improved in Figure 4.7(b). With the weighting by the multiple FT results, the beamformer outputs at sound source locations are enhanced. The image sources are separated from the sound sources with a much weaker sound power in the fourth quadrant.

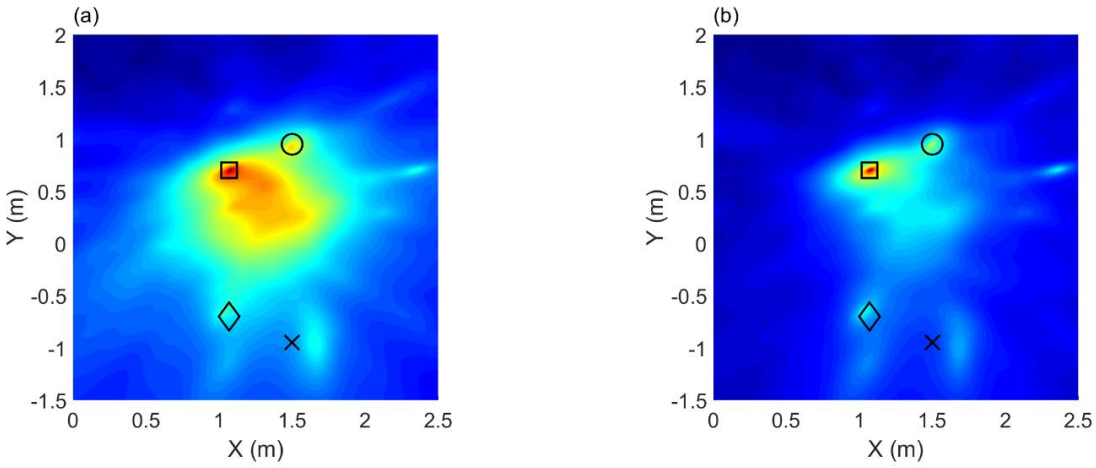

Figure 4.7 Localisation results from broadband MUSIC and weighted broadband MUSIC (□ and ○: location of sound sources, ◇ and X: location of image sources). (a) broadband MUSIC localisation result, (b) weighted broadband MUSIC localisation result.

4.4.2 Compared with kurtosis beamformer

In this section the random noise sound sources in Figure 4.7 are replaced by two roller test rigs with healthy and faulty wheels. Figure 4.8 shows the fault detection and localisation results by comparing the B-MUSIC, BW-MUSIC, time-domain DAS beamforming, and kurtosis beamforming methods. The x-axis in Figure 4.8 is also set as the ground surface. Consistently, in Figure 4.8, the healthy and faulty wheels are tagged as □ and ○, respectively, and the corresponding image sources are tagged as ◇ and X. In this case, the performance of the B-MUSIC and BW-MUSIC methods is nearly the same. The influence of the superposition of sidelobes in Figure 4.8(1a) is not remarkable compared with the

sound map in Figure 4.8(1b). In order to highlight the ability of the fault detection of kurtosis beamforming method, the sound volume of the roller test rig with the healthy wheel is set louder. Therefore, the amplitude of the beamforming output at □ is appreciably higher than ○ in Figure 4.8(1a) and (1b).

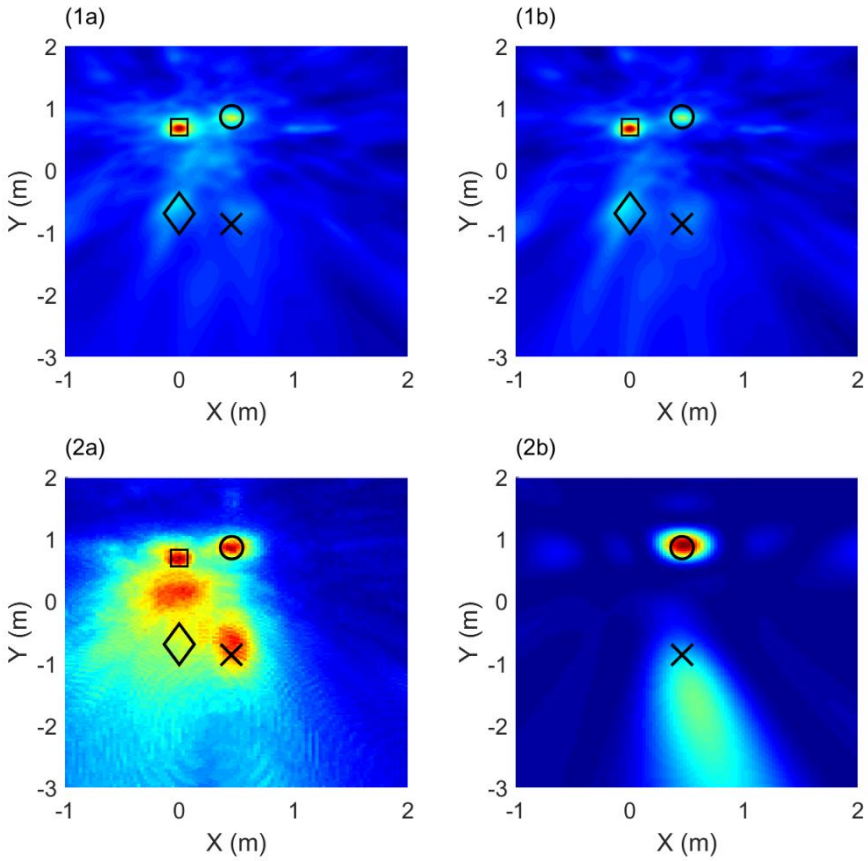

Figure 4.8 Fault detection and localisation results for a healthy wheel and a faulty wheel (□: location of the healthy wheel, ○: location of the faulty wheel, ◇ and X: location of image sources). (1a) broadband MUSIC localisation result, (1b) weighted broadband MUSIC localisation result, (2a) time-domain DAS beamforming result, (2b) kurtosis beamforming result.

Table 4.1 shows the percentage error in both the x and y-directions of fault

detection and localisation by different methods, which is defined as the ratio between the error and the actual fault location in percentage:

$$\delta_x = 100\% \times \left| \frac{x_a - x_e}{x_a} \right| \tag{4.35}$$

$$\delta_y = 100\% \times \left| \frac{y_a - y_e}{y_a} \right| \ , \tag{4.36}$$

in which x_a and y_a are the actual fault coordinates, while x_e and y_e are the estimated coordinates by the beamforming approach. The fault detection and localisation results are observed to be accurate.

Table 4.1

Percentage error of fault detection and localisation by kurtosis beamforming

Localisation method	x-direction	y-direction
Kurtosis beamforming	2.08%	3.45%

4.4.3 Ground impedance estimation results from the Levenberg–Marquardt and Crank Nicolson method

As mentioned in Sections 4.2.4 and 4.4.1, the LM–CN method is a better parameter estimation approach than the LM method for ground impedance estimation. With the results from BW-MUSIC as the initial inputs of the source location, the LM–CN method is performed in this section of the study. The estimation in the real and imaginary part of normal ground impedance from 500 to

6,000 Hz in the former experiment is shown in Figure 4.9. The real part of the normal impedance ranges from 0.93 to 0.99, while the imaginary part ranges from -0.03 to 0.11. Because the image source was expected to be considerable in this study, a hard timber sheeting covered with paint was employed as the imitation of the ground, and the estimated ground impedance in the experiment was extremely high. The accuracy of the estimation results was confirmed in the following.

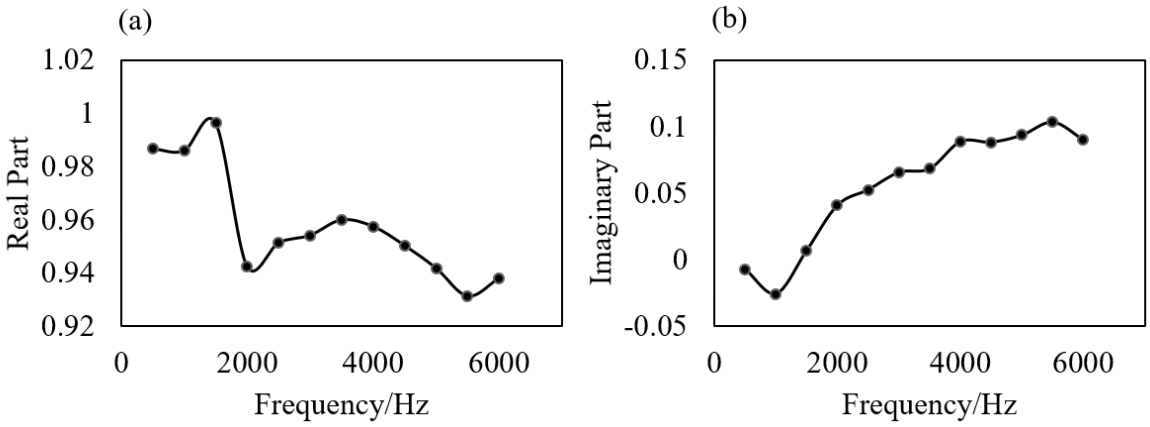

Figure 4.9 Normal impedance of ground surface estimation by the LM–CN method. (a) real part, (b) imaginary part.

Figure 4.10 shows the percentage error of normal impedance estimation in both the real and imaginary part. In Figure 4.10(a), the fluctuation of errors from 500 to 6,000 Hz is very slight. The largest percentage error (5.31%) occurs at 1,500 Hz. The performance of normal impedance real part estimation is quite acceptable. However, in Figure 4.10(b), the largest percentage error increases to 108.30%. The percentage error of one-third of the estimation results in impedance in the imaginary part is larger than 24%, especially in the low frequency range. Referring

to the estimation results in Figure 4.10(b), in the low frequency range from 500 to 1,500 Hz, the value of the imaginary part is very close to 0. This could be the reason why the percentage error is quite large. In this range, small deviations could lead to a large error.

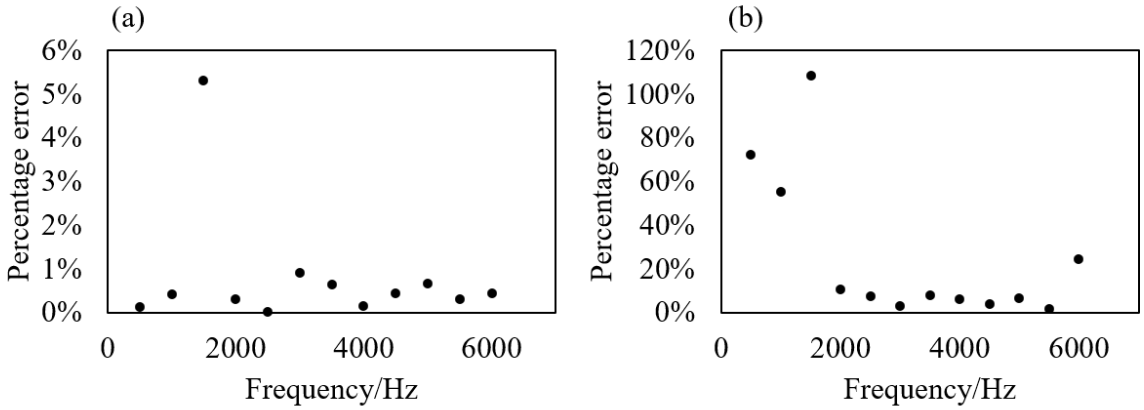

Figure 4.10 Percentage error of normal impedance estimation. (a) real part, (b) imaginary part.

4.5 Chapter summary

The objective of this chapter is to propose a hybrid microphone array signal processing approach for faulty wheel identification and ground impedance estimation. The performance of BW-MUSIC was compared with the previous LM and MUSIC method by simulation and experimental study to locate the sound source. Compared with the MUSIC and B-MUSIC methods, performance of BW-MUSIC with ground reflection and broadband signals is much better. In the simulation by FEM, with the interference of imitative ground reflection, the

localisation result by BW-MUSIC was more accurate than other methods. The range of the mainlobe was smaller, with nearly no sidelobe distortion. Consistent results were achieved in the experimental study. With multiple sound sources and ground reflection, the BW-MUSIC method provided a separate and distinct localisation result in the sound map compared with B-MUSIC.

In numerical simulation by MATLAB, the impedance of the reflecting ground surface can be estimated by the LM–CN method. Compared with the former LM approach to estimate ground impedance, the LM–CN method provides a preferable convergence path. The rate of convergence among all parameters is improved. The convergence values by LM–CN method are closer to the actual values than the LM method. In the experimental study, the estimation results and their accuracy in the real and imaginary part of normal ground impedance from 500 to 6,000 Hz is shown.

CHAPTER 5

Moving sound source localization

5.1 Introduction

During the beamforming processing, for the moving sources, whose position is continuously changing with respect to the operation time, the traditional beamforming output could only provide a blurred sound map of the paths on which the moving sources travelled. To utilize the beamforming technique on the moving source localization approach, the Doppler effect must be eliminated (Bao, 2014; Howell, Bradley, McCormick, & Brown, 1986). Therefore, the traditional beamforming method should be modified.

The modification of the beamformers are studied in two different directions. One straightforward method is assuming that the distance between the moving sound source and the receiver is much longer than the moving distance of the source during sound signal acquisition. In such short period, which is usually less than 1 s subject to the sampling rate, the moving sound source could be regarded as a stationary source. Considering the instantaneous frequency at the receiver due to Doppler amplification should be a function of Mach number, the computational

frequency should be modified while the rest parts of the beamforming algorithm could remain the same as the traditional frequency-domain methods (Huang, Teng, & Sun, 2016; Valin, Michaud, Hadjou, & Rouat, 2004).

The other compensation of the Doppler distortion method is conducted in the time-domain (Kim & Choi, 2013; Nakajima, Nakadai, Hasegawa, & Tsujino, 2007; X.-Z. Zhang, Bi, Zhang, & Xu, 2015). It is often called the de-Dopplerization approach. By using the de-Dopplerization approach, the pressure signal at the receiver can be reconstructed. Then the situation can be regarded as a moving receiver along with the moving sound source. Consequently, the traditional time-domain beamforming method could be applied (Chen & Choy).

In this chapter, a sound wave propagation model with moving source will be established at first. Then the mentioned frequency shift method and de-Dopplerization approach will be introduced. Based on which, the proposed BW-MUSIC and kurtosis beamformer will be utilized on the moving source localization and be compared and discussed in detail. In the end of the chapter, an outdoor measurement would be presented to validate the proposed approaches.

5.2 Methodology

5.2.1 Sound wave propagation model with moving source

For moving sound signal whose position in sound field, as it is shown in Figure 5.1, is continuously changing with respect to time τ, two main distortions in time-domain should be considered in the localization approach. First is the arrival time of sound signal and the second is Doppler amplification. For a linear motion with a speed v_0, the measured sound pressure at observation position $\mathbf{r} = [x, y, z]$ in time-domain is given by:

$$p(\mathbf{r}, t) = \frac{q_0(\tau)}{4\pi |\mathbf{r} - \mathbf{r}_0(\tau)|} \frac{1}{|1 - M_0(\tau)|} \tag{5.1}$$

in which q_0 is the time signal, $\mathbf{r}_0 = [v_0 \tau_j, 0, 0]$ is the position of source and M_0 is the Mach number term:

$$M_0(\tau) = \frac{v_0}{c} \frac{x - v_0 \tau}{\sqrt{(x - v_0 \tau)^2 + y^2 + z^2}} \tag{5.2}$$

which typically ranges from 0.02 to 0.1 (20 km/h to 120 km/h) for urban train noise. The received time signal $p(\mathbf{r}, t)$ from a moving source is a non-stationary and frequency varying signal. The conventional approach of signal processing with long sampling time to average out the background noise is not directly applicable for frequency-domain based array processing method. For time varying signals, a short-time processing approach is adopted in next section in order to limit the frequency bandwidth of the analysis and minimize the spatial travel distance of the moving source. In frequency-domain, the sound pressure fluctuation of a moving source at the receiver has a phase:

$$\varphi_s = \omega_s (t - r / c) \tag{5.3}$$

and thus, the instantaneous frequency at the receiver due to Doppler amplification is:

$$\omega_i = \frac{\partial \varphi_s}{\partial t} = \frac{\omega_s}{1 - M\cos\theta} \tag{5.4}$$

in which the incident angle θ could be assumed invariant during the signal acquisition time due to that the moving distance could be negligible compared with the distance between the moving sound source and the receiver. Accordingly, such assumption could only be made in the low Mach number situations. In high Mach number situations, de-Dopplerization approach in time-domain is recommended in Section 4.2.3 to avoid the frequency shift problems.

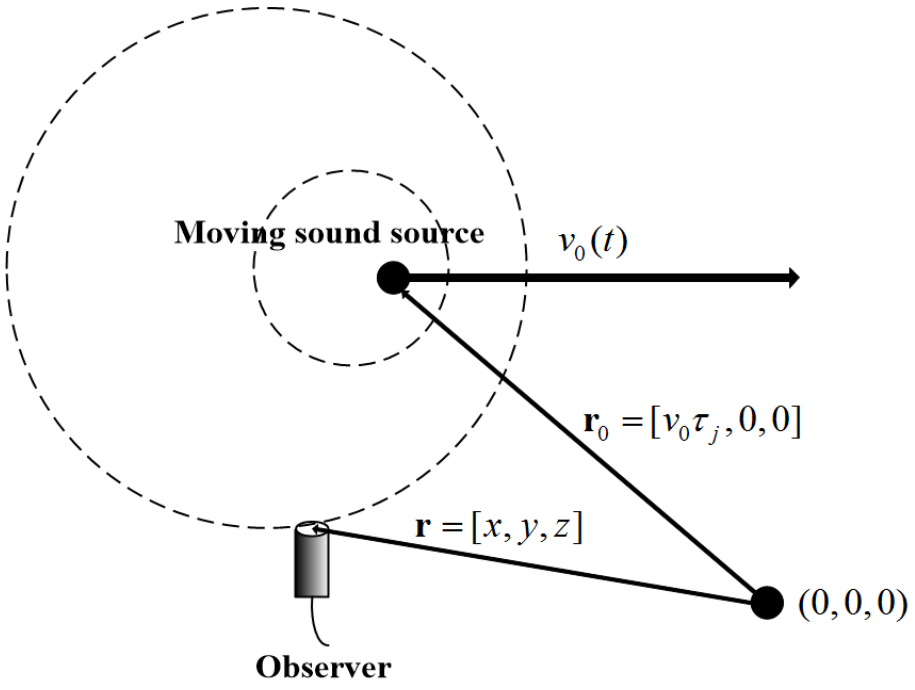

Figure 5.1 Propagation wavefront produced by a moving sound source.

5.2.2 Short-time processing approach

The BW-MUSIC method introduced in Chapter 4 is adopted in this section. Re-call the BW-MUSIC output:

$$\beta_{WBM}(r_m) = \frac{1}{N}\sum_{f=f_0}^{f_N} F(f)\beta_{MUSIC}(r_m, f) \tag{4.24}$$

To be compared with which, the broadband weighted DAS (BW-DAS) output can be written similarly as:

$$\beta_{WBD}(r_m) = \frac{1}{N}\sum_{f=f_0}^{f_N} F(f)\beta_{DAS}(r_m, f) \tag{5.5}$$

in which $\beta_{DAS}(r_m, f)$ is the traditional DAS beamforming power at near-field assumption:

$$\begin{aligned}\beta_{DAS}(r_m, \omega) &= E[|b(r_m, \omega)|^2] \\ &= \mathbf{w}(r_m, \omega)^H \mathbf{R}(\omega)\mathbf{w}(r_m, \omega)\end{aligned} \tag{5.6}$$

Figure 5.2 shows the experimental setup of a moving track with the loudspeakers. The purpose of this experiment is to examine the feasibility of locating the defect of the wheel/rail system when the trolley moves. To imitate the wheel/rail system operating, a belt track carried a plastic stand with three loudspeakers was utilized in the following experiment. The belt was driven by a servo motor (57hbm20-1000), which can be controlled by a touch screen control panel. A lineal microphone array containing 16 microelectrical-mechanical system (MEMS) microphones was used in the experiment, with a 0.1m gap between each two adjacent microphones. The belt track simulates that the train is moving, and the loudspeakers are regarded as moving sound sources. The lineal microphone

array is regarded as X-axis and the first MEMS microphone is regarded as zero point in the whole geography. The reflections and reverberation effect were not considered in this section. Owing to limitation of space, it is difficult to conduct the experiment of the real railway system or movable wheel system in the anechoic chamber. Hence, the sound of the noise radiated from different types of faults from the wheel in the roller test rig was recorded and generated through the loudspeakers that were fixed on a movable trolley in the anechoic chamber.

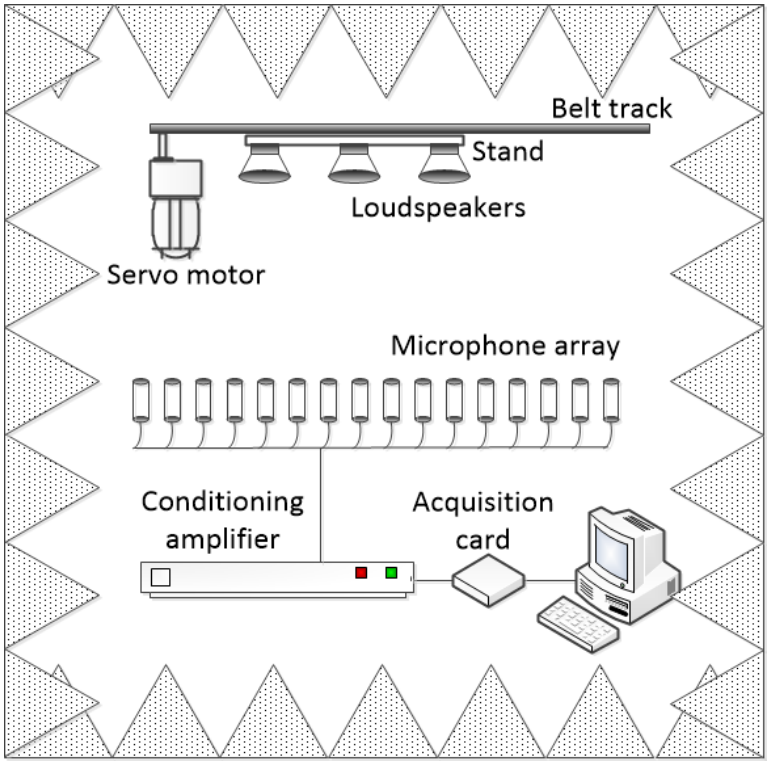

Figure 5.2 Experimental setup of moving sound sources.

Figure 5.3 shows the sound maps computed by using BW-DAS and BW-MUSIC method in all 10 s measurement time. One single pristine wheel source is moving from left to right by a uniform velocity which is 0.5 m/s. As it is discussed

before, the overall calculated beamforming output could only provide a blurred sound map. In Figure 5.3(a) two sound sources could be found at the moving path of the sound source, and in Figure 5.3(b) the sidelobe makes the sound map nebulous. Both of these two localization approaches failed to reflect the accurate position of the moving source.

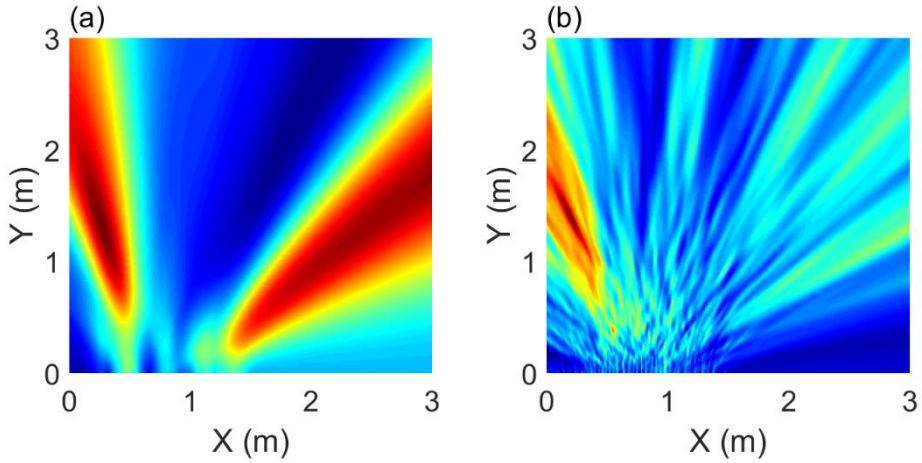

Figure 5.3 Localisation results from BW-DAS (a), and BW-MUSIC (b) in 10 s (Moving speed is 0.5 m/s).

The same experimental conditions were repeated in the next case. The measurement time was still remaining 10 s. However, in this case, the computational time is 0.5 s. Under such situation, the moving source could be assumed stationary in 0.5 s. Figure 5.4 shows the localisation results at 0 s and 2 s, respectively. In general, the localization results of BW-DAS and BW-MUSIC in Figure 5.4 are much better than which are shown in Figure 5.3. Only one clear sound source could be discovered in each plot. In addition, the location of the sound source computed by BW-MUSIC is much accurate in Figure 5.4(1b) and

(2b) than which is computed by BW-DAS in Figure 5.4(1a) and (2a). Since the moving speed of the source was 0.5 m/s in this case, the sound source location translates 1 m comparing Figure 5.4(1b) and (2b). Therefore, the short-time processing approach in frequency-domain is feasible to trace the moving source.

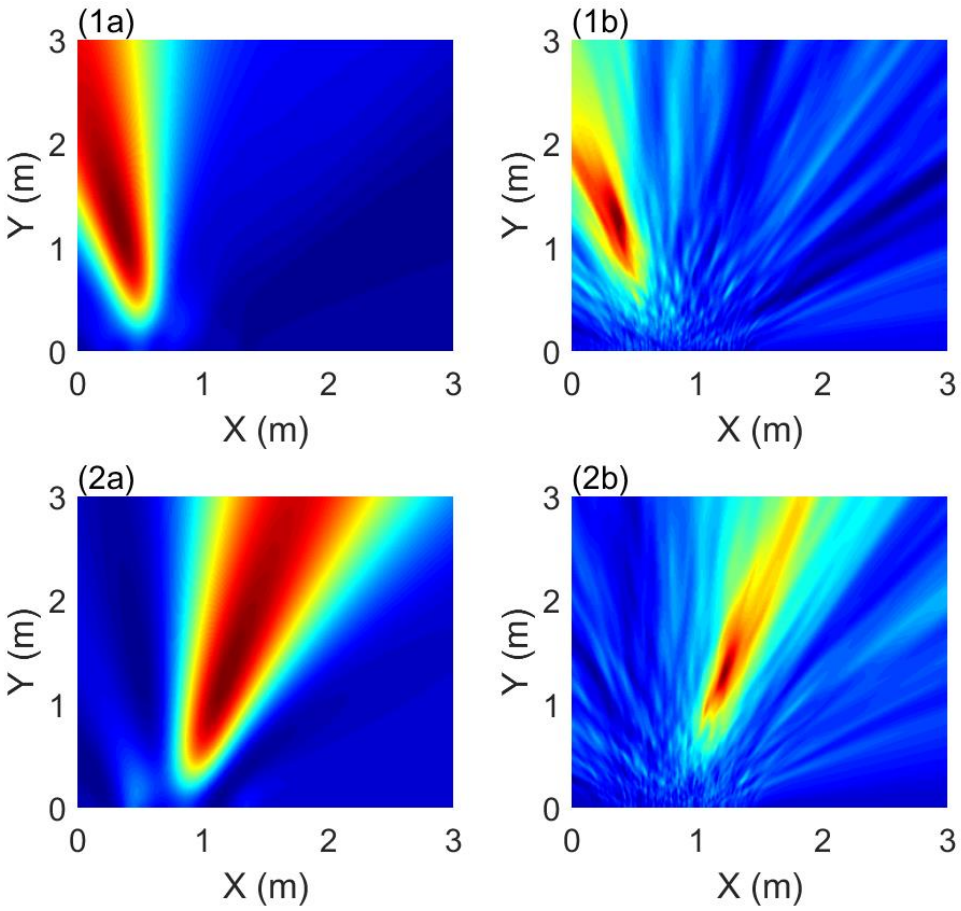

Figure 5.4 Localisation results of pristine wheel from BW-DAS (1a), BW-MUSIC (1b) at 0 s, and BW-DAS (2a), BW-MUSIC (2b) at 2 s (Moving speed is 0.5 m/s).

In the case showed in Figure 5.5, the pristine wheel was replaced by the wheel-flat while the other experimental conditions remained the same as former

cases. The computational time is still 0.5 s in each plot, and Figure 5.5 shows the results which is consistent with the results shown in Figure 5.4

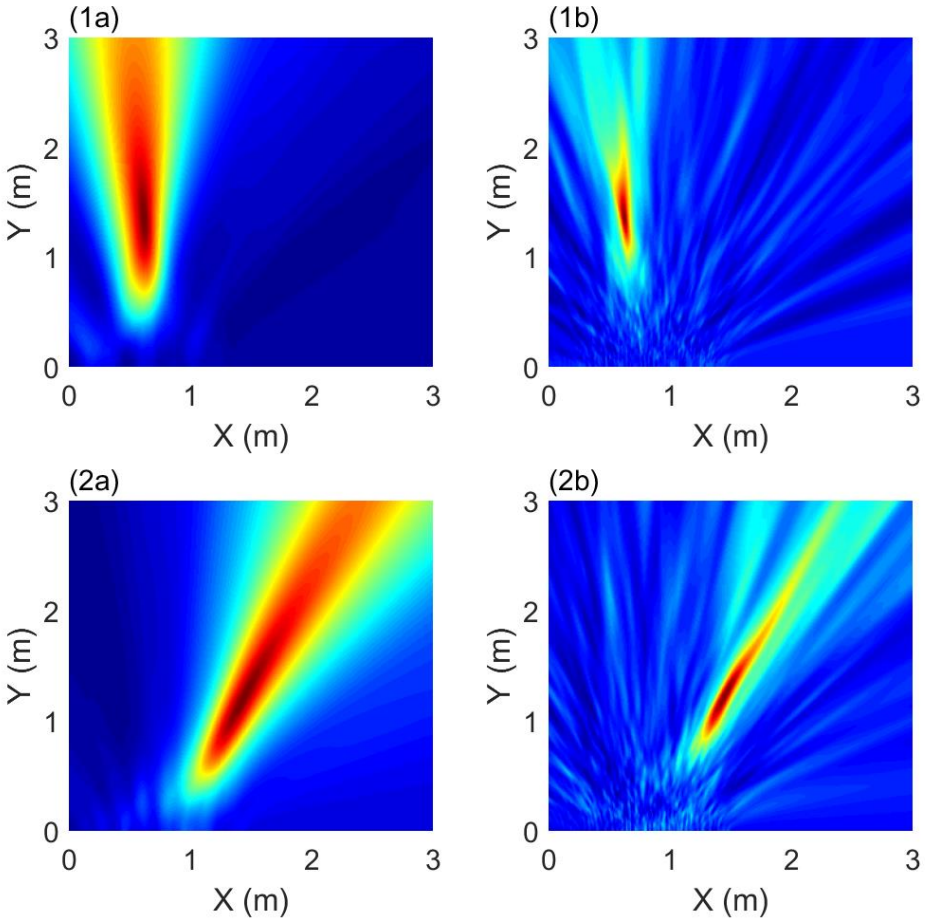

Figure 5.5 Localisation results of wheel-flat from BW-DAS (1a), BW-MUSIC (1b) at 0 s, and BW-DAS (2a), BW-MUSIC (2b) at 2 s (Moving speed is 0.5 m/s).

The last case was designed to investigate the reliability of the short-time processing approach when it is utilized to localize the multiple sources. Two loudspeakers, including a pristine wheel and a wheel-flat, were set on the stand at the belt track. The moving speed of the belt track is 0.3 m/s. Figure 5.6 shows the

localisation results of BW-DAS and BW-MUSIC of two moving sources. Unlike the former cases containing one single source, the advantage of the BW-MUSIC method in elimination of sidelobes is not obvious compared with the BW-DAS method during multiple sources localization. In Figure 5.6(2a) only one conspicuous source could be observed, while in both Figure 5.6(2a) and (2b) the effect of sidelobe is prominent. However, overall, the ability of tracing the multiple moving sources is acceptable by short-time processing approach. It could be observed easily that the two sources moved toward right at a speed of 0.3 m/s.

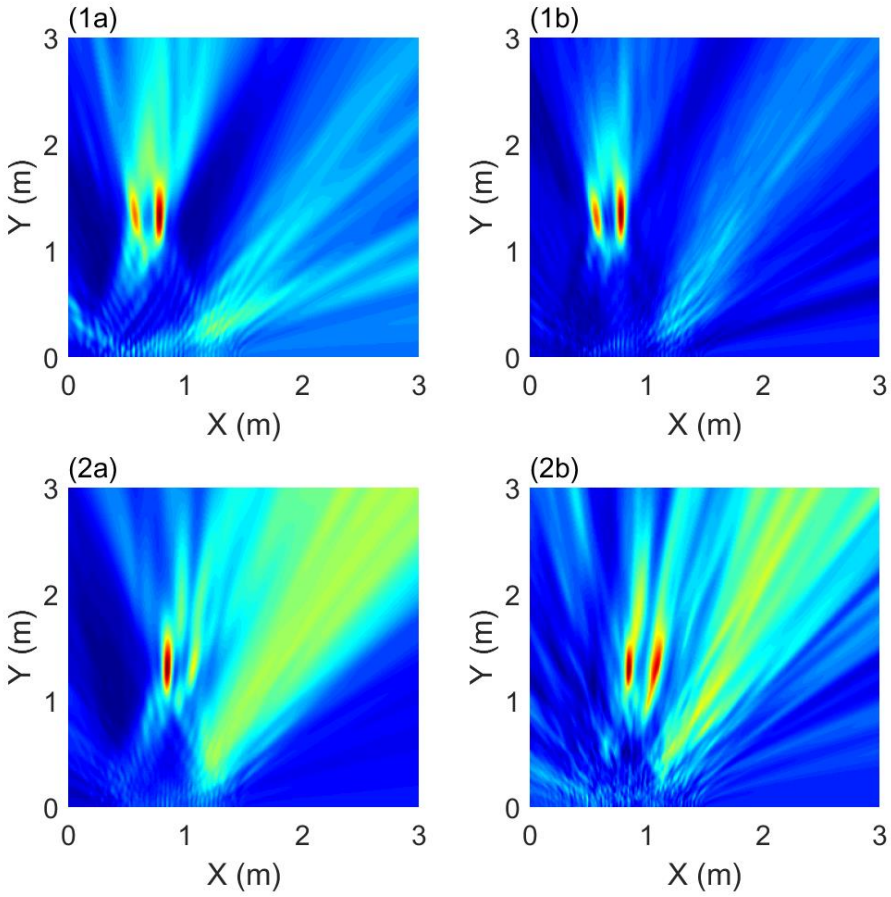

Figure 5.6 Localisation results of multiple sources (pristine wheel and wheel-flat) from BW-DAS (1a), BW-MUSIC (1b) at 1 s, and BW-DAS (2a), BW-MUSIC

(2b) at 2 s (Moving speed is 0.3 m/s).

5.2.3 De-Dopplerization approach

To neutralize the distortion of Doppler amplification, a method called de-Dopplerization can be adopted in beamforming localization approach. Use the relation of equation (5.1), the source signal can be estimated as:

$$q_0(\tau) = 4\pi \left|\mathbf{r} - \mathbf{r}_0(\tau)\right| \left|1 - M_0(\tau)\right| p(\mathbf{r}, \tau + \frac{\left|\mathbf{r} - \mathbf{r}_0(\tau)\right|}{c}) \qquad (5.7)$$

in which the sound pressure is assumed to be measured by a fixed microphone array.

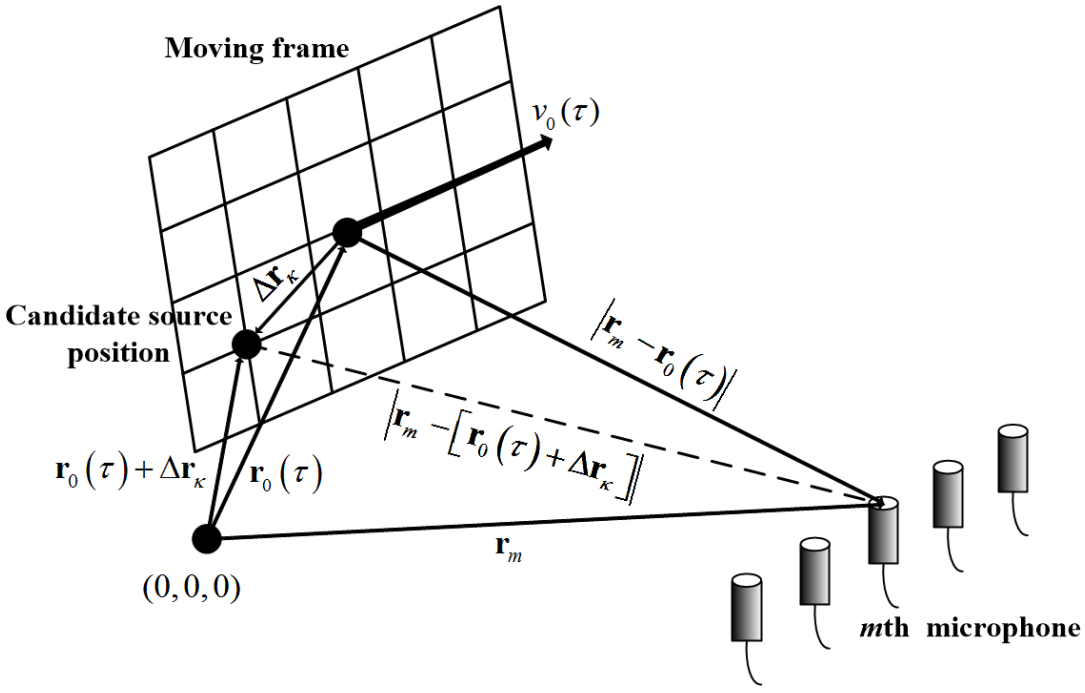

Figure 5.7 De-Dopplerization beamforming approach with sound source on a moving frame.

Assume K source signals in a moving frame as it is shown in Figure 5.7 with a centre $\mathbf{r}_0(\tau)$ and the speed v_0 is estimated by m microphones. Each position of the source signals can be expressed as $\mathbf{r}_0(\tau)+\Delta\mathbf{r}_\kappa$ (κ=1,$\cdots$,K), the de-Dopplerized time-domain beamforming output can be written as:

$$b(\Delta\mathbf{r}_\kappa,\tau)=\frac{1}{M}\sum_{m=1}^{M}4\pi\left|\mathbf{r}_m-\left[\mathbf{r}_0(\tau)+\Delta\mathbf{r}_\kappa\right]\right|\left|1-\frac{|v_0(\tau)|}{c}\cos\varphi_{m\kappa}(\tau)\right| \cdot p(\mathbf{r}_m,\frac{\tau+\left|\mathbf{r}_m-\left[\mathbf{r}_0(\tau)+\Delta\mathbf{r}_\kappa\right]\right|}{c}) \tag{5.8}$$

in which c is speed of sound, $\mathbf{r}_m$ is the position of mth microphone and $\cos\varphi_{m\kappa}(\tau)$ is the angle between the direction of $\mathbf{v}_0$ and $\mathbf{r}_m-\left[\mathbf{r}_0(\tau)+\Delta\mathbf{r}_\kappa\right]$.The corresponding kurtosis beamformer for moving source can be defined and calculated by:

$$Kurt(r_m)=\frac{E\{[b(\Delta\mathbf{r}_\kappa,\tau)-\mu(\Delta\mathbf{r}_\kappa,\tau)]^4\}}{[\sigma(\Delta\mathbf{r}_\kappa,\tau)]^4} \tag{5.9}$$

in which $\mu(\Delta\mathbf{r}_\kappa,\tau)$ is the mean of $b(\Delta\mathbf{r}_\kappa,\tau)$, $\sigma(\Delta\mathbf{r}_\kappa,\tau)$ is the standard deviation of $b(\Delta\mathbf{r}_\kappa,\tau)$.

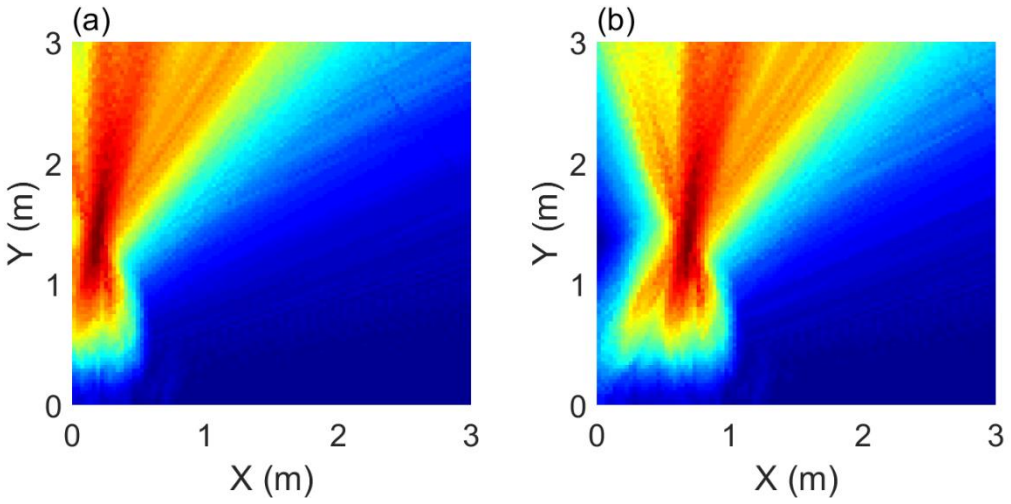

Figure 5.8 Localisation results for single pristine wheel: (a) DAS beamforming power at 0 s, and (b) DAS beamforming power at 1 s (Moving speed is 0.3 m/s).

Figure 5.8 shows the sound maps at 0 s and 1 s, in which the stand carrying a loudspeaker moved toward right at a speed of 0.3 m/s. One clear sound sources could be discovered in Figure 5.8 from the sound map. Obviously the de-dopplerization approach is effective to trace the moving sound source. Since the moving speed of the sources was 0.3 m/s in this case, the sound source location translated 0.3 m comparing the Figure 5.8(a) and (b).

In the case shown in Figure 5.9 the pristine wheel was replaced by the wheel-flat in order to investigate the performance of integrated approach which combing the de-Dopplerization method in time-domain and kurtosis beamformer. The first row shows the localisation results computed by traditional DAS beamformer with de-Dopplerization while the second row shows the localisation results computed by kurtosis beamformer. The moving speed of the wheel-flat is 0.3 m/s as well. It can be discovered from the Figure 5.9(1a), (1b) and (1c) that the sound source moves toward right at the speed of 0.3 m/s consistently. The sound map is vaguer in the second row, which is computed by kurtosis beamformer. This is mainly because that there is only one single source in the sound area. The kurtosis value of the whole sound area is relatively high. Therefore, the performance of the kurtosis beamformer could be worse. The mainly application of the kurtosis

beamformer is to identify the fault from other sound sources, including pristine wheel and background noise. Such situation would be discussed in the next case. However, in this case shown in Figure 5.9(2a), (2b) and (2c), the integration of de-Dopplerization approach and kurtosis beamformer is practicable. As a technology computed in time-domain, the kurtosis beamformer could trace the moving sound source as well as the traditional DAS beamformer.

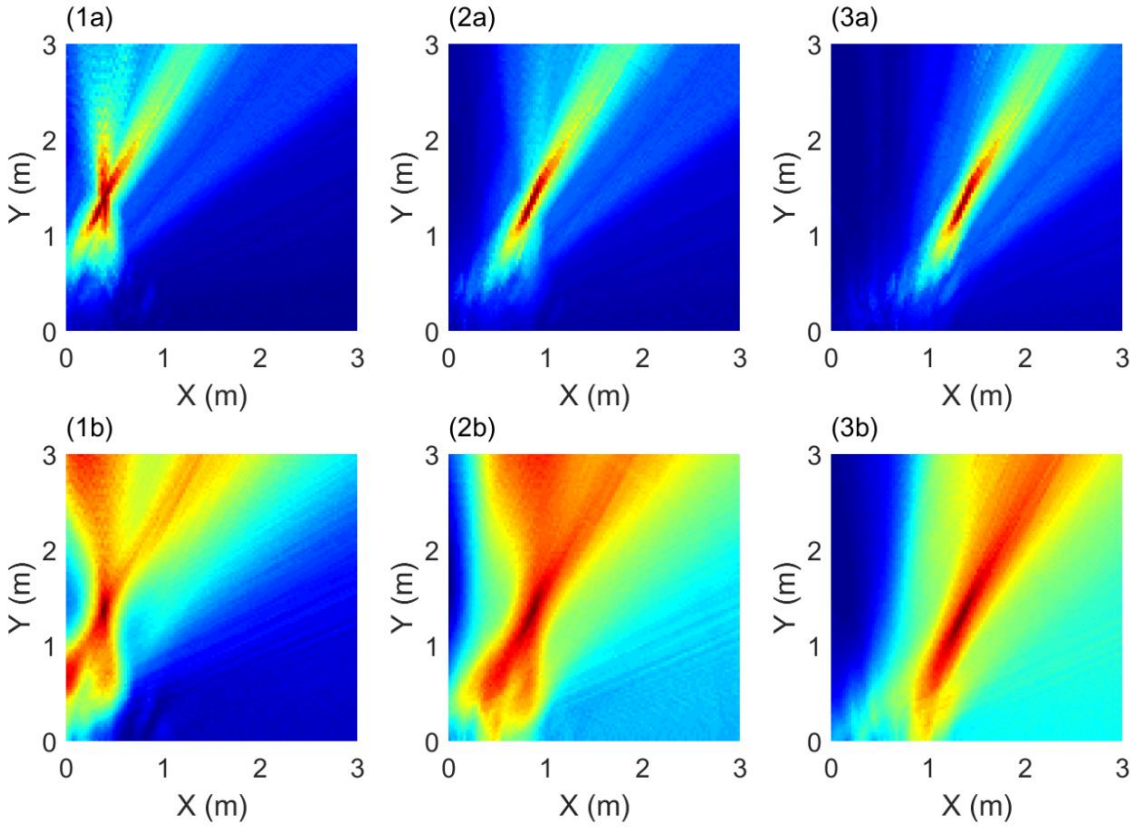

Figure 5.9 Fault detection and localisation results for single wheel-flat: (1a) DAS beamforming power at 0 s, (2a) DAS beamforming power at 1 s, (3a) DAS beamforming power at 2 s, (1b) kurtosis beamforming at 0 s, (2b) kurtosis beamforming at 1 s, and (3b) kurtosis beamforming at 2 s (Moving speed is 0.3 m/s).

In the next case the trolley carried three loudspeakers moved at a speed of 0.2 m/s. Figure 5.10 shows the traditional DAS beamformer compared with the kurtosis beamformer during detecting and localising three moving sound sources. The symbols of circle, diamond, and square represent the location of the loudspeaker generating random noise, the sound of wheel with fault, and that of the wheel without fault, respectively. Figure 5.10(1a) and (1b) show the beamformer evaluated by RMS and kurtosis, respectively, for the trolley that has moved after 2 s. Figure 5.10(1a) shows that the location of the loudspeaker generating random noise can be revealed while the wheel with fault is marginally observed. This is primarily because the SPL of the background noise is set rather higher compared to the other two signals. Figure 5.10(1b) shows that the speaker generating the wheel with fault can be recognised and is easier to be distinguished from the high background noise. Figure 5.10(2a) and (2b) show the beamformer evaluated by RMS and kurtosis, respectively, for the trolley that had moved after 4 s. Figure 5.10(2b) shows that the location of the speaker generating the sound of the wheel with fault can be traced using the de-Dopplerisation and kurtosis beamforming approach. Although the present experimental test is limited to the speed of approximately 0.1 m/s to 0.5 m/s owing to the space issue, the results of Figure 5.10 shows that the de-Dopplerisation and kurtosis beamforming approach are feasible to trace the wheel with fault.

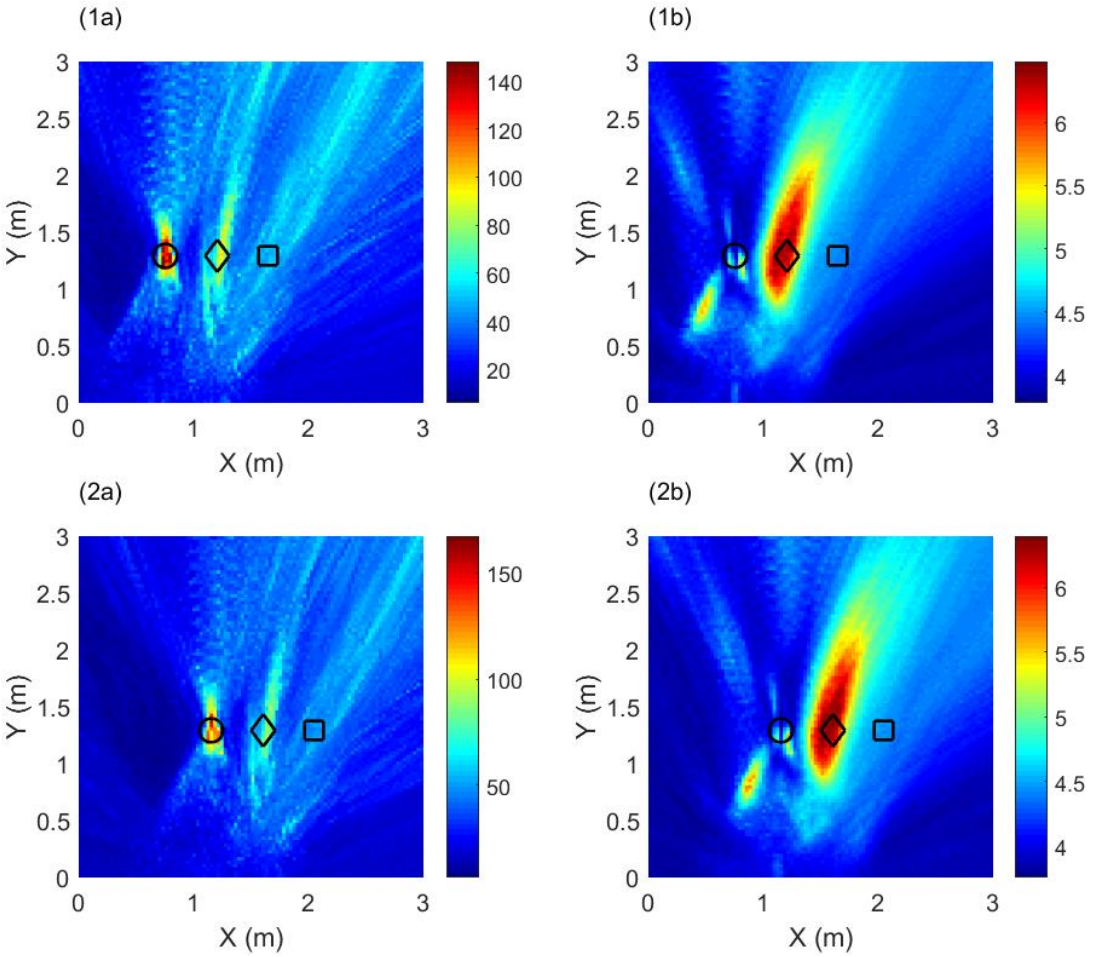

Figure 5.10 Fault detection and localisation results for moving sound sources (○: background white noise, ◇: wheel with fault, and □: wheel without fault): (1a) DAS beamforming power at 2 s, (1b) kurtosis beamforming at 2 s, (2a) DAS beamforming power at 4 s, (2b) kurtosis beamforming at 4 s (Moving speed is 0.2 m/s).

5.3 Chapter summary

In this chapter, the fault detection and localization approach is extended to the moving sound source. The wave propagation model of moving source is first introduced in Section 4.2.1. Then the modification of the beamformer to utilize on

the moving sound source localization are studied in two different directions. The short-time processing by using BW-DAS and BW-MUSIC method is proposed to localize the moving source in low Mach number in frequency-domain. The ability of which to trace the single and multiple moving sources is acceptable.

The de-Dopplerization approach integrated with kurtosis beamformer for fault identification and localization was developed next, which can extract the impulsive feature from original sound signals and locate the position of specific sound source. To localise the moving sound source in high Mach number, de-Dopplerization approach in time-domain were first introduced and applied in Section 4.2.3. To identify the fault, beamforming kurtosis were intergrated with de-Dopplerization approach, and in the experimental section the calculated results presented in sound maps had a good matching with the actual conditions in terms of localizing and identifying. In the first place the localization results for three moving sources were acceptable, furthermore the improved sound maps can identify wheel fault with the interference of background noise.

CHAPTER 6

Conclusions and Suggestions for Future Research

6.1 Conclusions

The approaches for the fault localization and characterization in wheel/rail system has been proposed in this thesis. In Chapter 2, the statistic estimator kurtosis is firstly integrated with beamforming technique to detect the impulsive features of sound signals. Chapter 3 considers and discusses the possibility of application of the kurtosis beamformer in many respects. In Chapter 4 and 5, the effect of the ground reflection and moving source is studied, respectively.

Fault detection in wheel/rail system has been studied extensively. To be start with, after introducing the propagation models of acoustic signals, the SK method for fault detection of impulsive signals is well studied and developed into WT-based SK method, which has the smoother curve and more outstanding peak. However, it has been proved by experimental study that the SK method can not distinguish the impact noise from the rolling noise in frequency-domain. Therefore, the so-called Kurtosis beamformer has been proposed for such situation. By the

validation of experiments, the kurtosis beamformer in time-domain is feasible to distinguish the location of the wheel with fault from the pristine wheel.

Further studies including applying different types of faults and SNR in the experiments have been conducted. Compared with the RMS and peak value, the ability of kurtosis beamformer to extract the impulsiveness emerging from the background noise is much stronger. The impact noise generated by a slightly defect on the structure surface could be still detected by the kurtosis beamformer. In addition, When the background noise is high, the kurtosis beamformer remains effective. Compared with the current state-of-the-art NDT techniques, for instance, the ultrasonic technique, magnetic method and AE technique, the main advantage of kurtosis beamformer is that it does not require the contact between sensors and structure.

Since in reality during the sound wave propagation, the ground reflection effect should not be ignored. Considering the ground impedance is a function of frequency, the simulation results show that in the frequency domain, compared with DAS and LCMV, the MUSIC method outperforms other algorithms in spatial resolution, robustness and output SNR. A hybrid method combining the LM-CN, BW-MUSIC method to estimate sound source location and the ground impedance simultaneously has been proposed. The proposed method is firstly verified by FEM and MATLAB simulations. During the BW-MUSIC localization approach, the location of the sound source is quite accurate, and no sidelobe distortion could be noticed in the sound map. Besides, by replacing the backward FDM with CN

method, the rate and accuracy of convergence during LM optimization approach is improved significantly. Still, with the ground reflection effect, the kurtosis beamformer could provide the accurate fault detection results.

The works from stationary sound sources is extended to the moving sound sources. When it is assumed that the moving distance during processing time is quite short, the short-time processing approach by BW-DAS and BW-MUSIC method is proposed to locate the moving sources with low Mach number. The moving sound source could be easily traced by such means. To localise the moving sound source in high Mach number and detect the fault, de-Dopplerization approach integrated with kurtosis beamformer has been proposed then. The experiment results show that the improved kurtosis beamformer can detect the fault under moving sound source conditions.

Hereto, a hybrid microphone array signal processing approach for faulty wheel identification and ground impedance estimation is proposed, and it is thoroughly studied theoretically and experimentally.

6.2 Recommendations for future research

This thesis focuses on the sound source localization and characterization problem in wheel/rail system. Based on beamforming technique, methods are developed for ground impedance and moving sound source situation. According to the present study, future research can be carried out.

The main idea of this fault detection approach is based on the statistic estimator kurtosis to extract the impulsiveness feature of the impact noise. As one of the key programs of fault diagnosis, feature extraction directly influences diagnosis results. There are other techniques to extract the signal features, for instance, information entropy, could be considered to be integrated with beamforming technique to detect the fault or any other sound source with obvious characteristics.

The kurtosis beamformer method is formulated under the free-field condition assumption. It works well in such situations where the direct-path component of the source signal is dominant. In Chapter 4 the ground impedance is considered, yet the sound source including true source and image source are still countable. In the future study, a more realistic formulation is to be established in which the reverberation effects should be considered. In such situation, not only the direct wave but the reflect waves should be included in the theoretical model.

The sound source localization system utilizes 16 MEMS microphones in a ULA or a 4*4 plane array to detect the fault. However, by optimizing the positions of the microphones, an array contains less microphone may have the ability to achieve the sound source localization and fault detection. Mathematical mode and experiments could be established and implemented to verify the optimized microphone array.

Computational time cost in time-domain calculation could be large. A more efficient way to use the time-domain beamforming could be considered in the

future research as well.

REFERENCES

Alemi, A., Corman, F., & Lodewijks, G. Review on condition monitoring approaches for the detection of railway wheel defects.

Antoni, J. (2004). The Spectral Kurtosis of nonstationary signals: formalisation, some properties, and application. Paper presented at the Signal Processing Conference, 2004 12th European.

Antoni, J. (2006). The spectral kurtosis: a useful tool for characterising non-stationary signals. Mechanical Systems and Signal Processing, 20(2), 282-307.

Antoni, J., & Randall, R. (2006). The spectral kurtosis: application to the vibratory surveillance and diagnostics of rotating machines. Mechanical Systems and Signal Processing, 20(2), 308-331.

Bao, C. (2014). Performance of time domain and time-frequency domain adaptive beamformers with moving sound sources. Paper presented at the INTER-NOISE and NOISE-CON Congress and Conference Proceedings.

Barke, D., & Chiu, W. (2005). Structural health monitoring in the railway industry: a review. Structural Health Monitoring, 4(1), 81-93.

Beebe, R. S. (1995). Machine Condition Monitoring: How to Predict Maintenance Requirements for Rotating and Stationary Plant: MCM Consultants.

Brooks, T. F., & Humphreys, W. M. (2006). A deconvolution approach for the mapping of acoustic sources (DAMAS) determined from phased microphone

arrays. Journal of Sound and Vibration, 294(4), 856-879.

Cabada, E. C., Leclere, Q., Antoni, J., & Hamzaoui, N. (2017). Fault detection in rotating machines with beamforming: Spatial visualization of diagnosis features. Mechanical Systems and Signal Processing, 97, 33-43.

Capdevielle, V., Serviere, C., & Lacoume, J. (1996). Blind separation of wide-band sources: Application to rotating machine signals. Paper presented at the European Signal Processing Conference, 1996. EUSIPCO 1996. 8th.

Carter, G. (1981). Time delay estimation for passive sonar signal processing. IEEE Transactions on Acoustics, Speech, and Signal Processing, 29(3), 463-470.

Chen, L., & Choy, Y.-S. FAULT IDENTIFICATION AND LOCALIZATION FOR MOVING WHEELS BASED ON DE-DOPPLERIZATION BEAMFORMING KURTOSIS METHOD.

Chen, L., Choy, Y. S., & Wang, T. G. (2017). Fault diagnosis by time-domain beamforming integrated with kurtosis method. Paper presented at the INTER-NOISE and NOISE-CON Congress and Conference Proceedings.

Chen, L., Choy, Y. S., Wang, T. G., & Chiang, Y. K. Fault detection of wheel in wheel/rail system using kurtosis beamforming method. Structural Health Monitoring, 0(0), 1475921719855444. doi:10.1177/1475921719855444

Cigada, A., Ripamonti, F., & Vanali, M. (2007). The delay & sum algorithm applied to microphone array measurements: numerical analysis and experimental validation. Mechanical Systems and Signal Processing, 21(6), 2645-2664.

Daubechies, I. (1990). The wavelet transform, time-frequency localization and

signal analysis. IEEE Transactions on Information Theory, 36(5), 961-1005.

de la Rosa, J. J. G., Sierra-Fernández, J. M., Agüera-Pérez, A., Palomares-Salas, J. C., & Moreno-Muñoz, A. (2013). An application of the spectral kurtosis to characterize power quality events. International Journal of Electrical Power & Energy Systems, 49, 386-398.

Dornfeld, D., & Cai, H. G. (1984). An investigation of grinding and wheel loading using acoustic emission. Journal of Engineering for Industry, 106(1), 28-33.

Drinkwater, B. W., & Wilcox, P. D. (2006). Ultrasonic arrays for non-destructive evaluation: A review. Ndt & E International, 39(7), 525-541.

Dvorkind, T. G., & Gannot, S. (2005). Time difference of arrival estimation of speech source in a noisy and reverberant environment. Signal Processing, 85(1), 177-204.

Dwyer, R. (1983). Detection of non-Gaussian signals by frequency domain kurtosis estimation. Paper presented at the Acoustics, Speech, and Signal Processing, IEEE International Conference on ICASSP'83.

Dwyer, R. (1984). Use of the kurtosis statistic in the frequency domain as an aid in detecting random signals. IEEE Journal of Oceanic Engineering, 9(2), 85-92.

Dwyer, R. (1985). Asymptotic detection performance of discrete power and higher-order spectra estimates. IEEE Journal of Oceanic Engineering, 10(3), 303-315.

Eftekharnejad, B., Alssayh, M., Addali, A., & Mba, D. (2012). Spectral kurtosis applied to acoustic emission in bearings. Paper presented at the Journal of Physics:

Conference Series.

Fan, R., Su, Z., Meng, G., & He, C. (2014). Application of sound intensity and partial coherence to identify interior noise sources on the high speed train. Mechanical Systems and Signal Processing, 46(2), 481-493.

Fassois, S. D., & Sakellariou, J. S. (2007). Time-series methods for fault detection and identification in vibrating structures. Philosophical Transactions of the Royal Society of London A: Mathematical, Physical and Engineering Sciences, 365(1851), 411-448.

Fink, M. (1999). Time-reversed acoustics. Scientific American, 281(5), 91-97.

Fink, M., Montaldo, G., & Tanter, M. (2004). Time reversal acoustics. Paper presented at the IEEE Ultrasonics Symposium, 2004.

Grassie, S., & Kalousek, J. (1993). Rail corrugation: characteristics, causes and treatments. Proceedings of the Institution of Mechanical Engineers, Part F: Journal of Rail and Rapid Transit, 207(1), 57-68.

Grassie, S. L. (2005). Rail corrugation: advances in measurement, understanding and treatment. Wear, 258(7), 1224-1234.

Hanson, C. E., Towers, D. A., & Meister, L. D. (2006). Transit noise and vibration impact assessment. Retrieved from

Hartley, H. O. (1961). The modified Gauss-Newton method for the fitting of non-linear regression functions by least squares. Technometrics, 3(2), 269-280.

Howell, G., Bradley, A., McCormick, M., & Brown, J. (1986). De-dopplerization and acoustic imaging of aircraft flyover noise measurements. Journal of Sound and

Vibration, 105(1), 151-167.

Huang, C., Teng, T., & Sun, D. (2016). Low-speed moving target detection of single frame image based on Doppler shift estimation. Paper presented at the 2016 IEEE/OES China Ocean Acoustics (COA).

Ishi, C. T., Chatot, O., Ishiguro, H., & Hagita, N. (2009). Evaluation of a MUSIC-based real-time sound localization of multiple sound sources in real noisy environments. Paper presented at the 2009 IEEE/RSJ International Conference on Intelligent Robots and Systems.

Jeffers, R., Bell, K. L., & Van Trees, H. L. (2002). Broadband passive range estimation using MUSIC. Paper presented at the 2002 IEEE International Conference on Acoustics, Speech, and Signal Processing.

Johansson, A. (2006). Out-of-round railway wheels—assessment of wheel tread irregularities in train traffic. Journal of Sound and Vibration, 293(3), 795-806.

Khorrami, M. R., Lockard, D. P., Humphreys Jr, W. M., Choudhari, M. M., & Van de Ven, T. (2008). Preliminary analysis of acoustic measurements from the NASA-Gulfstream airframe noise flight test. AIAA Paper, 2814, 5-7.

Kim, Y.-H., & Choi, J.-W. (2013). Sound visualization and manipulation: John Wiley & Sons.

Levenberg, K. (1944). A method for the solution of certain non-linear problems in least squares. Quarterly of Applied Mathematics, 2(2), 164-168.

Li, J., Stoica, P., & Wang, Z. (2003). On robust Capon beamforming and diagonal loading. IEEE Transactions on Signal Processing, 51(7), 1702-1715.

Li, K., Attenborough, K., & Heap, N. (1991). Source height determination by ground effect inversion in the presence of a sound velocity gradient. Journal of Sound and Vibration, 145(1), 111-128.

Liang, B., Iwnicki, S., Ball, A., & Young, A. E. (2015). Adaptive noise cancelling and time–frequency techniques for rail surface defect detection. Mechanical Systems and Signal Processing, 54, 41-51.

Liu, H., Huang, W., Wang, S., & Zhu, Z. (2014). Adaptive spectral kurtosis filtering based on Morlet wavelet and its application for signal transients detection. Signal Processing, 96, 118-124.

Lu, W., Jiang, W., Yuan, G., & Yan, L. (2013). A gearbox fault diagnosis scheme based on near-field acoustic holography and spatial distribution features of sound field. Journal of Sound and Vibration, 332(10), 2593-2610.

Marquardt, D. W. (1963). An algorithm for least-squares estimation of nonlinear parameters. Journal of the society for Industrial and Applied Mathematics, 11(2), 431-441.

Martin, H., & Honarvar, F. (1995). Application of statistical moments to bearing failure detection. Applied Acoustics, 44(1), 67-77.

Matsumoto, A., Sato, Y., Ohno, H., Tomeoka, M., Matsumoto, K., Kurihara, J., . . . Sato, Y. (2008). A new measuring method of wheel–rail contact forces and related considerations. Wear, 265(9), 1518-1525.

Maynard, J. D., Williams, E. G., & Lee, Y. (1985). Nearfield acoustic holography: I. Theory of generalized holography and the development of NAH. The Journal of

the Acoustical Society of America, 78(4), 1395-1413.

Michel, U. (2006). History of acoustic beamforming. Paper presented at the Berlin Beamforming Conference, Berlin, Germany, Nov.

Mucci, R. (1984). A comparison of efficient beamforming algorithms. IEEE Transactions on Acoustics, Speech, and Signal Processing, 32(3), 548-558.

Nakajima, H., Nakadai, K., Hasegawa, Y., & Tsujino, H. (2007). Moving sound source extraction by time-variant beamforming. Paper presented at the Annual Conference of the Japanese Society for Artificial Intelligence.

Nason, G. P., & Silverman, B. W. (1995). The stationary wavelet transform and some statistical applications. In Wavelets and statistics (pp. 281-299): Springer.

Nielsen, J. C., & Johansson, A. (2000). Out-of-round railway wheels-a literature survey. Proceedings of the Institution of Mechanical Engineers, Part F: Journal of Rail and Rapid Transit, 214(2), 79-91.

Ottonello, C., & Pagnan, S. (1994). Modified frequency domain kurtosis for signal processing. Electronics Letters, 30(14), 1117-1118.

Owsley, N., & Swope, G. (1981). Time delay estimation in a sensor array. IEEE Transactions on Acoustics, Speech, and Signal Processing, 29(3), 519-523.

Pagnan, S., Ottonello, C., & Tacconi, G. (1994). Filtering of randomly occurring signals by kurtosis in the frequency domain. Paper presented at the Pattern Recognition, 1994. Vol. 3-Conference C: Signal Processing, Proceedings of the 12th IAPR International Conference on.

Pal, S., Daniel, W. J., & Farjoo, M. (2013). Early stages of rail squat formation and

the role of a white etching layer. International Journal of Fatigue, 52, 144-156.

Peng, Z., & Kessissoglou, N. (2003). An integrated approach to fault diagnosis of machinery using wear debris and vibration analysis. Wear, 255(7-12), 1221-1232.

Quazi, A. (1981). An overview on the time delay estimate in active and passive systems for target localization. IEEE Transactions on Acoustics, Speech, and Signal Processing, 29(3), 527-533.

Rincon, R. F., Vega, M., Buenfil, M., Geist, A., Hilliard, L., & Racette, P. (2010). DBSAR's first multimode flight campaign. Paper presented at the Synthetic Aperture Radar (EUSAR), 2010 8th European Conference on.

Salzburger, H.-j., Schuppmann, M., Li, W., & Xiaorong, G. (2009). In-motion ultrasonic testing of the tread of high-speed railway wheels using the inspection system AUROPA III. Insight-Non-Destructive Testing and Condition Monitoring, 51(7), 370-372.

Sawalhi, N., Randall, R., & Endo, H. (2007). The enhancement of fault detection and diagnosis in rolling element bearings using minimum entropy deconvolution combined with spectral kurtosis. Mechanical Systems and Signal Processing, 21(6), 2616-2633.

Schmidt, R. (1986). Multiple emitter location and signal parameter estimation. IEEE Transactions on Antennas and Propagation, 34(3), 276-280.

Seo, D.-H., Choi, J.-W., & Kim, Y.-H. (2014). Impulsive sound source localization using peak and RMS estimation of the time-domain beamformer output. Mechanical Systems and Signal Processing, 49(1), 95-105.

Shibata, K., Takahashi, A., & Shirai, T. (2000). Fault diagnosis of rotating machinery through visualisation of sound signals. Mechanical Systems and Signal Processing, 14(2), 229-241.

Sijtsma, P. (2007). CLEAN based on spatial source coherence. International journal of aeroacoustics, 6(4), 357-374.

Steyskal, H. (1987). Digital beamforming antennas-An introduction. Microwave Journal, 30, 107.

Su, Z., Ye, L., & Lu, Y. (2006). Guided Lamb waves for identification of damage in composite structures: A review. Journal of Sound and Vibration, 295(3), 753-780.

Sweilam, N., Khader, M., & Mahdy, A. (2012). Crank-Nicolson finite difference method for solving time-fractional diffusion equation. Journal of Fractional Calculus and Applications, 2(2), 1-9.

Tam, K.-C., Lau, S.-K., & Tang, S.-K. (2016). Estimation of source location and ground impedance using a hybrid multiple signal classification and Levenberg–Marquardt approach. Journal of Sound and Vibration, 374, 279-296.

Thompson, D., & Jones, C. (2000). A review of the modelling of wheel/rail noise generation. Journal of Sound and Vibration, 231(3), 519-536.

Trees, H. (2002). Optimum array processing. In: New York: John Wiley & Sons.

Tuma, J., Janecka, P., Vala, M., & Richter, L. (2012). Sound source localization. Paper presented at the Carpathian Control Conference (ICCC), 2012 13th International.

Vér, I., Ventres, C., & Myles, M. (1976). Wheel/rail noise—part III: impact noise generation by wheel and rail discontinuities. Journal of Sound and Vibration, 46(3), 395-417.

Valin, J.-M., Michaud, F., Hadjou, B., & Rouat, J. (2004). Localization of simultaneous moving sound sources for mobile robot using a frequency-domain steered beamformer approach. Paper presented at the IEEE International Conference on Robotics and Automation, 2004. Proceedings. ICRA'04. 2004.

Veronesi, W., & Maynard, J. D. (1987). Nearfield acoustic holography (NAH) II. Holographic reconstruction algorithms and computer implementation. The Journal of the Acoustical Society of America, 81(5), 1307-1322.

Vrabie, V., Granjon, P., Maroni, C.-S., & Leprettre, B. (2004). Application of spectral kurtosis to bearing fault detection in induction motors. Paper presented at the 5th International Conference on acoustical and vibratory surveillance methods and diagnostic techniques (Surveillance5).

Wang, Y., Xiang, J., Markert, R., & Liang, M. (2016). Spectral kurtosis for fault detection, diagnosis and prognostics of rotating machines: A review with applications. Mechanical Systems and Signal Processing, 66, 679-698.

Wang, Z., Li, J., & Wu, R. (2005). Time-delay-and time-reversal-based robust capon beamformers for ultrasound imaging. IEEE Transactions on Medical Imaging, 24(10), 1308-1322.

Wu, T., & Thompson, D. (2002). A hybrid model for the noise generation due to railway wheel flats. Journal of Sound and Vibration, 251(1), 115-139.

Zhang, X.-Z., Bi, C.-X., Zhang, Y.-B., & Xu, L. (2015). Sound source identification and sound radiation modeling in a moving medium using the time-domain equivalent source method. The Journal of the Acoustical Society of America, 137(5), 2678-2686.

Zhang, X., Feng, N., Wang, Y., & Shen, Y. (2015). Acoustic emission detection of rail defect based on wavelet transform and Shannon entropy. Journal of Sound and Vibration, 339, 419-432.

Zhang, Y., Liang, M., Li, C., & Hou, S. (2013). A Joint Kurtosis-Based Adaptive Bandstop Filtering and Iterative Autocorrelation Approach to Bearing Fault Detection. Journal of Vibration and Acoustics, 135(5), 051026.